מכון ויצמן למדע
WEIZMANN INSTITUTE OF SCIENCE

עבודת גמר (תזה) לתואר
דוקטור לפילוסופיה

מוגשת למועצה המדעית של
מכון ויצמן למדע
רחובות, ישראל

מאת
רביד שניו

Thesis for the degree
Doctor of Philosophy

Submitted to the Scientific Council of the
Weizmann Institute of Science
Rehovot, Israel

By
Ravid Shaniv

שיטות מאינפורמציה קוונטית לטובת מדידות מדוייקות בעזרת יונים לכודים
Quantum Information Methods For Precision Measurements With Trapped Ions

מנחה:
פרופ' רועי עוזרי

Advisor:
Prof Roee Ozeri

אייר ה'תשע"ט

May 2019

To my wife, Sharon, my son Amit, my daughter Eden and my cat Moshie

Contents

Acknowledgments

I would like to first thank my wife Sharon, for supporting, understanding and forcing me to excel. In my eyes, technical frustration is the biggest enemy of scientific motivation for the experimental physicist, and Sharon helped me deal with frustration by knowing when to listen, when to advise and when to tell me "that's enough, take a break". Sharon is also the main reason I am continuing for a postdoc, since she knows me better than myself and was and is certain that I should at least try. I would like to thank my two children, Amit and Eden, for making the Ph.D period significant not only scientifically, and making me happier at all times, during and after work.

Second, I want to thank my adviser, Prof. Roee Ozeri, for being the gateway to experimental science, and infecting me with the excitement of thinking, building and performing experiments. Roee has his way of taking a complicated, possibly unsolvable experimental problem, identify its most basic underlying physical principles, and then solve it with intuition and some number hand waving. If I could choose to retain one thing from my Ph.D, it would be Roee's simple-but-deep way of thinking and problem solving. I want to also thank Roee for having the courage to let a new and inexperienced master's student enter a complicated and already working quantum information lab, deviate from the lab's original path and pursue his own scientific whims. I believe that this is the way science should be done.

Third, I would like to thank my group members, for being true friends and colleagues, for helping both theoretically and physically when are asked, and for providing the best work environment anyone could ask for.

A very special thanks goes to Nitzan Akerman, for the patience to help a beginner through technical lab stuff and theoretical ideas, both as a former group member who build the lab, and as a staff scientist later on. Without him, being available to help or to discuss, my learning curve would be much flatter. Here I would also like to mention and thank Ziv Meir, a senior Ph.D from Roee's second lab, who was sitting next to me in the office and had the time to exchang ideas and to help me solve technical and fundamental problems in my experiments.

Finally, I would like to thank my parents, Ayala and Amnon Shaniv, for planting the desire to answer the question "how does *** work?" since childhood, for supporting me both financially when needed and morally when needed, and for consistently making me know how proud of me they are.

Part I
Thesis Introduction

Back in the 20^{th} century, quantum mechanics (QM) was the new, revolutionary, counter-intuitive theory that stimulated the minds of philosophers and scientists alike. It provided an explanation to observed phenomena (e.g. the photoelectric effect) that was remarkably different from classical predictions. For about a century scientists examined this theory and tested it experimentally, reaching the conclusion that, although not all physical problems are solved, this theory provides a more comprehensive explanation to experimental observations, and yields reliable predictions.

QM aspects are apparent in the evolution of a massive system usually when some of its degrees of freedom are well isolated from its environment. Front-runner examples are superconducting circuits, cold molecules, cold atoms, trapped atomic ions etc. In this thesis, I will, focus on the latter. These systems are somewhat "simple" quantum mechanical systems, and the developed theory of the previous century allows to theoretically predict their behavior well. One evidence of the relative quantum-simplicity of cold atoms is the ability to account only for small number of atomic energy levels or quantum states. The simplest quantum entity is the two-level system, in which two energy levels of the atom can be isolated and well addressed with minimal coupling to other levels.

As consistently happens with new and exciting physical theories, once they are established, yield reliable predictions and are accepted as accurate enough, technological uses begin to emerge, and applications for the new understanding of the world are found. With trapped ions, two dominant applicative fields emerged: Quantum Information Processing (QIP) and Precision Measurements (PM). Both these fields benefit from the well-developed methods for trapping, cooling and manipulating the internal quantum states of atomic ions, many of which are summarized in [1].

The basic building block of QIP is the qubit (QUantum-BIT), which is no other than a two-level quantum system. Here, the qubit can be encoded in any two levels within the entire subspace our ion (e.g. two electronic spin half states or states chosen from two optically separated orbitals). Quantum information is encoded in the amplitude and phase of the two-level superposition, and in the quantum correlations between many qubits, also known as "entanglement". The ability to quantum-mechanically manipulate a register of these qubits allows for QIP computational devices that can perform new type of algorithms, with efficiency advantage over classical computers that is exponential in the register size [2, 3]. This is the big promise of ("digital") quantum computation. However, in order to obtain this control over a large quantum register and to exploit the full quantum characteristics of it, one needs (as mentioned above) to isolate the system from undesired environmental effects, that may cause the loss of deterministic control of the register quantum state. This is termed "decoherence", and is characterized by a time scale for loss of coherent control of the quantum

state - the decoherence time. Long decoherence time has been the main motivation for a race towards the best platform for quantum computation for over 50 years, and it is still ongoing. Examples are superconducting qubits coupled via microwave resonator [4], photos coupled through beam-splitters [5], Rydberg atoms coupled through the Rydberg dipole dipole interaction [6], trapped ions coupled through their Coulomb repulsion [3] etc. In addition to choosing a different physical quantum system, different methods were theoretically developed and experimentally demonstrated in order to extend the coherence time of a quantum register, e.g. decoherence free subspaces (DFS), Dynamical Decoupling (DD) and quantum error correction [7]. As a part of my Ph.D work, I participated in two experiments aimed at improving the fidelity and prolonging the coherence time for one type of operations on a trapped ions quantum register, a two-qubit entanglement operation, and making it more robust to undesired environment noise and drifts [8, 9]. However, this is not the topic I choose to focus on in my thesis.

In PM, the second field trapped ions are among its leading platforms, rather than isolating the ions from any effect other than the experimentalist's control, the goal is to controllably expose the ions to their environment. By measuring the dynamics or difference in the ion's final state with respect to its initial one, one can obtain information about its environment. The ion can be an excellent probe for some "standard" measurable quantities of interest, such as forces applied on it [10, 11] or electromagnetic fields at its position [12, 13], it can be used as a very precise, accurate and absolute clock ticking at optical frequencies [14, 15, 16], and perhaps shed some light on more "exotic" phenomena as well, e.g. dark matter particles interacting with it, testing whether fundamental constants are really constants in time of in space or testing invariance of our physical laws to spacial rotations [17]. Here, the goal is to improve and perfect the control of the ion's exposure to the desired part of the environment, while reducing all undesired effects altering the ion's quantum state, erasing the desired signal (causing decoherence) or disguising as a signal (adding systematics).

In the work I present here, I walked on the interface between these two fields. On one hand, I focused on the second goal - using trapped ions as probes for PM. On the other hand, I wanted to import and modify the well-developed techniques and operations aimed at isolating the ions from undesired environmental effects or enhancing the fidelity of the controlled operations developed for the field of QIP. This was not a trivial import, as the QIP techniques are aimed at completely decouple the ion from any interaction that is not applied by the experimentalist, and by definition, it implies that interesting environmental effects are canceled as well.

Below I will describe five experiments, utilizing the aforementioned concepts of DD [18] and entangling operations based on the celebrated M*ö*lmer-S*ö*rensen scheme [19, 20], in order to increase a measurement's Signal to Noise Ratio (SNR), either by increasing the amplitude of the desired signal or reducing the undesired noise, and in some cases both.

The notion of DD can be phrased as the application of a (usually time dependent) known Hamiltonian on a quantum system. This Hamiltonian is

chosen such that the evolution of the system, which is the combined known evolution and the environment unknown and possible noisy evolution, mimics an evolution decoupled from the noise in the environment at specific times. This concept originated from the idea of Hann's spin echo [21] in NMR, and since migrated to be a vital tool in atomic physics for quantum manipulation, measurements and information processing. Here, I used DD in order to mitigate uncontrolled noises, mainly magnetic field noise, that might reduce the precision and sometimes even completely overshadow the effects I was interested in. In some experiments I had modified the standard two-level DD and generalize it to a multi-level DD sequence.

Entanglement between ions is a key ingredient in the theoretical concept of quantum computers. In order to use the quantum advantage of computation power exponential in the qubit register size, one needs to be able to navigate in the large Hilbert space of the register, and this space includes mainly entangled states between the qubits. In a different setting, entanglement may provide a bypass to some previously considered limits of measurement uncertainty. By using N quantum probes independently (or alternatively, a single probe and N repeated measurements), one can reduce the uncertainty of the quantity being measured by $\sqrt{N}$ corresponding to the Standard Quantum Limit (SQL). However, when utilizing entanglement or quantum correlation between N multiple quantum probes, the uncertainty can be reduced by a factor between $\sqrt{N}$ and N, the latter correspond to the Heisenberg quantum limit [22], which is the lowest theoretical limit to measurement uncertainty allowed by quantum mechanics. This idea was experimentally demonstrated previously only in a Ramsey spectroscopy setting [23]. In my experiment I proposed and demonstrated this uncertainty reduction in Rabi spectroscopy for the first time.

The experiments I performed are partially proof of principle experiments and partially actual measurements of quantities of interest (some with the best precision to date). In addition to showing the specific measurements and protocols, I believe that the main message of my work is that the fields of QIP goes hand in hand with the field of quantum metrology and PM. If one's quantum system is insensitive to the environment but sensitive to one's control, it is a good qubit for information storing and manipulating. If one's system is sensitive to the environment, it is a probe, and clever choice of the control scheme may make it an excellent probe. The latter is the thread weaving my ideas and experiments presented here together.

Part II
Trapped $^{88}Sr^{+}$system, characteristics and toolbox

1 Ion trap apparatus and ion manipulation

1.1 Linear Paul trap

Our ions are trapped in a linear Paul trap [24]. The trap is composed of six cylindrical electrodes. Two, called the endcaps, are facing each other and are held in a DC potential. They define the $\hat{a}$ direction of the trap potential, also termed the axial direction. Since they are held at a constant potential, they confine the ions in the axial direction. The other four electrodes are arranged in two opposite pairs. One pair has a voltage oscillating at radio-frequency (RF) of $\approx$ 21 MHz, while the other two are held in a DC potential. Since the RF frequency is much faster than the ion response time to the changing forces the potential can be modeled as an effective quadratic potential in the $\hat{b} - \hat{c}$ plane, also referred to as the radial plane, such that $\left\{\hat{a}, \hat{b}, \hat{c}\right\}$ are an ordered triplet, and is called a pseudo-potential (since in is not actually a DC potential). A sketch of our trap is given in Fig 1.

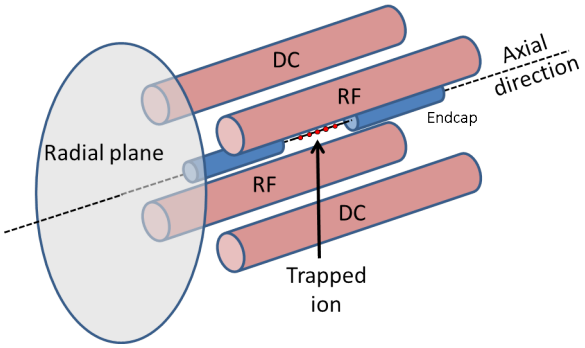

Figure 1: Schematic sketch of our linear Paul trap configuration

The motion of the ions in the pseudo-potential has been investigated thoroughly and is well understood [1]. Trapped ion chains systems can be laser-cooled to very low temperatures and are therefore localized to few nm. In addition, they can be moved using controlled voltages. These characteristics and more, entitle ion traps with the reputation of an excellent quantum experiments platform. Details on our specific trap design can be found in [25, 26].

1.2 Imaging system

The ions fluorescence is collected and detected in an optical imaging system. The same optical setup allows us both to image the ions' fluorescence for state detection and address a single ion out of the chain using the same optical system. The new imaging system uses a fast EMCCD camera to detect fluorescence from the ions, which is used to analyze which ion is in which state. Using this camera, when detecting the ions state, information of both the number of ions that are fluorescing and which ion is fluorescing are readily read from the camera output. More about the imaging system can be found in ref. [27].

2 $^{88}Sr^{+}$ ion

Sr is an earth-alkali metal, with atomic number of 38 - second column in the periodic table of elements. When ionized, it remains with one electron in its outer shell, and as such it shows a level structure similar to that of the hydrogen atom - first column in the periodic table of elements. We use $^{88}Sr^{+}$, which has no nuclear spin, and hence does not have hyperfine splitting. The relevant levels of the $^{88}Sr^{+}$ ion are plotted in Fig. 2.

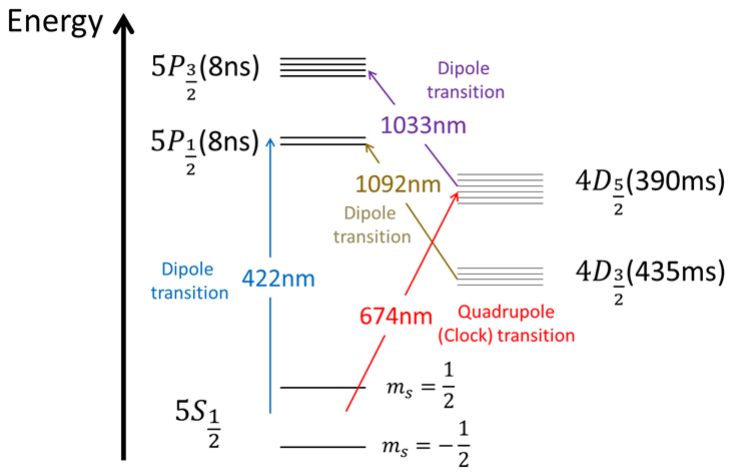

Figure 2: $^{88}Sr^{+}$ relevant level structure, along with the coupling laser wave lengths, transition type and levels life-times.

The $5S_{\frac{1}{2}} \leftrightarrow 4D_{\frac{5}{2}}$ transition, driven by a 674 nm laser, is a dipole forbidden but quadrupole allowed transition, and therefore it is a narrow transition, with linewidth of about 0.4 Hz. For that reason, this transition in earth-alkali metals

such as $^{88}Sr^{+}$ is used as a reference for optical atomic clocks. This transition can be interrogated with the help of a strong closed dipole transition, $5S_{\frac{1}{2}} \leftrightarrow 5P_{\frac{1}{2}}$, that is used for state fluorescence detection.

Notation remark: From this section and on, we will use the Dirac notation in order to denote the ion levels corresponding to the ground and excited Zeeman manifolds of the optical clock transition. The left symbol in the ket will be either S or J, corresponding to the ground $5S_{\frac{1}{2}}$ or the excited $4D_{\frac{5}{2}}$ manifolds, respectively. S and J will in general be used to denote manifolds with total angular momentum of half or higher, respectively. The right number in the ket will be the angular momentum projection number of the corresponding level. When not specified, this number will be denoted as m_S or m_J for the ground and the excited states, respectively. As an example, the state $\left|S, -\frac{1}{2}\right\rangle$ is the state in the $5S_{\frac{1}{2}}$ ground state Zeeman manifold, with quantum projection number $m_S = -\frac{1}{2}$.

2.1 Ion basic manipulation

2.1.1 Ion state initialization

At the beginning of most experiments, the ion is initialized in one of the $5S_{\frac{1}{2}}$ levels, e.g. $\left|S, \frac{1}{2}\right\rangle$, with optical pumping using the 422 nm dipole transition. A circular-polarized 422 nm light couples only the $\left|5S_{\frac{1}{2}}, -\frac{1}{2}\right\rangle$ sub-level the $5P_{\frac{1}{2}}$ manifold, from which it can decay to either $5S_{\frac{1}{2}}$ sub-level. After pulse time of hundreds of μs, the ion is pumped to the $m_{\frac{1}{2}} = \frac{1}{2}$ state with high probability (better than 99.9%), a state that is not coupled to the $5P_{\frac{1}{2}}$ level.

2.1.2 Ion state detection

The ion state can be projectively-measured using fluorescence selective detection. An ion in either $\left|S, -\frac{1}{2}\right\rangle$ or $\left|S, \frac{1}{2}\right\rangle$ will fluoresce 422 nm light when shined upon with linearly polarized 422 nm light, as this light couples both levels to the dipole strong transition $5S_{\frac{1}{2}} \rightarrow PS_{\frac{1}{2}}$. However, the same light would essentially not be scattered if the ion is in a state $|J, m_J\rangle$ in the excited state manifold. That means that shining 422 nm laser on the ion acts as a measurement, providing information whether the ion is in one of the S manifold sub-levels or not. When the ion is used as a two-level system with one level in the $5S_{\frac{1}{2}}$ level and one level in the $4D_{\frac{5}{2}}$ level (optical qubit), this measurement will provide one bit of information, whether the ion is in the S or the J manifolds. Averaged over many realizations, the population of the ion in each of the state can be extracted. If the ion is used as a two-level system encoded in the two Zeeman states of the the S manifold (Zeeman qubit), one of these states first needs to be transferred to one of the J sub-levels using the 674 nm laser (see below), and then a 422 nm detection can be applied. This method is referred to as electron-shelving [28].

2.1.3 Zeeman transition manipulation

A grounded RF electrode is located below the trap electrodes, and can be driven with an oscillating current. This current generates an oscillating magnetic field at the ion position, which couples to the spin of the ion. This field is used to rotate the ion's total angular momentum. In the S manifold, it couples the two $\{|S, m_S\rangle\}_{m_S}$ sub-levels, and can induce rotations in the sub-space spanned by them. In the J manifold, the RF magnetic field rotates the $J = \frac{5}{2}$ angular momentum within the $\{|J, m_J\rangle\}_{m_J}$ subspace.

2.1.4 Optical transition manipulation

A narrow linewidth 674 nm laser addresses the trapped ions in the trap. The laser's fast linewidth is smaller than 30 Hz over a few minutes, and as such it could resolve the different $|S, m_S\rangle \leftrightarrow |J, m_J\rangle$ transitions, which for the quantization magnetic field we apply - about 3 G, are separated by few MHz. The laser frequency is varied using acousto-optic modulators (AOM's) in order to tune it close to a specific transition. The frequency source of the AOM is either a direct-digital synthesizer (DDS) for precise and stable operation or a voltage controlled oscillator (VCO) for locking in-servo correction. Both the frequency and the phase of the laser can be controlled via the frequency and phase of the RF voltage applied to the AOM.

This beam has two configurations - single and global addressing. In the single addressing configuration, A focused 674 nm (about 3 μm waist) illuminates one of the ions in the chain, essentially manipulating only this single ion. In the global beam configuration, a different beam, focused less tightly (about 20 μm waist) compared to the single addressing beam, illuminates all the ions in the chain homogeneously. This beam can be sent from two directions, with 45°between them. The 674 nm laser beams configuration is illustrated in Fig. 3.

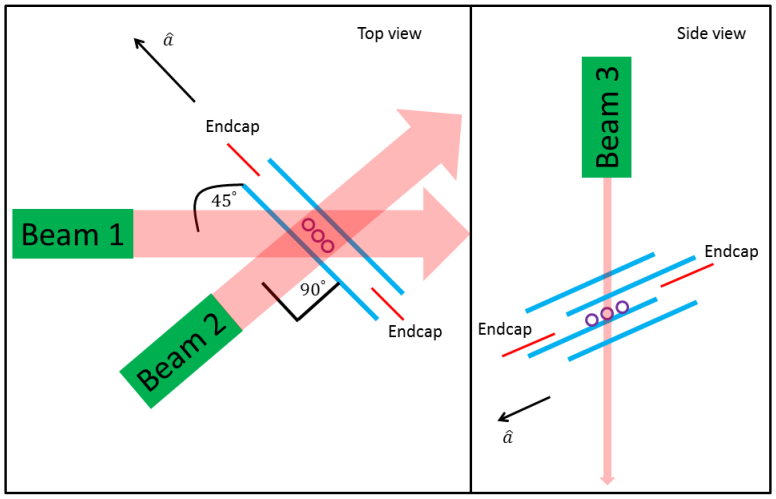

Figure 3: 674 nm laser beam configuration.
Left: The trap RF electrodes are marked as blue solid lines, while the endcaps are the red solid lines. The left sketch shows the two global beams from top view of the trap, as the pink thick arrows. These beams should shine equally on all the ions (three empty circles) in the chain. Unless stated otherwise, quantization axis aligns with beam 1. **Right:** a side view of the trap, and the single ion addressing beam is shown as a pink arrow, which is perpendicular to the plane spanned by the two global beams.

2.1.5 1092 nm laser repump

The $5P_{\frac{1}{2}}$ level can spontaneously decay to both the $5S_{\frac{1}{2}}$ level and the $4D_{\frac{3}{2}}$level. The ratio of the decay to these states is approximately 17:1 correspondingly[29]. In order to maintain ion fluorescence on the strong dipole transition for either cooling or detection, a repump laser, at 1092 nm close to resonance with the dipole transition $4D_{\frac{3}{2}} \leftrightarrow 5P_{\frac{1}{2}}$repumps the ion population out of the $4D_{\frac{3}{2}}$ Zeeman manifold.

2.1.6 1033 nm laser repump

As is seen from Fig. 2, the $4D_{\frac{5}{2}}$ level is a meta-stable level, with lifetime of about 390 msec. Every experiment we do concludes with state selective fluorescence detection which projects the ion either on the $S_{\frac{1}{2}}$ manifold - when fluorescence is detected - or on the $5D_{\frac{5}{2}}$ manifold, when it is dark. In both cases, the ion needs to be restarted to a known pure state, in order to maintain reasonable experimental duty cycle. Therefore, following any state detection, a 1033 nm repump laser pulse, close to resonance with the dipole transition $5D_{\frac{5}{2}} \leftrightarrow 5P_{\frac{3}{2}}$repumps the ion back to the $5S_{\frac{1}{2}}$ manifold. Both the $5D_{\frac{5}{2}} \leftrightarrow 5P_{\frac{3}{2}}$ and $5P_{\frac{3}{2}} \leftrightarrow 5S_{\frac{1}{2}}$ are dipole transitions, and therefore this pumping happens on the time scale of tens of ns.

2.2 Ion advanced manipulation

2.2.1 Cooling the ion

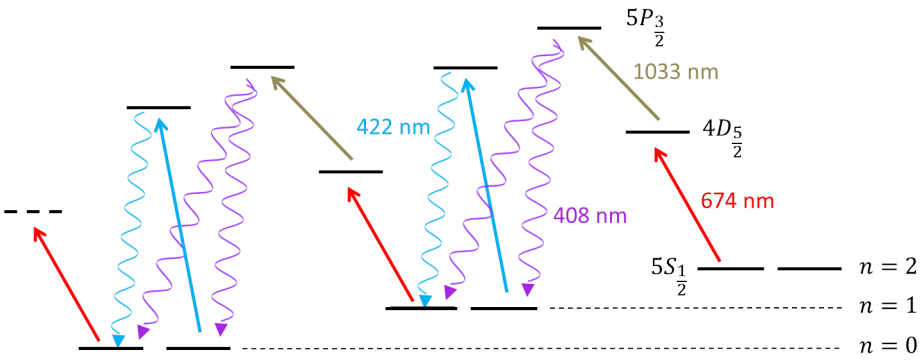

Figure 4: Sideband cooling scheme.
The plot demonstrates the continuous wave sideband cooling configuration. The lasers operating continuously are the 674 nm, 1033 nm and the 422 nm. The 674 nm is tuned to the red sideband of some specific transition between the $5S_{\frac{1}{2}}$ level and the $4D_{\frac{5}{2}}$ level. The 1033 nm repump then works between the $4D_{\frac{5}{2}}$ level and the $5P_{\frac{3}{2}}$ level. As the ion builds population in the $4D_{\frac{5}{2}}$ chosen level, this population is then transferred to the $5P_{\frac{3}{2}}$. Since the $5P_{\frac{3}{2}}$ level is fast decaying (see Fig. 2), it decays quickly to a random superposition of the $5S_{\frac{1}{2}}$ sub-levels. Since the 674 nm laser is tuned to a transition coupling only one of the $5S_{\frac{1}{2}}$ levels, a 422 nm optical pumping laser is operated(see subsection 1.3.1). The ion is then cascading down the harmonic motional energy states, until it reaches the zero point motion. The process then stops since the red sideband 674 nm laser does not couple the ion to an excited transition.

Even though the ion trap is dynamic (section 1.1), it can be approximated as a static 3D harmonic potential. In our experiments, we will focus on the ion motion in the axial direction. In order to manipulate the ion in the quantum regime, it needs to be cold. In trapped ions systems, it is possible to cool them very close to their motional ground harmonic state. More accurately, the ensemble averaged phonon number in the axial direction can satisfy $\langle \hat{n}_{axial} \rangle \ll 1$. This is done with the resolved side-band cooling method [30]. The ions are initially cooled using laser Doppler cooling technique [31]. An off-resonance 422 nm laser light is shined upon the ion. The light scattering rate depends on the ion velocity through the Doppler shift. In our system, this process cools the ion, and the ion's temperature reaches a temperature of about 2 mk, about a factor of four above the Doppler limit, $T_{Doppler} = \frac{\hbar\gamma}{2k_B}$ where γ is the natural linewidth of the transition. As mentioned above, for some applications the ion should be cooled even further, to its ground motional state. To this aim, a sequence of resolved sideband cooling pulses is being used sequentially to the

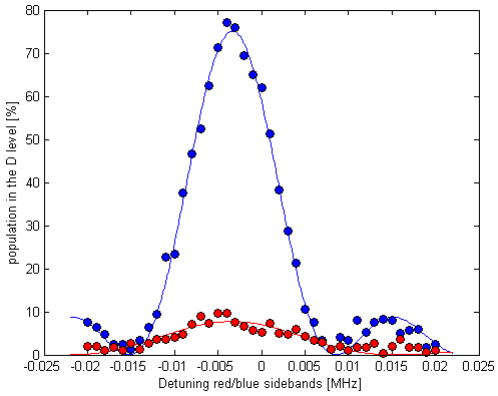

Figure 5: Ion response to 674 nm laser pulses tuned close to the red and the blue sidebands after sideband cooling.
The blue(red) dots are population in the $D_{\frac{5}{2}}$ level for different detuning from the blue(red) sideband transition after sideband cooling. It is apparent that the red sideband transition is quenched in comparison to the blue sideband transition, which indicates that the ion was indeed cooled. In this experiment we got $\langle \hat{n}_{axial} \rangle \approx 0.11$.

Doppler cooling process. This technique uses a narrow transition (the 674 nm clock transition in our case), so it could resolve the different motional sidebands in the ion's spectrum. The idea in its simple form is to excite the ion to a higher internal state but lower external motional state optically. Then induce fast decay of the ion from the internal excited state to the internal ground state, while maintaining the motional state unchanged, due to small Lamd-Dicke parameter. The result of this sequence is that the ion loses one quanta of motion every cycle and therefore cools. This process is repeated multiple times, and it stops when the ion is in its ground state. When that happens, the first pulse cannot excite the ion, since the ion is in its lowest motional state, and cannot be excited to a state with lower motional state. The ion therefore stays in the motional ground state. This sequence can be performed in pulses configuration, or in a continuous wave (CW) configuration. This sequence is illustrated in Fig. 4.

Laser cooling was already demonstrated in our setup [26]. A hallmark for this close to ground-state cooling is a suppression of excitation when the laser is tuned to the red sideband and an enhancement of population transfer when tuning the laser to the blue sideband. An experimental example for this observation is given in Fig. 5. As seen, while the blue sideband is excited, the red sideband is strongly suppressed.

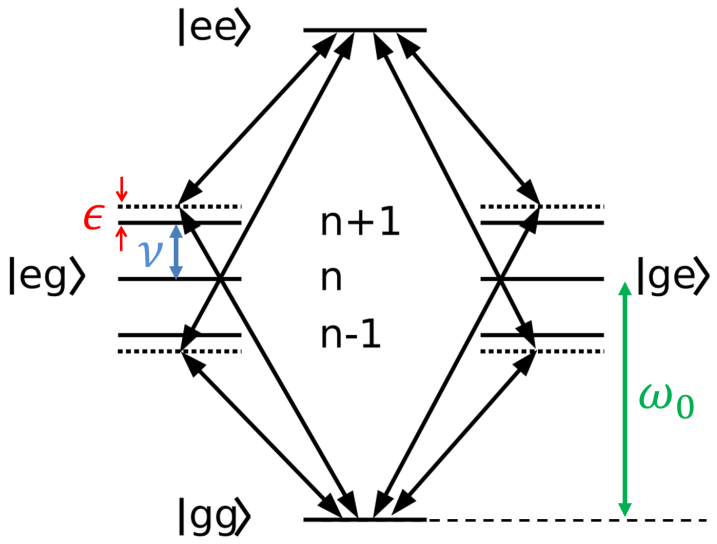

Figure 6: Frequency configuration for a Sörensen-Mölmer gate.

2.2.2 Coupling internal and external ion states

Some desired quantum operations involve manipulation of ions quantum state in a correlated manner - entangling operations. In simple terms, an entangled state of multiple trapped ion chain means that by knowing the state of one ion we gain some information about the state of the others. Therefore, the production of an entangled state must somehow involve a correlated operation on the ion chain as a whole, and not only on single ions. The first suggestion for an deterministic entanglement creating operation in trapped ion chains was purposed by Cirac and Zoller [2]. Since the ions in a trap repel each other due to the strong Coulomb force between them, their motion is described in the normal modes basis. As a result, a single harmonic motion mode would be shared by more than a single ion. Cirac and Zoller's suggested to use this mutual motion in order to couple the ions' internal states. This idea was a breakthrough in the theoretical concept of quantum computing using trapped ions. Later on, an ions' temperature-independent entangling method was proposed - Mölmer-Sörensen method [19].

In this method, the ions are excited by two laser frequencies. The frequencies are close to resonance with the first red and blue sidebands of a collective ion chain motional mode, corresponding to an optical transition. Below we briefly describe this process for a two-ion chain. We denote the relevant two-ion states as $|g$ or e, g or $e, n\rangle$, where e, g denote the two internal states in the optical transition and n denotes the number of motional quanta in the specific ion chain motion mode. We denote the laser frequencies as $\omega_{\pm} = \omega_0 \pm (\nu + \epsilon)$, where ω_0 is

the optical transition resonance frequency, ν is the motional mode frequency and ϵ is the deviation from resonance with the sideband. The frequency configuration is plotted in Fig. 6. These two frequencies add up to twice the optical transition frequency $2\omega_0$, and match the energy difference between the state $|gg, n\rangle$ and the state $|ee, n\rangle$ for any n. However, each laser frequency does not resonate with any transition on its own. That means that the internal transition $|gg\rangle \rightarrow |ee\rangle$ in this laser configuration is possible only by exciting a collective motion. As the frequencies are tuned off resonance from the motional sidebands, the resulting ion motion obeys the beating of a driven harmonic oscillator. By choosing the laser pulse time carefully, the lasers couple the internal state of the ions to their shared motional state during the evolution, and this evolution is times to stop at a point in time where the motional state of the ions is the same as the initial one, and decoupled from their internal state, which is entangled. This gives rise to the transitions:

$$|gg, n\rangle \rightarrow \frac{1}{\sqrt{2}} \left[|gg, n\rangle + i\,|ee, n\rangle\right],$$

$$|ge, n\rangle \rightarrow \frac{1}{\sqrt{2}} \left[|ge, n\rangle + i\,|eg, n\rangle\right],$$

$$|eg, n\rangle \rightarrow \frac{1}{\sqrt{2}} \left[|eg, n\rangle + i\,|ge, n\rangle\right],$$

$$|ee, n\rangle \rightarrow \frac{1}{\sqrt{2}} \left[|ee, n\rangle + i\,|gg, n\rangle\right].$$

Part III
Precision measurements involving optical-based methods

3 Introduction

In this part I will describe two experiments, employing optical pulses for the purpose of enhancing a desired physical signal and/or reducing the undesired noise signal affecting the measurement. In the first experiment, optical pulses were used in order to both enhance an AC signal in the ion's superposition phase oscillating at the pulses frequency, and mitigate oscillating signals at different frequency. Using this technique, referred to as "quantum lock-in" or DD, we measured small AC forces acting on our ion, which were translated to superposition phase via the Doppler effect. In the second experiment, we used a far detuned regime of the well known Mölmer-Sörensen laser pulse scheme, in order to create an entangling rotation of two qubits. Using this entangling rotation in a two-qubit subspace, we demonstrated Rabi spectroscopy type measurement of the ions' transition frequency close to the Heisenberg limit - the lowest uncertainty allowed by quantum mechanics. We also demonstrated close to Heisenberg limited measurement of the frequency difference between two ions, using the same method.

4 Quantum lock-in force sensing using optical clock Doppler velocimetry

The main article can be found in [11].

4.1 Abstract

In this work we present a method for measuring off-resonance oscillating forces using a trapped $^{88}Sr^{+}$ ion. Since the ion is trapped in a harmonic trap, there is a linear relation between the amplitude of the force applied on the ion and the ion's amplitude of motion. When the ion is prepared in an optical superposition, due to the Doppler effect, the relative phase between the ion and the laser oscillates at the ion's motion frequency. By applying a sequence of echo pulses at frequency matching the force frequency, this phase, instead of not averaging out, is accumulated over multiple oscillation cycles. This is a use of the well-known quantum lock-in technique, and here it allows measurement of forces which oscillates at frequency far (three orders of magnitude) from the trap resonance frequency. We report frequency force detection sensitivity as low as $1.3 \times 10^{-20}\mathrm{N} \cdot \mathrm{Hz}^{-\frac{1}{2}}$.

4.2 Driven undamped harmonic oscillator

A classical particle in a driven undamped Harmonic oscillator abides the equation for the oscillator position $x(t)$:

$$\ddot{x} + (2\pi f_t)^2 x = \frac{F_0}{m} \sin(2\pi f_m t + \xi_0).$$

where f_t is the oscillator frequency, m is the particle mass, F_0 is the AC force amplitude and f_m is the drive frequency. The solution for the initial conditions $x(t=0) = \dot{x}(t=0) = 0$ is

$$x(t) = x_0 \sin(2\pi f_m t + \xi_0) = \frac{F_0}{4\pi^2 m (f_t^2 - f_m^2)} \sin(2\pi f_m t + \xi_0). \quad (1)$$

From this solution, one can learn that the force amplitude is proportional to the oscillatory motion amplitude, and that they are related through a scale factor inversely proportional to $(f_t^2 - f_m^2)$. As a result, by measuring the amplitude of motion, one can detect the force applied on the particle. It is also evident that if the driving force frequency is close to the oscillator frequency, i.e. $f_t \sim f_m$, the force sensitivity increases, since small forces will induce large motion amplitudes. If on the other hand, $f_t \gg f_m$, the sensitivity for force detection reduces as f_t^2. In some cases, the difference between f_t and f_m is constrained due to various reasons, limiting for example f_t to be high while slower forces are to be measured. In this case, the motion amplitude is reduced, and therefore the signal to noise is reduced as well, yielding poor sensitivity in the use of the oscillator as a force detector. In this work, we demonstrate a method to enhance this signal to noise with the use of the quantum-mechanical properties of a trapped ion as the oscillator that can allow for the detection of off-resonance forces.

4.3 Doppler effect and optical superposition phase

4.3.1 General two level atom

We assume a two level atomic ion, with levels $|g\rangle, |e\rangle$, separated energetically by an optical frequency, ω_{eg}, defined in the rest frame of the ion. Initializing at $|g\rangle$ and applying a laser $\frac{\pi}{2}$ pulse with frequency $\omega \sim \omega_{eg}$, will result in the state $\psi(t=0) = \frac{1}{\sqrt{2}}(|g\rangle + |e\rangle)$. We define the detuning δ as $\delta = \omega - \omega_{eg}$. We now assume that $\delta \ll \omega_{eg}, \omega$, so we can use the rotating wave approximation [32]. Turning off the laser light and letting the ion evolve within the rotating frame of the atom, the evolution of the state is

$$\psi(t) = \frac{1}{\sqrt{2}} \left(|g\rangle + e^{i\phi(t)} |e\rangle \right),$$

where

$$\phi(t) = \int_0^t \delta(\tau)\, d\tau.$$

If the ion moves in a one dimensional oscillatory fashion in a direction that has a non-zero projection on the laser $\vec{k}$ vector, in the ion's frame of reference the laser light will be modulated due to the Doppler effect. Assuming laser frequency $\omega(t) \sim \omega_{eg}$ with k number at angle χ from the atomic line of motional, and assuming oscillatory velocity for the atom of $v(t) = v_0 \cos(2\pi f_m t + \xi_0)$, the time varying detuning between the atom and the laser is

$$\delta(t, \xi_0) = \omega(t) - \omega_{eg} = k v_0 \cos(\chi) \cos(2\pi f_m t + \xi_0) + \delta_N(t),$$

where $\delta_N(t)$ represents noise in the laser frequency, the ion resonance frequency or both. The corresponding superposition phase is

$$\phi(t, \xi_0) = \int_0^t [k v_0 \cos(\chi) \cos(2\pi f_m t + \xi_0) + \delta_N(t)] \, d\tau =$$

$$= \frac{k v_0}{2\pi f_m} \cos(\chi) (\sin(2\pi f_m t + \xi_0) - \sin(\xi_0)) + \int_0^t \delta_N(\tau) \, d\tau.$$

This can be written in terms of the motional amplitude, x_0:

$$\phi(t, \xi_0) = k x_0 \cos(\chi) (\sin(2\pi f_m t + \xi_0) - \sin(\xi_0)) + \int_0^t \delta_N(\tau) \, d\tau. \quad (2)$$

We denote $\phi_{Doppler}(t, \xi_0) = k x_0 \cos(\chi) (\sin(2\pi f_m t + \xi_0) - \sin(\xi_0))$ and we denote $\phi_{noise}(t) = \int_0^t \delta_N(\tau) \, d\tau$. From Eq. 2 we conclude from measuring the amplitude of $k x_0 \cos(\chi)$, while knowing k and χ, the value of x_0 can be obtained. Using Eq. 1, we can then obtain F_0, the force amplitude.

4.4 Signal enhancing using the quantum lock-in technique

4.4.1 Phase estimation averaging scale

Since $\phi_{Doppler}(t) = \phi_{Doppler}\left(t + \frac{1}{f_m}\right)$, the relative uncertainty in the force scales as

$$\frac{\Delta F_0}{F_0} \propto \frac{\Delta\phi}{\sqrt{N} \cdot k x_0 \cos(\chi)}$$

where $\Delta\phi$ is the uncertainty of a single phase estimation and N is the number of averaged phase estimations. In order to reduce the relative uncertainty, one could increase the signal amplitude in the denominator. To that aim, we employed the quantum lock-in technique [33].

4.4.2 The quantum lock-in technique main concept

In the quantum lock-in technique, we generate an external modulation to our detuning, in the form of $f(t)$. The implementation of this modulation is carried out by timed optical π pulses. As a result, the phase of the superposition becomes:

$$\phi(t, \xi_0) = \int_0^t f(\tau) \, \delta(\tau, \xi_0) \, d\tau$$

In our experiment we chose the modulation to be in the form of:

$$f(t,\tau,n) = \text{rect}\left(\frac{t}{2n\tau}\right)\left[\Theta(t) + 2\sum_{k=1}^{\infty}(-1)^k\,\Theta(t-(2k-1)\tau)\right].$$

This is a square modulation between the values of 1 and -1, at a period of 4τ. An example for $n = 4$ is illustrated in Fig. 7.

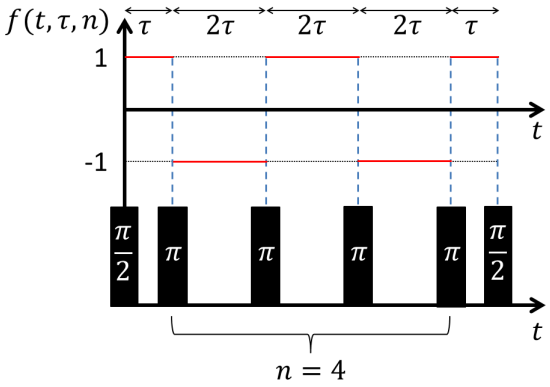

Figure 7: Schematic representation of the modulation function $f(t,\tau,n)$. The modulation function alternates between values of 1 and -1, as shown by the red horizontal lines. This modulation function is created by a periodic sequence of π pulses, between two Ramsey $\frac{\pi}{2}$ pulses, as is schematically shown at the bottom. Here, a four pulse sequence is shown in which the pulses are applied at time intervals of τ and 2τ, as shown in the top.

If we assume that $\delta_N(t)$ has very small spectral overlap with $f(t,\tau,n)$, for example if $\delta_N(t)$changes slowly on τ time scale, then the change of sign in $f(t,\tau,n)$ will mitigate the noise term in $\phi(t)$, that is $\int_0^t f(t,\tau,n)\,\delta_N(\tau)\,d\tau \approx 0$. From this point and on, we will neglect the effect of δ_N, unless stated otherwise. That is:

$$\delta(t,\xi_0) \approx kv_0\cos(\chi)\cos(2\pi f_m t + \xi_0)$$

We now divide the use of the modulation $f(t)$ into two cases:

Case I: The motional phase ξ_0 is known

In this case, a time delay can be inserted to the application of the function $f(t,\tau,n)$, such that the function applied is $f\left(t+\frac{\xi_0}{2\pi f_m},\tau,n\right)$. In addition, if the interval time $\tau = \frac{1}{4f_m}$ is chosen, then we get $f\left(t+\frac{\xi_0}{2\pi f_m},\tau,n\right)\cdot\delta(t,\xi_0) = |\delta(t,\xi_0)|$. The value of $\phi(t,\xi_0)$can be readily computed:

$$\phi(t,\xi_0) = \int_0^t |\delta(\tau,\xi_0)|\,d\tau = kv_0\cos(\chi)\int_0^t |\cos(2\pi f_m\tau+\xi_0)|\,d\tau.$$

We will assume now that $t = n \cdot \frac{1}{2f_m} + \tilde{t}$, where $\tilde{t} < \frac{1}{2f_m}$. Since the period of $|\cos(2\pi f_m t + \xi_0)|$is $\frac{1}{2f_m}$, we can write

$$\phi(t,\xi_0) = kv_0\cos(\chi)\left[n\int_0^{\frac{1}{2f_m}}\sin(2\pi f_m\tau)\,d\tau + \int_{n\cdot\frac{1}{2f_m}}^{n\cdot\frac{1}{2f_m}+\tilde{t}}\left|\cos(2\pi f_m\tau+\xi_0)\right|d\tau\right] =$$

$$= kv_0\cos(\chi)\left[\frac{2n}{2\pi f_m} + \int_{n\cdot\frac{1}{2f_m}}^{n\cdot\frac{1}{2f_m}+\tilde{t}}\left|\cos(2\pi f_m\tau+\xi_0)\right|d\tau\right] =$$

$$= 2nkx_0\cos(\chi) + kv_0\cos(\chi)\int_{n\cdot\frac{1}{2f_m}}^{n\cdot\frac{1}{2f_m}+\tilde{t}}\left|\cos(2\pi f_m\tau+\xi_0)\right|d\tau$$

If in addition we choose $\tilde{t} = 0$ in the interrogation time, we get

$$\phi(t) = 2nkx_0\cos(\chi).$$

Here, by increasing the interrogation time, i.e. increasing n, we can increase the phase signal that we measure, and reduce the relative uncertainty of our force measurement, that will scale as

$$\frac{\Delta F_0}{F_0} \propto \frac{\Delta\phi}{2n\cdot\sqrt{N}\cdot kx_0\cos(\chi)}.$$

Case II: The motional phase ξ_0 is unknown

Unlike the previous case, here we assume the ξ_0 is evenly distributed over experiment realizations. Therefore, the average of $\phi(t) = \int_0^t f(\tau',\tau,n)\,\delta(\tau')\,d\tau'$ over N realizations vanishes as N increases. However, instead of measuring the phase itself, we can use the fact that $\phi(t)$ enters the quantum state as $e^{i\phi(t)}$, and therefore we can measure the coherence of our state, i.e. $\left\langle e^{i\phi(t)}\right\rangle$, where the average is over experimental realizations, which translates to an average over the motional oscillation phase ξ_0. The coherence will depend on the amplitude of the force in a non-linear way, and from coherence measurement at different τ values, one could extract the phase oscillation amplitude, and therefore get an estimate for the force amplitude.

4.4.3 Theoretical model for the superposition phase

The analytic expression for the phase $\phi(t,\xi_0) = kv_0\cos(\chi)\int_0^{2n\tau_m} f(\tau',\tau,n)\cos(2\pi f_m\tau'+\xi_0)\,d\tau'$ where n is an even integer is (calculated in [33]):

$$\phi(t,\xi_0) = -4kx_0\cos(\chi)\cdot\frac{\cos\left(2\pi f_m n\tau+\xi_0+n\frac{\pi}{2}\right)\sin\left(2\pi f_m n\tau-n\frac{\pi}{2}\right)\sin^2\left(\frac{2\pi f_m\tau}{2}\right)}{\cos(2\pi f_m\tau)}. \tag{3}$$

For $\xi_0 = 0$, $\tau \to \frac{1}{4f_m}$ we get as expected:

$$\phi(t) = \lim_{\tau \to \frac{1}{4f_m}} \left[-4kx_0 \cos(\chi) \cdot \frac{\cos\left(2\pi f_m n\tau + n\frac{\pi}{2}\right) \sin\left(2\pi f_m n\tau - n\frac{\pi}{2}\right) \sin^2\left(\frac{2\pi f_m \tau}{2}\right)}{\cos(2\pi f_m \tau)} \right] =$$

$$= 4kx_0 \underbrace{\cos\left(\frac{\pi}{2}n + n\frac{\pi}{2}\right)}_{1} \underbrace{\sin^2\left(\frac{\pi}{4}\right)}_{\frac{1}{2}} \cos(\chi) \underbrace{\lim_{\tau \to \frac{1}{4f_m}} \left[-\frac{\sin\left(2\pi f_m n\tau - n\frac{\pi}{2}\right)}{\cos(2\pi f_m \tau)} \right]}_{n} =$$

$$= 2nkx_0 \cos(\chi)$$

4.4.4 Theoretical model for the superposition coherence

We assume that the phase of the force ξ_0 varies with each realization of the experiment, and it is uniformly distributed between 0 and 2π. With this assumption, we compute the average $\left\langle e^{i\phi(t,\xi_0)} \right\rangle_{\xi_0}$ for an even integer n:

$$\left\langle e^{i\phi(t)} \right\rangle_{\xi_0} =$$

$$= \frac{1}{2\pi} \int_{-\pi}^{\pi} \exp\left[i \left(-\frac{4kx_0 \cos(\chi) \cos\left(2\pi f_m n\tau + \xi_0 + n\frac{\pi}{2}\right) \sin\left(2\pi f_m n\tau - n\frac{\pi}{2}\right) \sin^2\left(\frac{2\pi f_m \tau}{2}\right)}{\cos(2\pi f_m \tau)} \right) \right] d\xi_0$$

We use the identity

$$J_0(x) = \frac{1}{2\pi} \int_{-\pi}^{\pi} \exp(ix\cos(y))\, dy,$$

where J_0 is Bessel function of the first kind, and we finally get

$$\left\langle e^{i\phi(t)} \right\rangle_{\xi_0} = \frac{1}{2\pi} \int_{-\pi}^{\pi} \left[\cos(\phi(t, \xi_0)) \right] d\xi_0 = J_0 \left(4kx_0 \cos(\chi) \cdot \frac{\sin(2\pi f_m n\tau) \sin^2\left(\frac{2\pi f_m \tau}{2}\right)}{\cos(2\pi f_m \tau)} \right). \tag{4}$$

4.5 Force detection experiment with $^{88}Sr^+$ trapped ion

4.5.1 Experimental system description

Our simplified experimental apparatus scheme is shown in Fig. 8.

In our experimental implementation of the force detection method described above, our atomic ion is $^{88}Sr^+$, and we choose$|g\rangle = \left|S, -\frac{1}{2}\right\rangle$ and $|e\rangle = \left|J, \frac{1}{2}\right\rangle$ in the $5S_{\frac{1}{2}}$ and $4D_{\frac{5}{2}}$ Zeeman manifolds respectively. Our axial trap frequency is $f_t = 1.13$ MHz and our ion is Doppler cooled to roughly 2 mK.

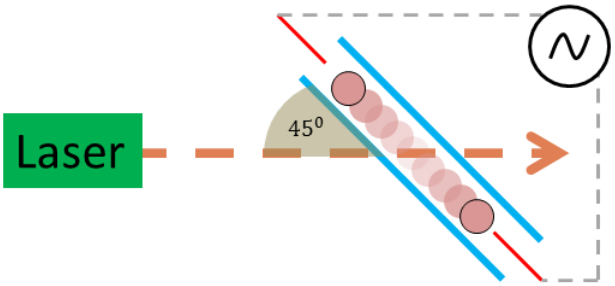

Figure 8: Simplified Experimental apparatus.
A trapped $^{88}Sr^{+}$ ion (pink full circles) is oscillating in the axial direction of a Paul trap (red and blue solid lines) under the influence of an oscillating voltage applied on the endcap electrodes (red solid lines). An interrogation laser is directed at 45^{o} degrees angle with respect to the ion's motion.

4.5.2 Motional phase ξ_0 is known

Experimental sequence

Our experimental sequence, based on Ramsey-type spectroscopy scheme, is as follows:

1. First, and throughout the experiment, we apply an oscillating force on the ion, at frequency of $f_m = 1013$ Hz. We do that by combining an oscillating voltage with the DC endcap voltage in our trap.

2. We begin the experimental sequence with initializing our ion in the $\psi_{init} = |g\rangle$ state using optical pumping (see section 2.1).

3. Next, we trigger our sequence to begin with a specific force phase ξ_0, such that ξ_0 is a controlled parameter.

4. At the trigger signal, we operate a $\frac{\pi}{2}$ laser pulse on the transition $|g\rangle \leftrightarrow |e\rangle$, and obtain the state

$$\psi\left(t=0\right)=\frac{1}{\sqrt{2}}\left(|g\rangle+|e\rangle\right).$$

5. We now turn on the modulation $F\left(t,\tau,n\right)$ by applying laser π pulses on the transition $|g\rangle \leftrightarrow |e\rangle$ at times $\left(2j-1\right)\tau$ when $j=1,2,...,n$. We choose n to be an even number of pulses. This choice allows us to alternate the phase of the pulses between 0 and π, such that pulse errors can be eliminated to leading order. After time of $2n\tau$, our state becomes

$$\psi\left(t=2n\tau\right)=\frac{1}{\sqrt{2}}\left(|g\rangle+e^{i\phi\left(2n\tau,\xi_0\right)}|e\rangle\right).$$

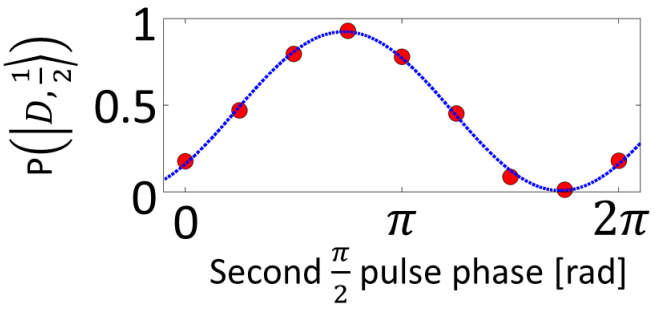

Figure 9: A typical Ramsey fringe, data and fit, for the case where ξ_0 is known.

6. In order to measure $\phi(t)$, we apply a second $\frac{\pi}{2}$ laser pulse driving the transition $|g\rangle \leftrightarrow |e\rangle$, with laser phase ϕ'. The resultant state is

$$\psi_{\text{interrogation}} =$$

$$= e^{i\frac{\phi(2n\tau,\xi_0)+\phi'}{2}} \cos\left(\frac{\phi(2n\tau,\xi_0)+\phi'}{2}\right)|g\rangle + ie^{i\frac{\phi(2n\tau,\xi_0)-\phi'}{2}} \sin\left(\frac{\phi(2n\tau,\xi_0)+\phi'}{2}\right)|e\rangle$$

7. We now measure whether the ion is in the $|g\rangle$ or the $|e\rangle$ state, by applying a 422 nm laser pulse, and measuring the ion fluorescence. The probability for no fluorescence detection is given by:

$$P(\text{Dark}|\phi',\tau,\xi_0,n) = \sin^2\left(\frac{\phi(2n\tau,\xi_0)+\phi'}{2}\right) = \frac{1}{2} - \frac{1}{2}\cos\left(\phi(2n\tau,\xi_0)+\phi'\right)$$

By Scanning the value of ϕ' we obtain a Ramsey fringe, from which the phase $\phi(2n\tau,\xi_0)$ can be extracted by a maximum likelihood fit. An example for such fringe is given in Fig. 9.

Results

In the experiment, we scanned the parameters ϕ' and $\xi_0$in the way described above, for a $n = 10$ modulation pulses. We now define $\tilde{\phi} = \phi(2n\tau,\xi_0) + \phi'$. The function $\tilde{\phi}(\phi',\xi_0)$ was plotted from the results of the scans of ϕ' and ξ_0, and was fitted to the theory. From this fit, the parameter x_0 in Eq. 1 was extracted, and from this parameter we could infer the force amplitude applied on the ion at $f_m = 1013$ Hz. The results and the fit to the theory are presented in Fig. 10.

The measured phase is in a good agreement with the theory. From the fit to the theory we estimate $x_0 = 59.8 \pm 0.3$ nm, and correspondingly $F_0 = 4.32 \pm 0.02 \times 10^{-19}$ N. We note here that this oscillation amplitude is about an order of magnitude below the optical wavelength (674 nm) whereas the phase acquired is larger than π. The total experiment time was about 9 Hours, and taking that into account, we estimated the sensitivity for the entire experiment

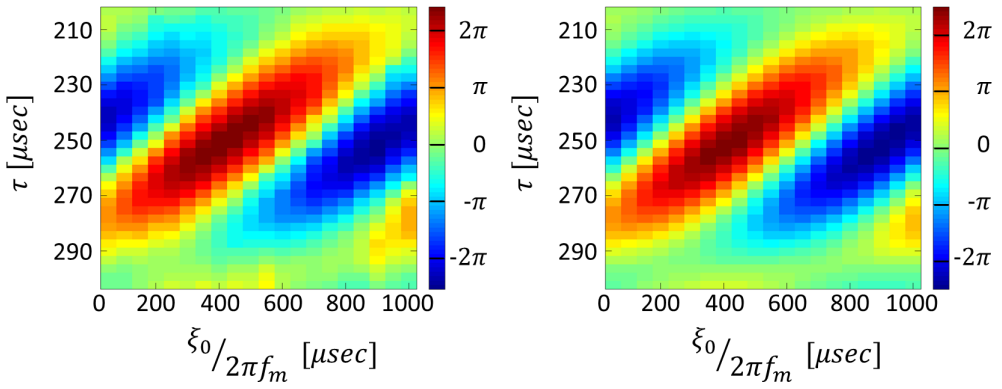

(a) Experimental results.

(b) Fit to theory.

Figure 10: $\tilde{\phi}$ as a function of ξ_0 and τ, for $n = 10$ echo pulses.

duration as 3.6×10^{-19} N·Hz$^{-\frac{1}{2}}$. However, the experiment results presented in figure 10a can be considered as a calibration, at the end of which the optimal parameters τ and ξ_0 are found. Therefore, the best sensitivity is reached when measuring at these values alone. We estimate that sensitivity by taking into account only the Ramsey fringe attained at these values. This single fringe experiment duration is about 19 s, and the force uncertainty for this fringe alone is 3×10^{-21} N. Therefore the estimated sensitivity is 1.3×10^{-20} N·Hz$^{-\frac{1}{2}}$.

4.5.3 Motional phase ξ_0 is unknown

The experimental sequence for this experiment is very similar to the known ξ_0 case. Steps 1-2 are identical. Step 3 has no meaning, since in this case ξ_0 cannot be a control parameter. The outcome is that in the different realizations, ξ_0 is distributed uniformly between 0 and 2π. The rest of the experimental steps are the same, but this time the probability $P\left(\text{Dark}|\phi'\right)$ in step 7 should be averaged over all realizations, meaning over ξ_0. Using Eq. 5, we can write:

$$\left\langle P\left(\text{Dark}|\phi'\right)\right\rangle_{\xi_0} =$$

$$= \frac{1}{2} - \frac{1}{2}\left\langle \cos\left(\phi\left(2n\tau\right) + \phi'\right)\right\rangle_{\xi_0} =$$

$$= \frac{1}{2} - \frac{1}{2}\left[\left\langle \cos\left(\phi\left(2n\tau\right)\right)\right\rangle_{\xi_0} \cos\left(\phi'\right) - \left\langle \sin\left(\phi\left(2n\tau\right)\right)\right\rangle_{\xi_0} \sin\left(\phi'\right)\right].$$

According to sub-subsection 2.4.4, the term $\langle \sin(\phi(2n\tau)) \rangle_{\xi_0}$ vanishes, and we are left with

$$\langle P(\text{Dark}|\phi') \rangle_{\xi_0} = \frac{1}{2} - \frac{1}{2} J_0 \left(4kx_0 \cos(\chi) \cdot \frac{\sin(2\pi f_m n\tau) \sin^2\left(\frac{2\pi f_m \tau}{2}\right)}{\cos(2\pi f_m \tau)} \right) \cos(\phi') .$$

This expression reflects a constant phase for the Ramsey fringe, up to a π phase shift due to the sign of the $J_0(\cdot)$ coefficient. We denote $C(\tau, n)$ to be the fringe contrast function:

$$C(\tau, n) = J_0 \left(4kx_0 \cos(\chi) \cdot \frac{\sin(2\pi f_m n\tau) \sin^2\left(\frac{2\pi f_m \tau}{2}\right)}{\cos(2\pi f_m \tau)} \right) .$$

The force amplitude can be extracted from the fringe contrast function. Typical fringes for different τ values are shown in figure 11.

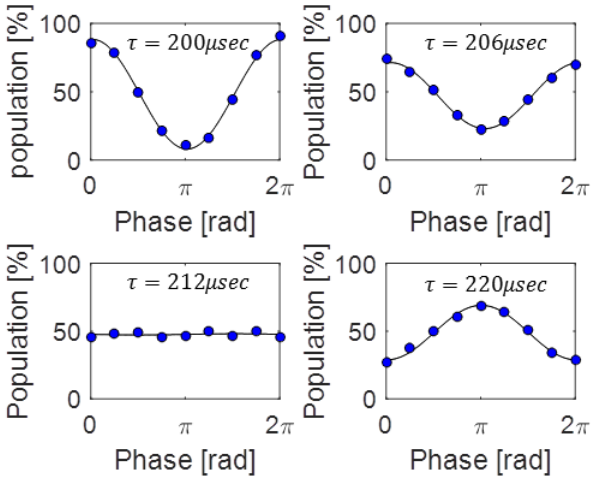

Figure 11: Typical Ramsey fringes for the case where ξ_0 is averaged. Four fringes were taken for different τ values in the modulation function, for $n = 10$ pulses. As the variance of $\phi(2n\tau, \xi_0)$ grows for different τ values, it could get to a point where the contrast vanishes (bottom left fringe). However, when the variance gets larger, the contrast absolute value increases, but with an overall π phase shift for the fringe. This revival of contrast is a result of the Bloch sphere equator having a topology of a circle.

Results

The experiment was carried out for $n = 10, 20$ pulses. The time τ was scanned, and the contrast extracted from the Ramsey fringe of each value of τ was fit to the contrast function $C(\tau, n)$. The results are shown in figure 12.

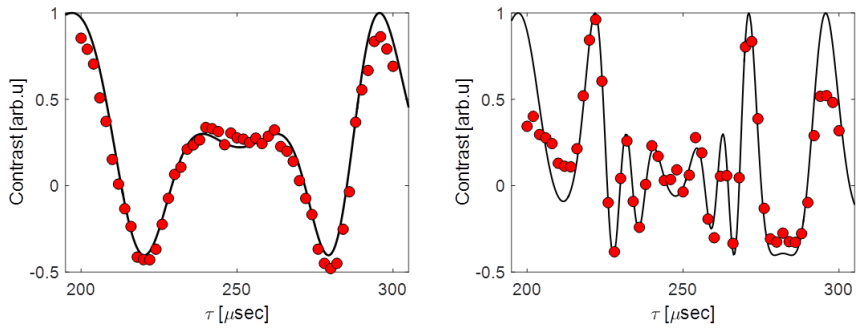

(a) $n = 10$ (b) $n = 20$

Figure 12: Measured Ramsey fringe contrast for different modulation times τ and fit to theory for $n = 10, 20$ pulses.

From the fits in figure 12 we could estimate the amplitude of the ion motion to be $x_0 = 58.0 \pm 1.5$ nm and $x_0 = 57.5 \pm 2.0$ nm for $n = 10, 20$ pulses respectively. From these measurements we could infer force amplitude of $4.3 \pm 0.1 \times 10^{-19}$ N and $4.3 \pm 0.2 \times 10^{-19}$ N respectively. The sensitivity in this experiment was $0.9 \times 10^{-18}$and 1.0×10^{-18} N$\cdot$Hz$^{-\frac{1}{2}}$ for $n = 10, 20$ pulses respectively. This results agrees with the force measured in the case where ξ_0 is known.

4.6 Conclusions and outlook

In this experiment we proposed and demonstrated a method aimed at detecting small forces applied on a trapped ion mechanical oscillator. An optical dynamical decoupling sequence was applied, modulating the ion's quantum superposition phase. That in turn allowed both filtering out unwanted noise different spectrally from the force spectrum, and enhance the signal from the force itself. Using this method, we demonstrated an increased force sensitivity far from the mechanical resonance. The idea presented here does not apply only for Doppler shifts measurement, and can be used to measure any effect leading to oscillating transition frequency. For example, similar method was used for measurement of laser frequency noise [34], and recently for placing bounds on theoretical model for beyond the standard model effects, such as dark matter candidates [35], where the optical transition leads to unprecedented experimental bound at large modulation frequencies.

5 Heisenberg-limited Rabi spectroscopy

The main article can be found in [36].

5.1 Abstract

The use of entangled states was theoretically shown to improve the fundamental limits of spectroscopy to beyond the standard-quantum limit. In this work, rather than probing the free evolution of the phase of a prepared entangled state with respect to a local oscillator (LO), we probe the evolution of an, initially separable, two-atom register under an Ising spin-Hamiltonian with a transverse field. The resulting correlated spin-rotation spectrum is twice as narrow as compared with uncorrelated single ion Rabi spectrum. We implement this Heisenberg-limited Rabi spectroscopy scheme on the optical-clock electric-quadrupole transition of $^{88}Sr^{+}$ using a two-ion crystal. We further show that depending on the initial state, correlated rotation can occur in two orthogonal sub-spaces of the full Hilbert space, yielding Heisenberg-limited spectroscopy of either the average transition frequency of the two ions or their frequency difference from the mean frequency. The use of correlated spin-rotations can potentially lead to new paths for clock stability improvement.

5.2 Theoretical background

5.2.1 Rabi spectroscopy

We assume a (pseudo) spin half system. We define the Rabi Hamiltonian as

$$\mathcal{H}_{\mathcal{R}} = \hbar \left[\Omega_R \sigma_y + \delta \sigma_z \right]. \tag{5}$$

This Hamiltonian generates rotations in the spin-half system $\{|\downarrow\rangle, |\uparrow\rangle\}$. Initializing the spin system in $|\downarrow\rangle$and letting it evolve under $\mathcal{H}_R$ for time $\tau_\pi = \frac{\pi}{\Omega_R}$ (π pulse) will yield some probability $\mathrm{P}\left(|\uparrow\rangle |\delta, \Omega_R\right)$ to measure our system in the state $|\uparrow\rangle$ at the end of the evolution. Scanning the parameter δ will lead to a resonance spectrum of $P\left(|\uparrow\rangle |\delta, \Omega_R\right)$, centered around $\delta = 0$. From this spectra the resonance parameters of the system (e.g the resonance laser frequency) corresponding to $\delta = 0$ can be estimated. This rotation can be visualized on a Bloch sphere. A general pictorial rotation in the Bloch sphere for an arbitrary initial state is shown in Fig. 13.

The spectral form of $\mathrm{P}\left(|\uparrow\rangle |\delta, \Omega_R\right)$ is presented in Fig. 14. For a π pulse, the functional form for the spectrum is

$$P\left(|\uparrow\rangle |\delta, \Omega_R\right) = \frac{\sin\left(\frac{\pi}{2}\sqrt{1+\left(\frac{\delta}{\Omega_R}\right)^2}\right)}{\sqrt{1+\left(\frac{\delta}{\Omega_R}\right)^2}}. \tag{6}$$

A main characteristic of this spectral shape is the fact that its width is dictated by Ω_R.

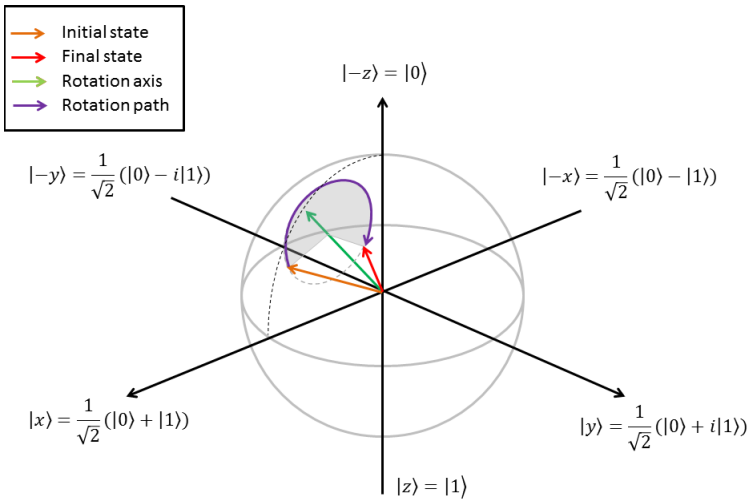

Figure 13: Bloch sphere representation of Rabi Hamiltonian.

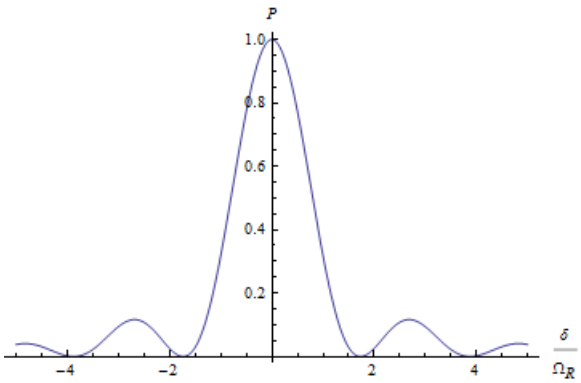

Figure 14: Spectral form of δ scan - P $(|\uparrow\rangle\,|\delta)$ - with the operation of $\mathcal{H}_R$ on the state $|\uparrow\rangle$ for operation time $\tau = \frac{\pi}{\Omega}$ (π pulse).

5.2.2 Two-spin Ising Hamiltonian

We assume a system composed of two $\frac{1}{2}$ spins. We denote the two basis states of each spin as $\{|\downarrow\rangle, |\uparrow\rangle\}$. The spins can be initialized in any of the states $\{|\downarrow\downarrow\rangle, |\downarrow\uparrow\rangle, |\uparrow\downarrow\rangle, |\uparrow\uparrow\rangle\}$. The Hamiltonian governing the system evolution is an Ising-type interaction Hamiltonian with a transverse field:

$$\mathcal{H}_I = \hbar\left[\Omega_I \sigma_y \otimes \sigma_y + \delta_+ \left(\sigma_z \otimes I + I \otimes \sigma_z\right) + \delta_- \left(\sigma_z \otimes I - I \otimes \sigma_z\right)\right], \qquad (7)$$

where $\sigma_x, \sigma_y, \sigma_z$ are the Pauli matrices, I is the 2×2 unity matrix and $\hbar$ is Planck constant divided by 2π. The term $\Omega_I \sigma_y \otimes \sigma_y$ represent an Ising type interaction between the spins. The term δ_+ represents the two-spin-average magnetic field along the z axis, and the term δ_- accounts for half the magnetic field difference between the two spins. The Hamiltonian $\mathcal{H}_I$ commutes with the operator $\sigma_z \otimes \sigma_z$. Therefore, it conserves the parity of the state. Stated differently, the Hamiltonian $\mathcal{H}_I$ does not mix the even $\{|\downarrow\downarrow\rangle, |\uparrow\uparrow\rangle\}$ and the odd $\{|\downarrow\uparrow\rangle, |\uparrow\downarrow\rangle\}$ subspaces. In addition, the even and odd subspaces are degenerate under the operation of $(\sigma_z \otimes I - I \otimes \sigma_z)$ and $(\sigma_z \otimes I + I \otimes \sigma_z)$ respectively. As a result, superpositions of the states $\{|\downarrow\downarrow\rangle, |\uparrow\uparrow\rangle\}$ ($\{|\downarrow\uparrow\rangle, |\uparrow\downarrow\rangle\}$) are invariant to change in δ_- (δ_+).

5.2.3 Correlated two spin Rabi spectroscopy and the Heisenberg limit

The Hamiltonian $\mathcal{H}_I$ can be used as a spectroscopic tool, similar to $\mathcal{H}_R$. Depending on the initialized state, this spectroscopic tool can be sensitive to the average frequency between the ions, or to the difference between the two ions' frequencies. Initialized in the $|\downarrow\downarrow\rangle$ state and operating the Hamiltonian for time $\tau = \frac{\pi}{\Omega_I}$, leads to a probability to measure the state $|\uparrow\uparrow\rangle$ denoted as $\mathrm{P}\left(|\uparrow\uparrow\rangle |\delta_+, \Omega_I\right)$. The function $\mathrm{P}\left(|\uparrow\uparrow\rangle |\delta_+, \Omega_I\right)$ is a spectrum in δ_+, centered around $\delta_+ = 0$. Due to the operator $(\sigma_z \otimes I + I \otimes \sigma_z)$, this spectrum is narrower compared to the single spin case of Eq. 6 by a factor of two. The spectral shape will be given now by

$$P\left(|\uparrow\uparrow\rangle |\delta_+, \Omega_I\right) = \frac{\sin\left(\frac{\pi}{2}\sqrt{1+\left(\frac{2\delta_+}{\Omega_I}\right)^2}\right)}{\sqrt{1+\left(\frac{2\delta_+}{\Omega_I}\right)^2}},$$

and a comparison between $P\left(|\uparrow\rangle |\delta, \Omega_R\right)$ and $P\left(|\uparrow\uparrow\rangle |\delta_+, \Omega_I\right)$ for $\Omega_I = \Omega_R$ is presented in Fig. 15.

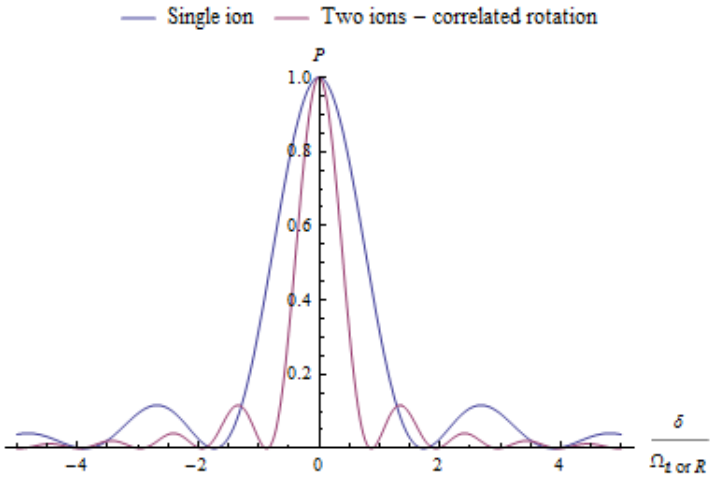

Figure 15: Comparison between Rabi spectrum of a single ion and two correlated ions for $\Omega_I = \Omega_R$.

The theory above is also valid when working in the odd subspace, by replacing

$$|\downarrow\downarrow\rangle \rightarrow |\downarrow\uparrow\rangle\,,$$
$$|\uparrow\uparrow\rangle \rightarrow |\uparrow\downarrow\rangle\,,$$
$$\delta_+ \rightarrow \delta_-.$$

This factor of 2 reduction in width in Fig. 15 is a manifestation of the Heisenberg-limit. If we would use the Hamiltonian $\mathcal{H}_R \otimes \mathcal{H}_R$ for the two spin case, that is, operate $\mathcal{H}_R$ on each spin in an uncorrelated manner, it would be equivalent to performing the same experiment on one spin twice. Taking the average of the two spin measurement outcomes will yield uncertainty improvement that scales as $\sqrt{2}$. This corresponds to the standard quantum limit (SQL). However, in the correlated case, the use of correlation between the spins leads to a reduction of the uncertainty that scales as 2, which is a factor of $\sqrt{2}$ improvement over the SQL. That is the Heisenberg limit, which is a fundamental limit in quantum mechanics. We define an experimental measure for the closeness of a spectrum to the Heisenberg limit by α in the fitting function

$$P\left(|\text{State}\rangle\,|\delta,\Omega\right) = A\frac{\sin\left(\frac{\Omega\tau}{2}\sqrt{1+\left(\frac{\alpha\delta}{\Omega}\right)^2}\right)}{\sqrt{1+\left(\frac{\alpha\delta}{\Omega}\right)^2}}, \tag{8}$$

where Ω is the correct Rabi frequency, τ is the pulse duration, δ is the parameter being scanned and $1 < \alpha < 2$ is a parameter defining the degree above the SQL for the measurement (2 corresponds to Heisenberg limit). A is a fit parameter correcting for experiment imperfections.

5.3 Experimental methods

5.3.1 Experimental apparatus

In our experiment we used two trapped $^{88}Sr^{+}$ions in a linear Paul trap. The pseudo-spins levels are $\left|S,-\frac{1}{2}\right\rangle \equiv |\downarrow\rangle$ and $\left|J,-\frac{3}{2}\right\rangle \equiv |\uparrow\rangle$ (see notation remark in section 2). The ions are ground-state cooled, and can be addressed with the quadrupole transition $5S_{\frac{1}{2}} \rightarrow 4D_{\frac{5}{2}}$ 674 nm laser both globally and in a single addressed manner (see section 2.1.4). A simple scheme of the apparatus is shown in Fig. 16.

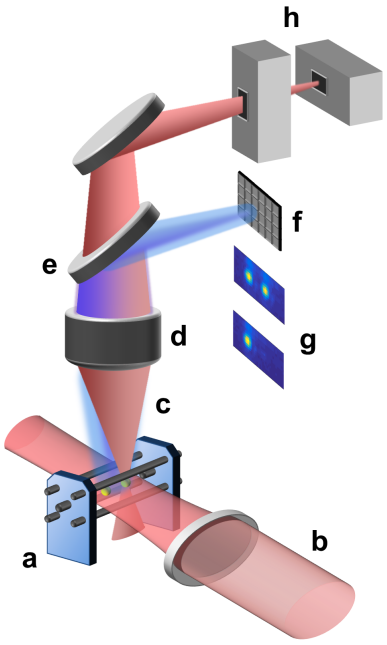

Figure 16: Experimental apparatus scheme.
Two ions trapped in a linear Paul trap **(a)** are addressed with two clock-transition laser beams. A global beam addresses both ions equally **(b)** and a tightly focused single-ion addressing beam can be tuned to address ions individually **(c)**. A magnetic field of 3.1 G is aligned along the global beam propagation direction (not marked in the figure). An objective lens **(d)** focuses the single-ion addressing beam onto the ion-crystal. The same objective lens collects fluorescence from the ions at 422 nm used for state readout. The two wavelengths are separated with a dichroic mirror **(e)**. The fluorescence light is focused on an EMCCD camera **(f)** camera images of two and a single fluorescing ions are shown **(g)**. The single-ion addressing beam passes through a double AOM system in a XY configuration, allowing fast 2D scan of the beam's position and fast shifting of the beam from one ion to the another **(h)**.

The ions are detected using an EMCCD camera. Each of the states $|\downarrow\downarrow\rangle, |\downarrow\uparrow\rangle, |\uparrow\downarrow\rangle, |\uparrow\uparrow\rangle$ can be individually detected on the camera.

5.3.2 Hamiltonian $\mathcal{H}_I$ generation

We generate the evolution described by the Hamiltonian $\mathcal{H}_I$ by realizing Mölmer-Sörensen interaction [20]. The two ions are illuminated by the 674 nm global beam operating at two frequencies defined as

$$\omega_{\pm} = \omega_0 \pm (\nu + \varepsilon) - \delta,$$

where $\omega_0 = \frac{\omega_0^1 + \omega_0^2}{2}$ is the average of clock transition carrier frequency of the ion 1 and ion 2, ν is the axial trap frequency, ε is a symmetric detuning and δ is an asymmetric detuning from the sideband transitions. The laser frequency configuration and the relevant ion levels are shown in Fig. 17. The laser coupling to the red and blue sidebands has the coupling constant $\eta\tilde{\Omega}$, where η is the Lamb-Dicke parameter and $\tilde{\Omega}$ is the carrier laser coupling of the $|\downarrow\rangle \leftrightarrow |\uparrow\rangle$ transition. When taking the limit of $\varepsilon \gg \eta\tilde{\Omega}$, the laser is largely-detuned from the sideband and the single-ion coupling is suppressed. The two ions' coupling is then dominant, and we get the two-ion Ising coupling $\Omega_I = \frac{\left(\eta\tilde{\Omega}\right)^2}{\varepsilon}$. We define the center laser frequency as the average $\omega_L = \frac{\omega_+ + \omega_-}{2} = \omega_0 - \delta$. Under these notations, $\delta_+ = \omega_0 - \omega_L$, and $\delta_- = \frac{\omega_0^1 - \omega_0^2}{2}$.

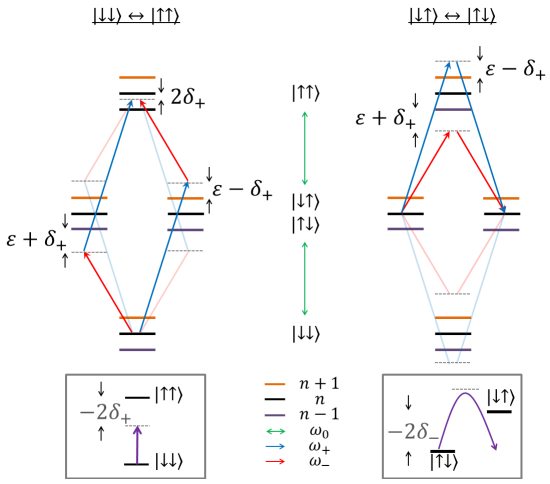

Figure 17: Mölmer-Sörensen laser configuration.
The horizontal lines color code refers to different harmonic oscillator (trap) states, while the vertical arrows' color code mark the laser frequencies. The bottom framed left (right) inset show the effective coupling between the even (odd) subspace's levels for very large ε. When ε is large, the levels of the odd (even) subspace can be adiabatically eliminated, leaving the system as an approximate two level system. The even (odd) subspace can then be used as a probe for $\delta_+(\delta_-)$.

5.3.3 Creating clock-transition frequency difference between the two ions

In order to vary the parameter δ_- we used the single-addressing 674 nm beam operating off-resonance by $\delta_{ls} \approx 3.5$ MHz from the clock transition. The beam was illuminating only one ion at a time, and light-shifting its frequency. The light-shift magnitude is $\Delta_{ls} = \frac{(\Omega_{ls})^2}{4\delta_{ls}}$, where Ω_{ls} is the Rabi frequency for the carrier transition of the light-shifting beam. By changing its power, that is, changing Ω_{ls}, we could scan Δ_{ls}, and in turn scan the difference of the ions' transition frequency. We note that in this method we change both the ions' average frequency corresponding to $\delta_+ = \frac{\Delta_{ls}}{2}$ and the frequency difference corresponding to $\delta_- = \frac{\Delta_{ls}}{2}$. In this work we scanned $\Delta_{ls}/2\pi$ in the range of $\approx 0 - 800$ Hz, corresponding to $\Omega_{ls}/2\pi$ in the range of $\approx 0 - 100$ kHz.

5.4 Results

5.4.1 Validity of our model - correlated Rabi Oscillations

The first experiment we performed was a correlated Rabi oscillations in both the even and odd subspaces. This results verifies that we are in fact applying a good approximation to $\mathcal{H}_I$ on our two pseudo-spin system, and that $\mathcal{H}_I$ indeed

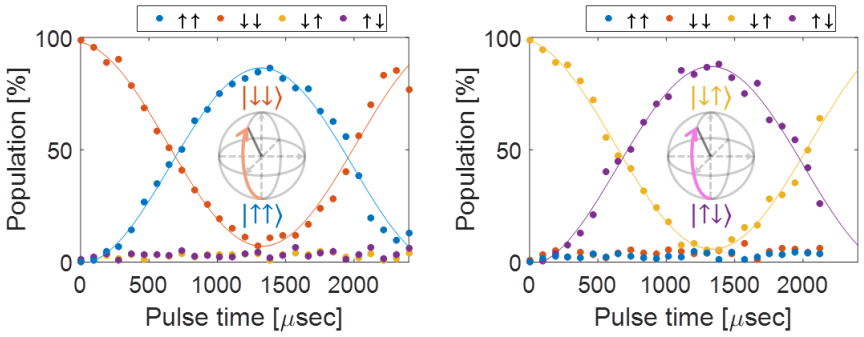

(a) Even subspace oscillations.

(b) Odd subspace oscillations.

Figure 18: Correlated Rabi oscillations.
The figure shows the population of the corresponding subspace oscillating while the other subspace population remains small. The latter is a result of adiabatic elimination. Each subspace oscillation can be viewed as a rotation in a Bloch-sphere of the corresponding two-level system.

does not mix between the even and odd subspaces. We initialized our spin system both in the $|\downarrow\downarrow\rangle$ and in the $|\downarrow\uparrow\rangle$ states, and applied our Mölmer-Sörensen bi-chromatic beam for various times, and after each experiment we measured the state of the ions, and we averaged over 300 realizations. Here we chose $\varepsilon = 6 \times \eta\Omega \approx 17.4$ kHz. The results are shown in Fig. 18. From the results, it appears that the oscillation contrast is about 90%, meaning that 10% of the population escaped the specific subspace.

5.4.2 Insensitivity to different parameters in the odd and even subspaces

The next experiment was aimed at testing the different subspaces as spectroscopy-probes for the different parameters δ_+ and δ_-. Here we showed that the even (odd) subspace is sensitive to $\delta_+(\delta_-)$ while being insensitive to $\delta_-(\delta_+)$. We first performed a large scan of δ_+ for an initial state $|\downarrow\downarrow\rangle$ and $|\downarrow\uparrow\rangle$. We performed a π pulse, for values of δ_+ from $-\varepsilon$ to ε. In this scan $\varepsilon = 2\pi \times 25.5$ kHz $\approx 10\eta\Omega$. The scan results appear in Fig. 19.

From Fig. 19a it is apparent that indeed the even subspace is sensitive to δ_+, the average ion frequency. This sensitivity is shown by the sharp peak and dip in the population of $|\downarrow\downarrow\rangle$ and $|\uparrow\uparrow\rangle$ respectively. In contrast, in Fig. 19b the same scan interval shows a flat response, proving that indeed the odd subspace is insensitive to δ_+. This sensitivity spans over a large set of δ_+ values between $\pm\varepsilon$. The response at δ_+ values on the scale of ε is due to the fact that when δ_+ approaches $\pm\varepsilon$, one of the global laser beam frequencies is driving a single-ion motional sideband. This effect is then dominating the ions evolution, and the approximation of $\mathcal{H}_I$ does not hold.

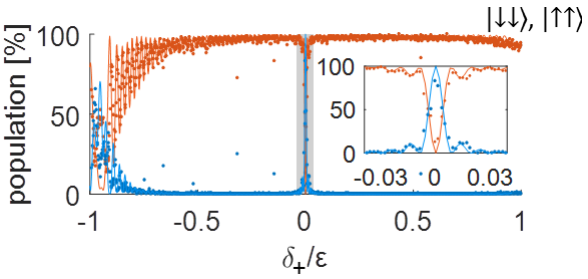

(a) δ_+ scan results when initializing in $|\downarrow\downarrow\rangle$ and measuring the population in $|\uparrow\uparrow\rangle$ (blue) and $|\downarrow\downarrow\rangle$ (orange).

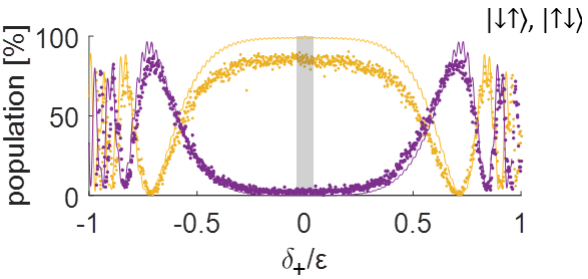

(b) δ_+ scan results when initializing in $|\downarrow\uparrow\rangle$ and measuring the population in $|\uparrow\downarrow\rangle$ (yellow) and $|\downarrow\uparrow\rangle$ (purple).

Figure 19: Large δ_+ scan for initial state $|\downarrow\downarrow\rangle$ and $|\downarrow\uparrow\rangle$. The data was shifted to be symmetric around $\delta_+ = 0$, and the solid lines are calculation results with no fit parameters. The discrepancy between simulation and data in is due to in population leaking to the complementary subspace owing to experimental imperfections. The shaded gray area illustrates the difference in sensitivity to δ_+ in both subspaces, and the inset is a magnification of that scan interval. In both measurements $\varepsilon = 2\pi \times 25.5\text{kHz} \approx 10\eta\Omega$.

We continued by testing the sensitivity to δ_-. In this experiment, we performed a scan of δ_- and δ_+, and we plot a two dimensional map of these two, when initializing in $|\downarrow\downarrow\rangle$ and in $|\downarrow\uparrow\rangle$. The results are presented in Fig. 20.

In Fig. 20a and 20b, we show that the even subspace is insensitive to pure difference between the ions' frequencies. However, in our system we did not scan δ_- by itself, but scanned Δ_{ls} using our light-shift method. Therefore we scanned both $\delta_- = \frac{1}{2}\Delta_{ls}$ and $\delta_+ = \left|\frac{1}{2}\Delta_{ls}\right|$ together. The positive values of δ_- originate in light-shifting one of the ions, and the negative values comes from light-shifting the other. That creates the same average frequency shift, but opposite frequency difference. From the symmetry of these maps around $\frac{1}{2}\Delta_{ls} = 2\pi \times 40$ Hz we can infer that indeed the even subspace is insensitive to δ_-. The 40 Hz offset comes from a constant frequency difference between the ions resulting from stray magnetic field gradient. Fig. 20c and 20d show the sensitivity of the odd subspace to δ_-. It shows a peak centered at $\Delta_{ls} = 2\pi \times 40$ Hz which is

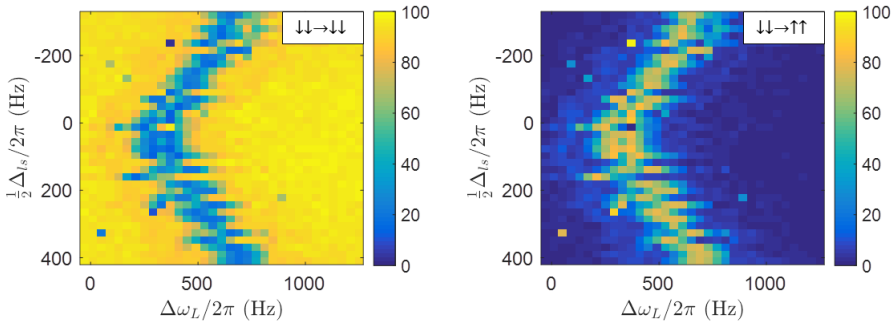

(a) Initialize in $|\downarrow\downarrow\rangle$ and measuring in $|\downarrow\downarrow\rangle$. (b) Initialize in $|\downarrow\downarrow\rangle$ and measuring in $|\uparrow\uparrow\rangle$.

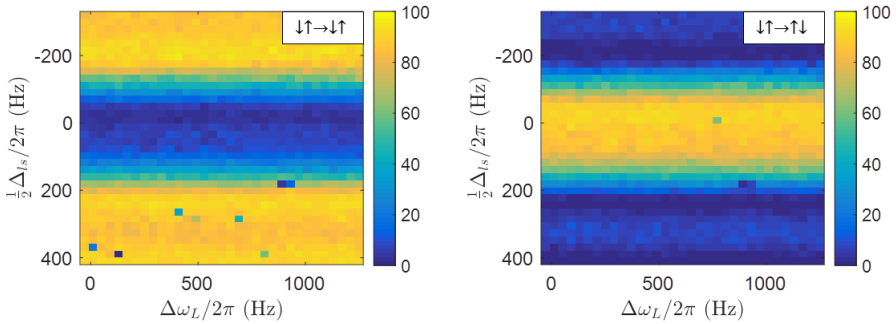

(c) (d)

Figure 20: Sensitivity to δ_- for initial state $|\downarrow\downarrow\rangle$ and $|\downarrow\uparrow\rangle$.

insensitive to δ_+.

5.4.3 Uncertainty close to the Heisenberg limit

The final aspect of the Hamiltonian $\mathcal{H}_I$ we wanted to demonstrate is the uncertainty reduction in the resonance frequency estimation with respect to a single ion experiment. In addition, we wanted to show that both δ_+ and δ_- are measured with Heisenberg-limited uncertainty using the even and odd subspaces respectively. The measurement was implemented by operating with $\mathcal{H}_I$ for a π pulse time when initializing at $|\downarrow\downarrow\rangle, |\downarrow\uparrow\rangle$, and scanning delicately the parameter δ_+ and δ_-. The results are shown in Fig. 21.

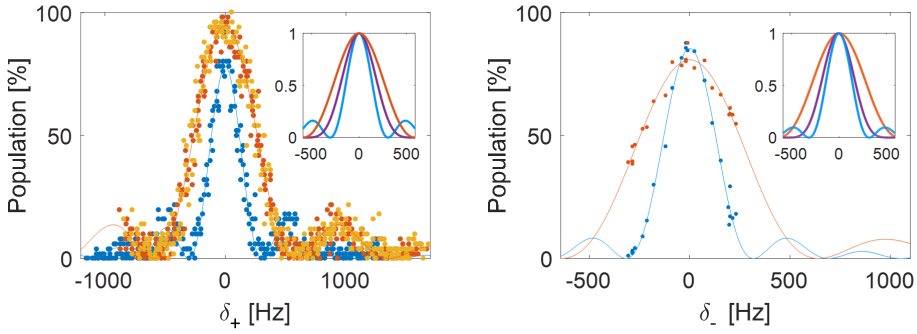

(a) Frequency average.

(b) Frequency difference.

Figure 21: Heisenberg limited spectroscopy of the average and difference between the ions' frequencies.
Heisenberg-limited spectroscopy. **(a)** Comparison between the spectra for the cases of a single ion $|\downarrow\rangle \rightarrow |\uparrow\rangle$ (red and orange full circles for the right and left ion respectively) and two ions correlated spectroscopy $|\downarrow\downarrow\rangle \rightarrow |\uparrow\uparrow\rangle$ (blue full circles). All spectra were shifted to center around $\delta_+ = 0$ due to small shifts ($10'$s of Hz) and fitted to the model of Eq. 8 (solid blue line). **(b)** Comparison between the frequency-difference spectra of two ions in an uncorrelated (red full circles) and a correlated (blue full circles) measurement. In the uncorrelated case the average frequency of the two ions was measured on each ion separately as a function of δ_-, and both populations were averaged to give the measurement result (See supplementary material). The spectra were also shifted to center around $\delta_- = 0$. **Insets**: Comparison between the normalized uncorrelated case fit, the product of the two single ion fits in the uncorrelated case and the normalized correlated fit for both δ_+ and δ_- scans. As seen, the single ion case is the widest, but holds two data points for each scanned parameter value, and therefore estimation of the resonance frequency can be performed with $\sqrt{2}$ reduction in the uncertainty. This can be manifested spectrum-wise by taking a spectrum of the probability of both ions excited (solid purple line). In this case the spectrum is $\sqrt{2}$ narrower than the single ion case, but not all measurements are included, thus matching the resonance frequency uncertainty to the two, uncorrelated, ions case. The correlated case clearly yields the narrowest spectrum with the same number of measurements and therefore a $\sqrt{2}$ improvement in the frequency estimation uncertainty due to shot-noise.

Due to magnetic field drifts between experiments, these results are composed of ten different scans, where for each parameter δ_+ or δ_- value 50 experimental repetitions were averaged. The data of each scan was fit, and then shifted such that its peak corresponded to $\delta_+ = 0$ and $\delta_- = 0$. Therefore, only an estimate for the spectrum width can be extracted from the results in Fig. 21. By fitting the spectra presented in Fig. 21a to Eq. 8 we get $\alpha = 1.92 \pm 0.02$ for the correlated spectrum and $\alpha = 1.01 \pm 0.01$ for the uncorrelated spectrum. This

validates our understanding of the theory, and places our correlated rotation close to the Heisenberg limit for uncertainty.

The fit of the spectra in Fig. 21b gives $\alpha = 1.78 \pm 0.03$ for the correlated spectrum and $\alpha = 0.88 \pm 0.02$ for the uncorrelated case. Here again the fit suggests that the correlated case is better than the SQL, however this fit is in less agreement with theory due to lower number of measured points and intensity noise in the single addressing beam.

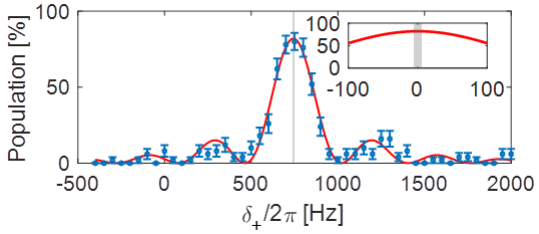

(a) Spectrum of two correlated ions

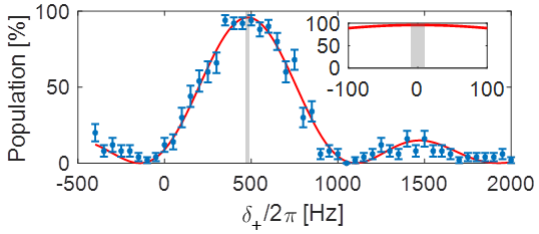

(b) Spectrum of ion 1

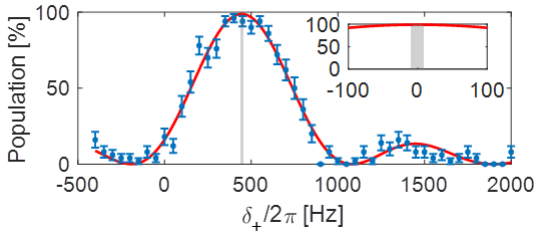

(c) Spectrum of ion 2

Figure 22: **Two-ion correlated and single ion Rabi spectroscopy.(a,b,c)** Rabi spectroscopy in the two ion correlated case, single ion for ion 1 and ion 2 respectively. The data (blue full circles) is taken from a single frequency scan out of the ten superimposed in figure 21.

5.4.4 Demonstration of improved sensitivity

In order to prove our claim for possible spectroscopic improvement due to our Heisenberg limited spectroscopy, we compared two frequency scans across our ions' resonance out of the ten mentioned in section 5.4.3 and estimated the error in the center frequency measured with a single ion and a correlated two ion spectroscopy. The results are shown in Fig. 22.

Here, both uncorrelated and correlated experiments' pulse time is equal. Each frequency point is the average over 50 experimental realizations, and is assumed to be projection noise limited. The shaded area marks the 95\% confidence uncertainty in the center of the spectrum from a maximum-likelihood fit. This interval is 10.3 Hz for the correlated case, and is compared to 21.3 Hz and 18.7 Hz for ion 1 and ion 2 respectively, proving improvement in the uncertainty for the correlated case. the insets show the corresponding theoretical fit shifted to be centered around zero for a 200 Hz span, emphasizing the smaller uncertainty in the correlated case by the shaded gray area.

Part IV
Precision measurements involving radio-frequency-based methods - the J_z^2 trilogy

6 Introduction

6.1 Section overview

In this part I will describe three different proposals and experiments, employing large-spin dynamical decoupling sequences - a tool that was developed by me and my group, to measure and cancel energy shifts in an atomic level with total spin higher than $\frac{1}{2}$. In section 7, I will present a method to measure quadrupole shifts in the excited state of an ion trapped in a linear Paul trap. Using this scheme we measured our ion's clock-transition excited-state quadrupole moment to the best precision known today. In section 8 I will describe a collaboration with several theoretical and experimental groups from Australia and the United States, in which we proposed and demonstrated an experimental method to measure frame-dependent shifts in the excited state of an atom. As current theory predicts that the energy levels of an atomic level should be space-orientation independent, this proposal aims at finding or placing bounds on beyond the standard model theories. In section 9 I will report on an experimental approach to cancel the quadrupole and linear Zeeman shift in clock transition. Such shifts are inhomogeneous, and thus are among the reasons for the common use of only single-ion frequency references in atomic-ions based optical clocks. Diminishing this inhomogeneity help paving the path towards the use of multiple ion chains, potentially leading to more precise and stable clock operation.

6.2 Origin of $\boldsymbol{J^2 - 3J_z^2}$ energy term

We assume a spin J, with a Hamiltonian respecting the mutual eigenvectors of $\overrightarrow{\boldsymbol{J}}^2$ and $\boldsymbol{J}_z$: $|J,m\rangle|_{m=-J,-J+1\ldots J-1,J}$. A tensor coupling in the form of

$$\delta H = \sum_{i,j=x,y,z} A_{ij} q_i q_j \tag{9}$$

is added to the Hamiltonian, where $q_i = \{q_x, q_y, q_z\}$ are the components of a 3-dimensional spacial vector-operator (e.g. position or momentum of a particle) and A_{ij} are coupling constants that are small compared to other parameters in the Hamiltonian, such that δH can be treated as a small perturbation. δH can be rewritten in a different way:

$$\delta H = \sum_{k\in\{-2,-1,0,1,2\}} \tilde{A}_k T_k^{(2)} \tag{10}$$

where $\tilde{A}_k$ are linear combinations of the $A'_{ij}s$ and $T_k^{(2)}$ are second degree spherical tensors. First order perturbation theory predicts a change of in the eigenvalues of the Hamiltonian as follows:

$$\delta E\left(m\right)=\left\langle J,m\right|\delta H\left|J,m\right\rangle =\left\langle J,m\right|\sum_{k}\tilde{A}_{k}T_{k}^{(2)}\left|J,m\right\rangle .$$

Using Wigner-Eckart theorem, we can write:

$$\left\langle J,m\right|\sum_{k}\tilde{A}_{k}T_{k}^{(2)}\left|J,m\right\rangle =\sum_{k}\tilde{A}_{k}\underbrace{\left\langle J,m,2,k\left|J,m\right.\right\rangle }_{\text{Clebch-Gordan}}\left\langle J\right\|T^{(2)}\left\|J\right\rangle ,$$

where $\left\langle J\right\|T^{(2)}\left\|J\right\rangle$ is the reduced matrix element that is independent of k. From here we can see that only $k=0$ contributes, since in order for the term to not vanish, we need to have a match between the two quantum numbers from the left and right hand sides: $m+k=m\rightarrow k=0$. Therefore, we can write that the only operator contributing to the energy shift is

$$\delta H_{eff}=\tilde{A}_{0}T_{0}^{(2)}=\tilde{A}_{0}\left(\overrightarrow{q}^{2}-3q_{z}^{2}\right).$$

In angular momentum basis, this operator takes the form:

$$\delta H_{eff}=\sum_{m_{1},m_{2}}\left|J,m_{1}\right\rangle \left\langle J,m_{1}\right|\tilde{A}_{0}T_{0}^{(2)}\left|J,m_{2}\right\rangle \left\langle J,m_{2}\right|=$$

$$=\tilde{A}_{0}\sum_{m_{1},m_{2}}\left\langle J,m_{1},2,0\left|J,m_{2}\right.\right\rangle \left\langle J\right\|T_{0}^{(2)}\left\|J\right\rangle \left|J,m_{1}\right\rangle \left\langle J,m_{2}\right|=$$

$$=\tilde{A}_{0}\sum_{m_{1},m_{2}}\underbrace{\left\langle J,m_{1},2,0\left|J,m_{2}\right.\right\rangle }_{0\text{ unless }m_{1}=m_{2}}\left\langle J\right\|T_{0}^{(2)}\left\|J\right\rangle \left|J,m_{1}\right\rangle \left\langle J,m_{2}\right|=$$

$$=\tilde{A}_{0}\sum_{m}\left\langle J,m,2,0\left|J,m\right.\right\rangle \left\langle J\right\|T_{0}^{(2)}\left\|J\right\rangle \left|J,m\right\rangle \left\langle J,m\right|$$

Therefore, we can conclude that in the angular momentum basis δH_{eff} is diagonal. In addition, the Clebch-Gordan coefficients in the diagonal elements are in the form

$$\left\langle J,m,2,0\left|J,m\right.\right\rangle =f\left(J\right)\left[J\left(J+1\right)-3m^{2}\right],$$

where f is some function of J. Taking all of the above, we obtain the operator form of δH_{eff}:

$$\delta H_{eff}=\kappa\left(J\right)\left(\overrightarrow{\boldsymbol{J}}^{2}-3\boldsymbol{J}_{z}^{2}\right). \tag{11}$$

where $\kappa=\tilde{A}_{0}f\left(J\right)\left\langle J\right\|T_{0}^{(2)}\left\|J\right\rangle$.

The derivation above leads to the conclusion that any small perturbation in the form of Eq. 9, can be treated to first order as the total angular momentum operator in Eq. 11.

6.3 Hamiltonian description of a spin $J > \frac{1}{2}$ under magnetic field with a δH_{eff} term

6.3.1 Free evolution

We assume a spin $J > \frac{1}{2}$ system, with an associated magnetic moment $\overrightarrow{\boldsymbol{\mu}} = \gamma_J \overrightarrow{\boldsymbol{J}}$. The spin is coupled to magnetic field $\overrightarrow{B} = B_z \hat{z}$ at its position, and therefore evolves according to the free linear magnetic Hamiltonian

$$\boldsymbol{H}_l = \gamma_J B_z \boldsymbol{J}_z. \tag{12}$$

In addition, we assume that the spin interacts with its environment in the form of Eq. 9, and therefore an additional quadratic term in $\boldsymbol{J}_z$ in the form of Eq. 11 is added:

$$\boldsymbol{H}_q = \kappa \left(\overrightarrow{\boldsymbol{J}}^2 - 3\boldsymbol{J}_z^2 \right). \tag{13}$$

The total free evolution Hamiltonian is the sum of the terms in Eq. 12 and Eq. 13:

$$\begin{aligned} \boldsymbol{H}_f &= \boldsymbol{H}_l + \boldsymbol{H}_q = \\ &= \gamma_J B_z \boldsymbol{J}_z + \kappa \left(\overrightarrow{\boldsymbol{J}}^2 - 3\boldsymbol{J}_z^2 \right). \end{aligned} \tag{14}$$

6.3.2 Drive operation term

We add an experimental control to the Hamiltonian, in the form of a magnetic AC drive, with frequency ω_{RF}^J, phase ϕ_J and amplitude $B_x(t)\,\hat{x}$. The drive adds the time-dependent Hamiltonian term

$$\boldsymbol{H}_d = \gamma_J B_x(t) \cos\left(\omega_{RF}^J t - \phi_J\right) \boldsymbol{J}_x.$$

We denote $\gamma_J B_x(t) = 2\hbar\Omega^J(t)$, where $\Omega^J(t)$ is the time-dependent spin J Rabi frequency. We now limit ourselves to two operation modes of $B(t)$, $B(t) = 0$ and $B(t) = B_0$, corresponding to $\Omega^J(t) = 0$ and $\Omega^J(t) = \Omega_0^J$. In addition, we assume that

$$\frac{\gamma_J B_z}{\hbar} - \omega_{RF}^J = \delta_J \ll \Omega_0^J \ll \frac{\gamma_J B_z}{\hbar} + \omega_{RF}^J. \tag{15}$$

The full spin J Hamiltonian reads

$$\begin{aligned} \boldsymbol{H}_J &= \boldsymbol{H}_{fe} + \boldsymbol{H}_d = \\ &= \gamma_J B_z \boldsymbol{J}_z + \kappa \left(\overrightarrow{\boldsymbol{J}}^2 - 3\boldsymbol{J}_z^2 \right) + 2\hbar\Omega^J(t) \cos\left(\omega_{RF}^J t - \phi_J\right) \boldsymbol{J}_x. \end{aligned} \tag{16}$$

6.3.3 Interaction picture Hamiltonian

We now move to the interaction picture with respect to the drive, i.e. with respect to the Hamiltonian $\tilde{\boldsymbol{H}} = \hbar\omega_{RF}^J \boldsymbol{J}_z$. The interaction Hamiltonian reads:

$$\tilde{\boldsymbol{H}}_J = e^{-i\frac{\tilde{\boldsymbol{H}}}{\hbar}t} \boldsymbol{H}_J e^{i\frac{\tilde{\boldsymbol{H}}}{\hbar}t} - \tilde{\boldsymbol{H}} =$$

$$= \gamma_J B_z \boldsymbol{J}_z + \kappa \left(\overrightarrow{\boldsymbol{J}}^2 - 3\boldsymbol{J}_z^2 \right) + 2\hbar\Omega^J(t) \cos\left(\omega_{RF}^J t - \phi_J\right) e^{-i\omega_{RF}^J t \boldsymbol{J}_z} \boldsymbol{J}_x e^{i\omega_{RF}^J t \boldsymbol{J}_z} - \hbar\omega_{RF}^J \boldsymbol{J}_z =$$

$$= \hbar\delta_J \boldsymbol{J}_z + \kappa \left(\overrightarrow{\boldsymbol{J}}^2 - 3\boldsymbol{J}_z^2 \right) + 2\hbar\Omega^J(t) \cos\left(\omega_{RF}^J t - \phi_J\right) \left(\cos\left(\omega_{RF}^J t\right) \boldsymbol{J}_x + \sin\left(\omega_{RF}^J t\right) \boldsymbol{J}_y \right),$$

where in the last step we used the fact that $e^{-i\omega_{RF}^J t \boldsymbol{J}_z} \boldsymbol{J}_x e^{i\omega_{RF}^J t \boldsymbol{J}_z}$ acts as a rotation of $\boldsymbol{J}_x$ around z. According to Eq. 15we can take the Rotating Wave Approximation (RWA), and neglect terms that rotate with frequency $2\omega_{RF}^J$. we are left with the interaction Hamiltonian

$$\boldsymbol{H}_J^{int} = \hbar\delta_J \boldsymbol{J}_z + \hbar\kappa \left(\overrightarrow{\boldsymbol{J}}^2 - 3\boldsymbol{J}_z^2 \right) + \hbar\Omega^J(t) \left(\cos(\phi_J) \boldsymbol{J}_x + \sin(\phi_J) \boldsymbol{J}_y \right). \quad (17)$$

7 Atomic Quadrupole Moment Measurement Using Dynamic Decoupling

Published article can be found in [13].

7.1 Abstract

We present a method that uses multi-level dynamic decoupling of trapped $^{88}Sr^+$ to distinguish small frequency shifts that depend on m_J^2 , where m_J is the projection of angular momentum J along the quantization axis, from large noisy shifts that are linear in m_j, such as those due to magnetic field noise. Using this method we measured the electric-quadrupole moment of the $4D_{\frac{5}{2}}$ level in $^{88}Sr^+$ to be $2.973^{+0.026}_{-0.033} e\, a_0^2$. Our measurement improves the uncertainty of this value by an order of magnitude compared to previous measurements and thus helps mitigate an important systematic uncertainty in $^{88}Sr^+$ in based optical atomic clocks. In addition, our measurement verifies complicated many-body quantum calculations.

7.2 Atomic quadrupole shift

7.2.1 Electric energy multipole expansion

The electric energy of a charge distribution $\rho(\boldsymbol{x})$ centered around the point $\boldsymbol{x} = 0$ and under an electric potential $V(\boldsymbol{x})$ is given by:

$$U = \int \rho(\overrightarrow{x})\, V(\overrightarrow{x})\, d\overrightarrow{x} =$$

$$= \int \rho(\overrightarrow{x}) \left(V(\overrightarrow{x})|_{\overrightarrow{x}=0} - \overrightarrow{x} \cdot \nabla V(\overrightarrow{x})|_{\overrightarrow{x}=0} + \sum_{i,j} x_i x_j \left. \frac{\partial^2 V}{\partial x_i \partial x_j} \right|_{\boldsymbol{x}=0} + ... \right) d\overrightarrow{x}$$

We write the first three terms of the expansion:

$$U_{\text{mono}} = V(\overrightarrow{x})|_{\overrightarrow{x}=0} \underbrace{\int \rho(\overrightarrow{x})\, d\overrightarrow{x}}_{\text{monopole moment (scalar)}}$$

$$U_{\mathrm{di}} = -\nabla V\left(\overrightarrow{x}\right)|_{\overrightarrow{x}=0} \cdot \underbrace{\int \rho\left(\overrightarrow{x}\right)\overrightarrow{x}d\overrightarrow{x}}_{\text{dipole moment (vector)}}$$

$$U_{\mathrm{quad}} = \sum_{i,j} \frac{\partial^2 V}{\partial x_i \partial x_j}\bigg|_{\overrightarrow{x}=0} \underbrace{\int \rho\left(\overrightarrow{x}\right) x_i x_j d\overrightarrow{x}}_{\text{quadrupole moment (tensor)}}$$

7.2.2 Electric energy of a bound electron in external field

We assume an electron bound in an atom positioned at $\overrightarrow{x} = 0$, under an external static electric potential $V\left(\overrightarrow{x}\right)$. The quadrupole moment of an electronic state in an atom is a measure of its deviation from perfect spherical symmetry. While S orbitals have a spherically symmetric electronic wave functions (and therefore spherical charge distribution), different orbitals e.g. the D orbital have a finite electric-quadrupole moment as their leading order deviation from spherical symmetry. Transitions in the atom will not be affected by the monopole term since all atomic levels have the same total charge, and since the atomic Hamiltonian preserves parity, no atomic eigenstate has a finite dipole moment. Hence we conclude that the leading order shifts in atomic transitions due to an external static electric potential are quadrupole shifts.

Quantizing the classical multipole expansion above, we see that the operator leading to quadrupole shifts has the form in Eq. 9:

$$\delta H_Q = \sum_{i,j} \frac{\partial^2 V}{\partial x_i \partial x_j}\bigg|_{\overrightarrow{x}=0} \boldsymbol{x}_i \boldsymbol{x}_j, \tag{18}$$

where $\boldsymbol{x}_i$ are the electron position operators with respect to the nucleus. Since quadrupole energy shifts results from external electric field gradient across the atomic-length scaled electronic charge distribution, the resulting energy shift is usually small in comparison to other shifts, e.g., the Zeeman shift. Therefore, according to section 6.2 we can treat it as a perturbation and write it in the form of Eq. 11:

$$\delta H = \hbar Q \left(\overrightarrow{\boldsymbol{J}}^2 - 3\boldsymbol{J}_z^2\right), \tag{19}$$

7.2.3 Quadrupole shift of an atomic-ion trapped in a linear Paul trap

We now focus on the case of an ion trapped in a linear Paul trap. Here, the ion is held in the trap axis ($\hat{a}$) direction by a trapping DC harmonic potential. The physical parameters in Q in this case are derived in [37]. Following this derivation, we write:

$$\hbar Q = \frac{1}{4}\frac{dE_a}{da}\frac{\Theta\left(\gamma, J\right)}{J\left(2J-1\right)}\left[3\cos^2\left(\beta\right) - 1 + \epsilon\sin^2\left(\beta\right)\cos\left(2\alpha\right)\right], \tag{20}$$

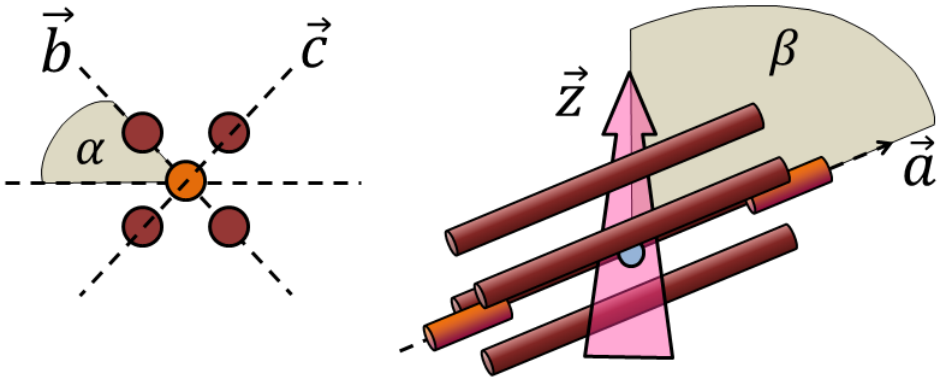

Figure 23: Trap and quantization axes and quadrupole shift relevant angles. **Left:** Trap electrode from a view parallel to $\hat{a}$, along with the definition of the angle α. The horizontal dashed line is at right angle with $\hat{a}$, and is in the plane defined by the quantization axis $\hat{z}$ and the trap axis, and the slanted dashed lines define the $\hat{b}$ and $\hat{c}$ directions of the trap. **Right:** Trap electrode from a different observation angle, showing the definition of the trap axis, the quantization axis and the angle between them, β.

where E_a is the electric field in the trap axial direction, $\frac{dE_a}{da}$ is the directional derivative of E_a in the $\hat{a}$ direction, $\Theta(\gamma, J)$ is the quadrupole moment of the γ orbital with J angular momentum and projection quantum number $m_J = J$, β is the angle between the ion's quantization axis and the trap axis, α is the angle between the x principle trap axes and the $\hat{a} - \hat{z}$ plane (in case of cylindrical symmetry of the trap around z, α can be set to zero) and ϵ is a measure of the deviation from cylindrical symmetry, i.e. difference between the x and y axes. The angles α and β and the directions $\hat{a}$ and $\hat{z}$ are shown schematically in Fig 23.

7.3 Quadrupole shift measurement scheme

7.3.1 Hamiltonian and experimental operations

We begin from a Hamiltonian similar to the one described in section 6.3.3 in Eq. 17, where we take the quadratic term to be the quadrupole shift with magnitude Q:

$$\boldsymbol{H}_J = \hbar\delta_J \boldsymbol{J}_z + \hbar Q\left(\vec{\boldsymbol{J}}^2 - 3\boldsymbol{J}_z^2\right) + \hbar\Omega^J(t)\left(\cos(\phi_J)\boldsymbol{J}_x + \sin(\phi_J)\boldsymbol{J}_y\right).$$

We now define two operation modes:

1. Free mode:
   In this mode, we do not operate the drive, meaning $\Omega(t) = 0$. The

evolution operator in this case is

$$U_f(\tau) = \exp\left[i\left(\delta_J \tau \boldsymbol{J}_z + Q\tau\left(\overrightarrow{\boldsymbol{J}}^2 - 3\boldsymbol{J}_z^2\right)\right)\right], \tag{21}$$

where τ is the evolution duration.

2. Pulse mode:
In this mode, we operate the drive with a constant amplitude $\Omega^J = \Omega_0$, and for short pulse times τ on the order of $\frac{\pi}{\Omega_0}$. Here, we neglect the evolution caused by the free part in $\boldsymbol{H}_J$ because $\frac{\delta_J}{\Omega_0} \ll 1$ and $\frac{Q}{\Omega_0} \ll 1$, and we are left with

$$U_p(\phi, \tau) = \exp\left[i\Omega_0 \tau\left(\cos(\phi)\boldsymbol{J}_x + \sin(\phi)\boldsymbol{J}_y\right)\right]. \tag{22}$$

7.3.2 Dynamical decoupling sequence building block

With the two operations from section 7.3.1, we can build a sequence that will let an initial spin state evolve only according to the quadrupole shift contribution $\hbar Q\left(\overrightarrow{\boldsymbol{J}}^2 - 3\boldsymbol{J}_z^2\right)$, and eliminate the influence of the magnetic field part $\hbar\delta_J \boldsymbol{J}_z$. We choose the RF field phase to be $\phi_+ = 0$, or $\phi_- = \pi$ such that the pulse evolution operator becomes $U_p(\phi_\pm, \tau) = \exp\left[\pm i\Omega_0 \tau \boldsymbol{J}_x\right]$. For a specific pulse time equals $\tau_p = \frac{\pi}{\Omega_0}$, we get a π pulse operation $U_p(\phi_\pm) = \exp\left[\pm i\pi \boldsymbol{J}_x\right]$. Our sequence building block is then the four operations

$$U_{bb} = U_f(\tau) U_p(\phi_-) U_f(2\tau) U_p(\phi_+) U_f(\tau).$$

In order to understand the evolution, we write it explicitly:

$$\begin{aligned} U_{bb} &= \exp\left[i\left(\delta_J \tau \boldsymbol{J}_z + Q\tau\left(\overrightarrow{\boldsymbol{J}}^2 - 3\boldsymbol{J}_z^2\right)\right)\right] ... \\ &= ...\underbrace{\exp\left[-i\pi \boldsymbol{J}_x\right] \exp\left[i\left(2v\tau \boldsymbol{J}_z + 2Q\tau\left(\overrightarrow{\boldsymbol{J}}^2 - 3\boldsymbol{J}_z^2\right)\right)\right] \exp\left[i\pi \boldsymbol{J}_x\right]}_{\text{Operator rotation of } \pi \text{ around x direction, } \boldsymbol{J}_z \to -\boldsymbol{J}_z} ... \\ &... \exp\left[i\left(\delta_J \tau \boldsymbol{J}_z + Q\tau\left(\overrightarrow{\boldsymbol{J}}^2 - 3\boldsymbol{J}_z^2\right)\right)\right] = \\ &= \exp\left[i\left(4Q\tau\left(\overrightarrow{\boldsymbol{J}}^2 - 3\boldsymbol{J}_z^2\right)\right)\right]. \end{aligned} \tag{23}$$

Here we used the fact that the operation $\exp\left[-i\pi \boldsymbol{J}_x\right] \boldsymbol{J}_z \exp\left[i\pi \boldsymbol{J}_x\right]$ is an operator rotation of $\boldsymbol{J}_z$ around the x direction with rotation angle π, therefore $\boldsymbol{J}_z \to -\boldsymbol{J}_z$. We conclude that using this pulse scheme, and under the assumption that δ is a slowly changing function with respect to this sequence duration, we can eliminate the magnetic field contribution and let an initial spin state evolve under the quadrupole part alone.

7.3.3 Full quadrupole shift experimental sequence

In order to measure the quadrupole shift of a trapped ion, i.e. evaluate Q, we can perform a Ramsey experiment using the operation in 23. The sequence is shown schematically in Fig. 24.

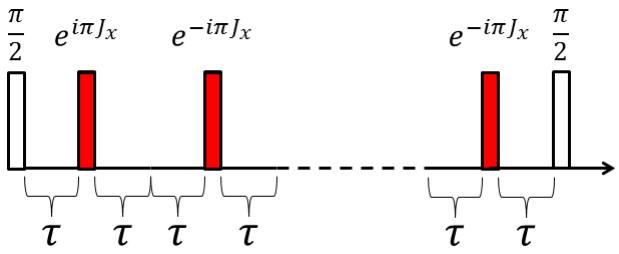

Figure 24: Quadrupole shift measurement Ramsey sequence.
The sequence begins with a $\frac{\pi}{2}$ Ramsey pulse, preparing an equal superposition of two different $|m|$ states. next, the sequence building block from section 7.3.2 is applied a number of times, so quadrupole shift phase is accumulated. Finally, a second Ramsey $\frac{\pi}{2}$ maps superposition phase into population that can be measured.

It begins by initializing the spin J state in an equal superposition of two different m states, m_1, m_2 such that $|m_1| < |m_2|$:

$$|\psi_{init}\rangle = \frac{1}{\sqrt{2}}\left(|J, m_1\rangle + |J, m_2\rangle\right).$$

This is the first $\frac{\pi}{2}$ in the Ramsey sequence. Then, we operate with the operator in Eq. 23 n times, such that:

$$|\psi\left(n\tau\right)\rangle = \exp\left[i\left(4Qn\tau\left(\vec{\boldsymbol{J}}^2 - 3\boldsymbol{J}_z^2\right)\right)\right]|\psi_{init}\rangle =$$

$$\exp\left[i\left(4Qn\tau\left(J\left(J+1\right)\right)\right)\right]\frac{1}{\sqrt{2}}\left(\exp\left[-i\left(12Qn\tau m_1^2\right)\right]|J, m_1\rangle + \exp\left[-i\left(12Qn\tau m_2^2\right)\right]|J, m_2\rangle\right).$$

Neglecting global phase, we write this state as

$$|\psi\left(n\tau\right)\rangle = \frac{1}{\sqrt{2}}\left(|J, m_1\rangle + \exp\left[-i\left(12Qn\tau\left(m_2^2 - m_1^2\right)\right)\right]|J, m_2\rangle\right).$$

The next step is mapping the phase difference between the $|J, m_1\rangle$ and $|J, m_2\rangle$ states onto their population (this is the second Ramsey $\frac{\pi}{2}$ pulse), and finally project the resulting superposition onto the $\{|J, m_1\rangle, |J, m_2\rangle\}$ basis. The final superposition phase is the result of the quadrupole shift alone, and by scanning the sequence parameters (e.g. $n\tau$ or a second Ramsey $\frac{\pi}{2}$ phase) we can measure the quadrupole shift parameter Q.

7.4 Experimental measurement of quadrupole shifts in the clock transition of $^{88}Sr^{+}$ ion trapped in a linear Paul trap

7.4.1 Quadrupole shift in $^{88}Sr^{+}$

As mentioned above, in our experiments we use a single $^{88}Sr^{+}$ ion trapped in a linear Paul trap. We performed the sequence described in sections 7.3.2 and 7.3.3 on the $|J, m_J\rangle$ manifold. The ions are held in place by a combination of oscillating and DC electric fields. The oscillating electric field's gradient averages to zero over time, and therefore contributes negligible quadrupole shift to this manifold. However, the DC potential holds the ion in a constant electric field gradient, and therefore shifts the $|J, m_J\rangle$ level frequency. From the appearance of $\boldsymbol{J}_z^2$ in Eq. 19, we see that this quadrupole shift depends on m_J quadratically. Fig. 25 shows a schematic frequency shift illustration of each $|J, m_J\rangle$ manifold in $4D_{\frac{5}{2}}$, resulting from the magnetic first order Zeeman effect and the quadrupole shift.

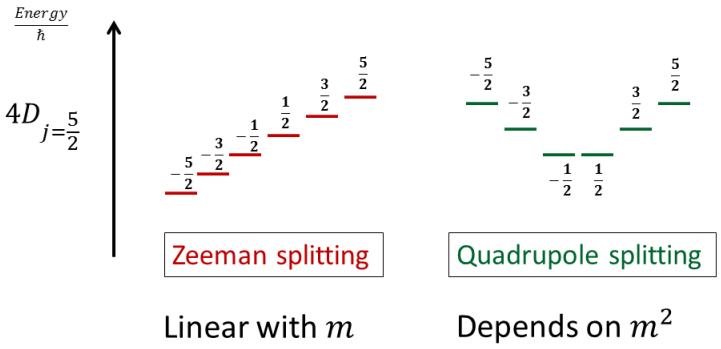

Figure 25: Schematic energy dependence on m for Zeeman and quadrupole shift.

In this experiment we operate at a constant magnetic field of typically 3 G at the ion position in order to split all orbitals to their Zeeman manifolds, resulting in a linear Zeeman frequency difference between $|J, m_J\rangle$ and $|J, m'_J\rangle$, when $|m_J - m'_J| = 1$ of roughly 5.04MHz.

7.4.2 Measurement of Ω_0

In order to perform the RF pulse operation in Eq. 22, we needed to measure Ω_0. We measured it by the following sequence: First, we optically pumped our ion to the $\left|S, -\frac{1}{2}\right\rangle$ state. Then, an optical π pulse drove the ion to the state $|J, m_J\rangle$. Next, a RF pulse with duration time τ is applied, such that the evolution operator obeys Eq. 22. Finally, a second optical π pulse drove the transition from some $|J, m'_J\rangle$, where m'_J could be equal or different from m_J, to one of the$|S, m_S\rangle$ states, followed by projective measurement on the $\{|S\rangle, |J\rangle\}$

subspace, yielding a bright (ion fluorescence) or dark (no ion fluorescence) result. The results are spin $\frac{5}{2}$ Rabi oscillations, and they are presented in Fig. 26.

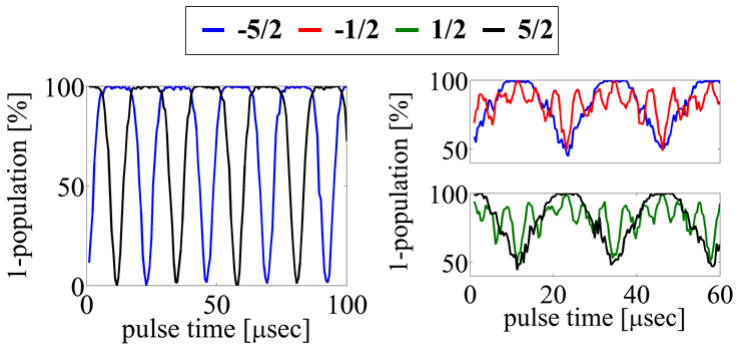

Figure 26: $J = \frac{5}{2}$ Rabi oscillations.
Left: Transition between $\left|4D_{\frac{5}{2}}, m_{\frac{5}{2}} = -\frac{5}{2}\right\rangle$ and $\left|4D_{\frac{5}{2}}, m_{\frac{5}{2}} = \frac{5}{2}\right\rangle$ induced by RF pulses. The vertical axis shows the measured population in all $4D_{\frac{5}{2}}$ manifold levels but the level stated in the legend. The population oscillated between fully be in $\left|J, -\frac{5}{2}\right\rangle$to fully be in $\left|J, \frac{5}{2}\right\rangle$, where in between the population is spread among the other levels in the manifold. **Right:** Transition between the two superpositions $\frac{1}{\sqrt{2}}\left(\left|J, -\frac{1}{2}\right\rangle + \left|J, -\frac{5}{2}\right\rangle\right)$ and $\frac{1}{\sqrt{2}}\left(\left|J, \frac{1}{2}\right\rangle + \left|J, \frac{5}{2}\right\rangle\right)$. Both top and bottom plots show data from the same experiment, separated for clarity. Both plots agree with $\Omega_0 = 2\pi \times 43$ kHz.

From these measurements we obtain $\Omega_0 \approx 2\pi \times 43$ kHz, corresponding to $\tau_\pi = \frac{\pi}{\Omega_0} = 11.63$ μs.

7.4.3 Measurement of the electric field gradient $\frac{dE_a}{da}$

Our trap is taken in the harmonic approximation, meaning its DC electric potential energy is

$$U = \frac{1}{4}\frac{dE_a}{da}\left(b^2 + c^2 - 2a^2\right)q, \tag{24}$$

where a, b, c are Cartesian coordinates, in which the a coordinate is in the direction is the trap axis and q is the electron charge. This DC potential energy translates to an axial trapping potential energy, in the form of

$$U_t = \frac{1}{2}m\omega_{\text{axial}}^2 a^2.$$

Equating the second derivative with respect to a in both forms gives

$$\frac{dE_a}{da} = \frac{m\omega_{\text{axial}}^2}{q}.$$

Therefore, knowing the mass of our ion and measuring the trapping frequency, we can obtain $\frac{dE_a}{da}$. The mass of $^{88}Sr^+$ ion is $m \approx 87.9$ amu $\approx 1.46 \times 10^{-25}$kg. We measured the trapping frequency by applying AC electric-fields with projection on the trap axial direction with different frequencies, and simultaneously measure fluorescence from the ion's 422 dipole transition. When the ion is modulated at the trap frequency, a sharp dip should be observed in the fluorescence. The results are given in Fig. 27.

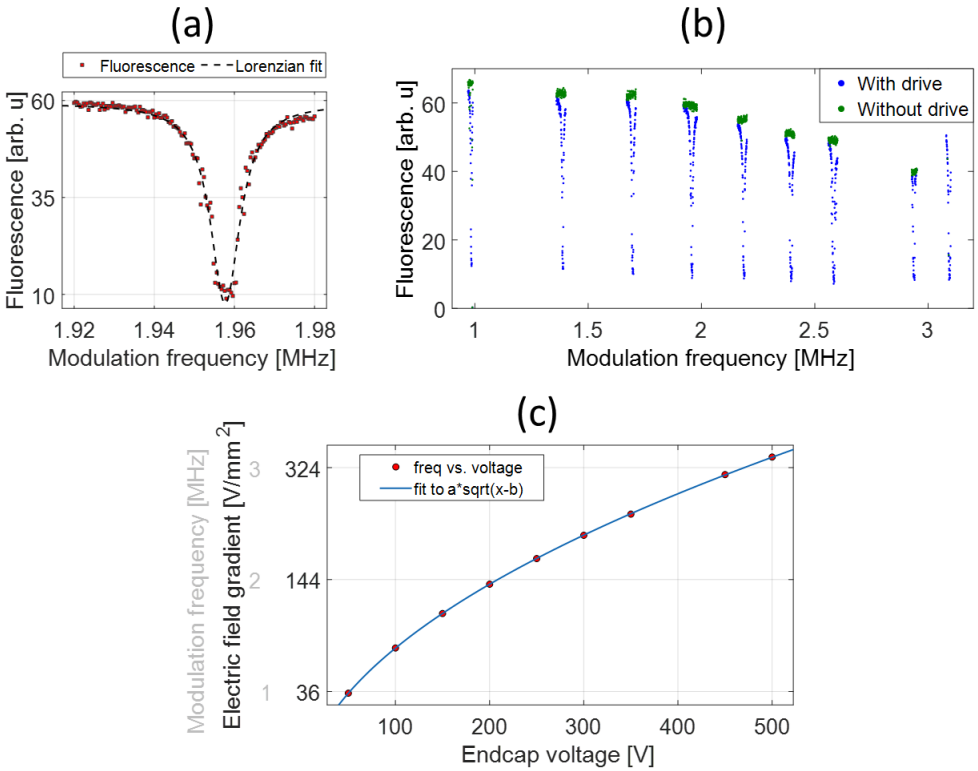

Figure 27: DC electric field gradient calibration.
(a) Ion fluorescence in a single scan of AC electric field frequency. The fluorescence drops when the modulation frequency matches the trap frequency, resulting in a sharp dip. The width of the dip is on the order of a few kHz's. **(b)** Ion fluorescence as a function of the modulation frequency for different trapping voltage on the endcap electrodes. **(c)** Final calibration matching endcap voltage to its corresponding axial trapping frequency and DC electric field gradient. The measurement agrees with the quadratic dependence of the voltage on the trapping frequency.

7.4.4 Measurement of the quantization-trap axis angle

The quantization axis is defined by a static magnetic field applied on the ion using three pairs of Helmholtz coils. Coil 1 is used for the main quantization field of about 3 G and it defines the quantization direction. Coils 2 and 3 apply weaker magnetic field and they are normally used to compensate for external stray fields. We measure the magnitude of the magnetic field at the ion position by performing RF Rabi spectroscopy on the Zeeman manifold $\left\{\left|S,-\frac{1}{2}\right\rangle,\left|S,\frac{1}{2}\right\rangle\right\}$. In the first step, we made sure that the magnetic field in the ions position is parallel to the plane spanned by the normal to coil 1 and coil 2. This was achieved by scanning the current running through coil 3 while the current in coils 1 and 2 was fixed, and finding the minimum of the Zeeman splitting. The result of this measurement appears on Fig. 28.

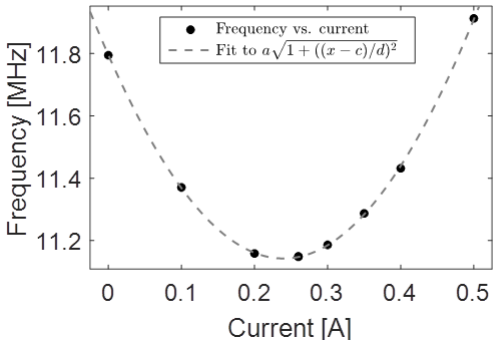

Figure 28: Magnetic field plane calibration, frequency vs current through coil 3 and fit.

From the fit's minimum point we found the current in coil 3 that will produce a magnetic field in the plane of coils 1 and 2. After this measurement, we were able to change the magnetic field varying only the current through coil 2, and calibrate the change of β. This calibration process is shown in Fig. 29.

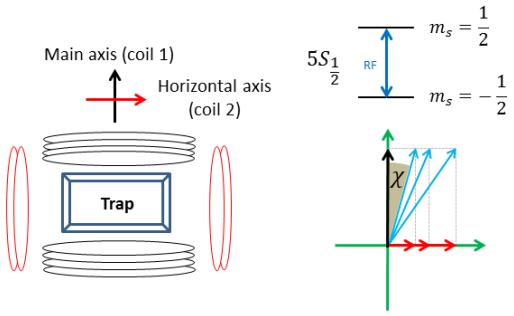

Figure 29: Scanning magnetic field angle.
Left: Directions of coils 1 and 2 with respect to each other and the trap. **Right: (top)** $5S_{\frac{1}{2}}$ Zeeman manifold for probing the magnetic field magnitude in the ion position. **(bottom)** By keeping the magnetic field component corresponding to coil 1 (black arrow) fixed, varying the current in coil 2 leads to perpendicular magnetic field component (red arrow). By measuring the resulting magnetic field magnitude at the ion position (length of blue arrows) the angle β can be calculated, with respect to the minimal magnetic field.

The result of this calibration are shown in Fig. 30. Note that the measured angle is not necessarily β. The measured angle is the angle between the magnetic field and the direction normal to coil 1. However, β is the angle between the magnetic field and the trap axis. Therefore, there is an unknown offset angle, χ_0, yet to be found.

7.4.5 Quadrupole Ramsey experiment

In order to measure quadrupole shifts we followed these steps:

1. We began by preparing the superposition

$$|\psi_{init}\rangle = \frac{1}{\sqrt{2}}\left(\left|J,-\frac{1}{2}\right\rangle + \left|J,-\frac{5}{2}\right\rangle\right). \tag{25}$$

   The ion was first optically pumped to the $\left|S,-\frac{1}{2}\right\rangle$ in the ground state manifold. Then , a 674 nm laser $\frac{\pi}{2}$ pulse drove the ion state to an equal superposition $\frac{1}{\sqrt{2}}\left(\left|S,-\frac{1}{2}\right\rangle + \left|J,-\frac{5}{2}\right\rangle\right)$ was followed by a 674 nm laser π pulse between the states $\left|S,-\frac{1}{2}\right\rangle$ and $\left|J,-\frac{1}{2}\right\rangle$. The result of these operations was the state in Eq. 25. The choice of $m_1 = -\frac{1}{2}$ and $m_2 = -\frac{5}{2}$ for the parameters in section 7.3.3 gives the largest quadrupole shift signal proportional to $\left|m_1^2 - m_2^2\right|$.

2. Next, we performed the RF DD sequence from section 7.3.2, with inter-pulse time 2τ. Depending on the total interrogation time, the sequence was performed once or twice. According to section 7.3.3, the resulting

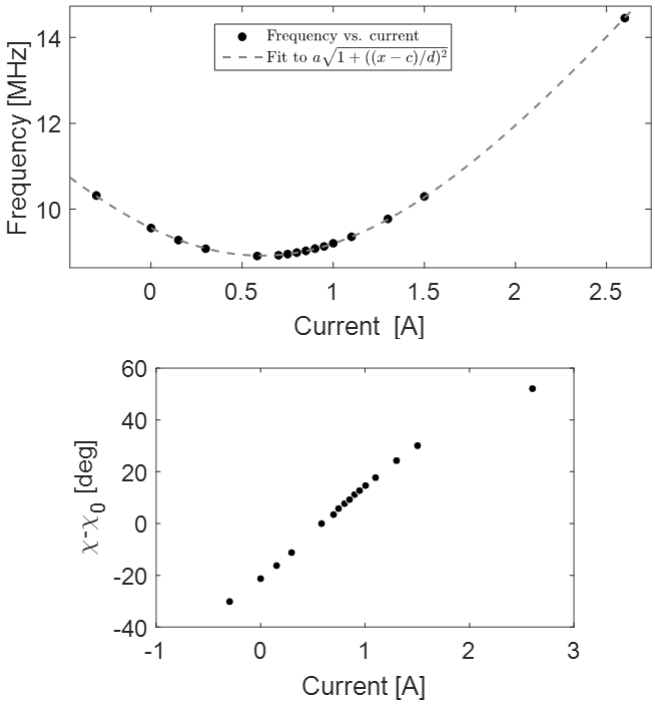

Figure 30: Current-angle conversion.
Left: Frequency vs. current in coil 2 results and fit to theory. **Right:** Resultant current to angle conversion.

state was

$$|\psi(T)\rangle = \frac{1}{\sqrt{2}}\left(\left|J,-\frac{1}{2}\right\rangle + \exp\left[-i\left(12Qn\tau\left(\left(\frac{5}{2}\right)^2-\left(\frac{1}{2}\right)^2\right)\right)\right]\left|J,-\frac{5}{2}\right\rangle\right) =$$

$$= \frac{1}{\sqrt{2}}\left(\left|J,-\frac{1}{2}\right\rangle + \exp\left[-i\left(3\cdot 6QT\right)\right]\left|J,-\frac{5}{2}\right\rangle\right),$$

where we define $T \equiv 4n\tau$ the total interrogation time.

3. After the Ramsey time, we performed a second Ramsey $\frac{\pi}{2}$ pulse. A 674 nm laser π pulse drove the $\left|J,-\frac{5}{2}\right\rangle \leftrightarrow \left|S,-\frac{1}{2}\right\rangle$ transition, leaving the ions in the state $\frac{1}{\sqrt{2}}\left(\left|J,-\frac{1}{2}\right\rangle + \exp\left[-i\left(3\cdot 6QT\right)\right]\left|S,-\frac{1}{2}\right\rangle\right)$. This π pulse was done with opposite phase with respect to the first π pulse on the $\left|J,-\frac{5}{2}\right\rangle \leftrightarrow \left|S,-\frac{1}{2}\right\rangle$ transition, done in the first Ramsey $\frac{\pi}{2}$ pulse above. That was in order to avoid additional laser phase in the superposition. The second Ramsey pulse was then performed on the transition $\left|J,-\frac{1}{2}\right\rangle \leftrightarrow \left|S,-\frac{1}{2}\right\rangle$, with phase χ,such that the resulting state was the detection state

(neglecting any global phase)

$$|\psi_{det}\rangle = \cos\left(\frac{3\cdot 6QT-\chi}{2}\right)\left|J,-\frac{1}{2}\right\rangle + \sin\left(\frac{3\cdot 6QT-\chi}{2}\right)\left|S,-\frac{1}{2}\right\rangle.$$

4. Finally, the state of the ion was measured using fluorescence-selective detection, differentiating between the $|S,m_S\rangle$ manifold and the $|J,m_J\rangle$ manifold. The probability to measure the ion in the $\left|J,-\frac{1}{2}\right\rangle$ state is given by

$$\mathrm{P}\left(\left|J,-\frac{1}{2}\right\rangle\right) = \frac{1}{2}+\frac{1}{2}\cos\left(\left(3\cdot 6QT-\chi\right)\right). \tag{26}$$

Steps 1-4 were averaged over 300 experimental realizations for each of different χ and T values. Fig. 31 show the quadrupole shifts measured results for different times and electric field gradient values.

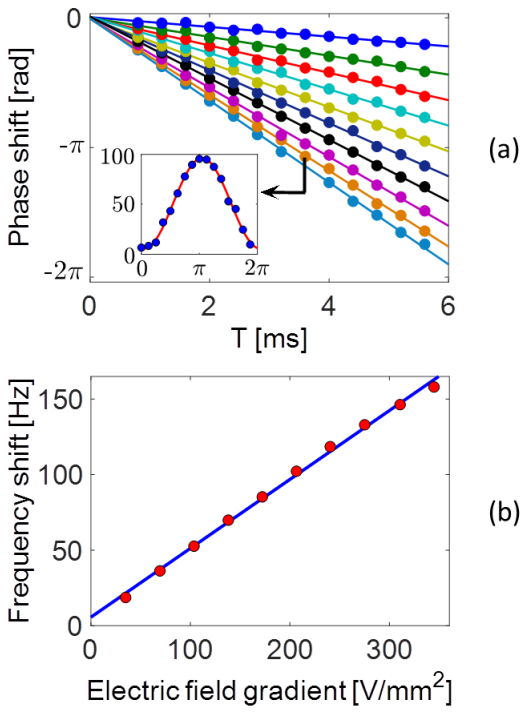

Figure 31: Quadrupole shift measurement.
(a) Ramsey phase as a function of Ramsey time. Full circles are Ramsey phase measurement, extracted from a maximum likelihood fit to a Ramsey fringe obtained by scanning χ, the second Ramsey pulse phase. The inset shows such a fringe, where the horizontal axis is the phase χ and the vertical axis is $\mathrm{P}\left(\left|J,-\frac{1}{2}\right\rangle\right)$ in percent. Each color corresponds to a different electric field gradient. For each electric field gradient value a linear curve was fit to the data, such that the slope corresponds to the frequency difference between $\left|J,\pm\frac{1}{2}\right\rangle$ and $\left|J,\pm\frac{5}{2}\right\rangle$. Since we were interested in the frequency, the interception of each linear fit was subtracted from the data. A non-zero interception point accounts for experimental imperfections since extrapolation to zero electric field gradient should yield vanishing quadrupole shift according to Eq. 20. **(b)** Quadrupole shift frequency as a function of electric field gradient. Each point correspond to the slope obtained from a linear fit in (a).

7.4.6 $4D_{\frac{5}{2}}$ level quadrupole moment measurement

Finally, we used the ability to measure independently the parameters $\frac{dE_a}{da}$, β, and the scheme described above to measure the quadrupole frequency Q in order to measure the quadrupole moment $\Theta\left(D,\frac{5}{2}\right)$. For that aim, we measured the quadrupole shift $Q\left(\frac{dE_a}{da},\beta\right)$ for ten $\frac{dE_a}{da}$ values and sixteen β values. We then

extracted the quadrupole moment $\Theta\left(D, \frac{5}{2}\right)$ using a maximum likelihood fit to the model

$$f\left(\frac{dE_a}{da}, \beta\right) = A\frac{dE_a}{da}\left(3\cos^2\left(\beta - B\right) - 1 + C\sin^2\left(\beta\right)\right), \tag{27}$$

in accordance to Eq. 20, where A, B and C are fitting parameters. Here C parametrizes the asymmetry in the radial trapping frequencies. The entire data set along with the corresponding maximum likelihood fit is shown in Fig. 32.

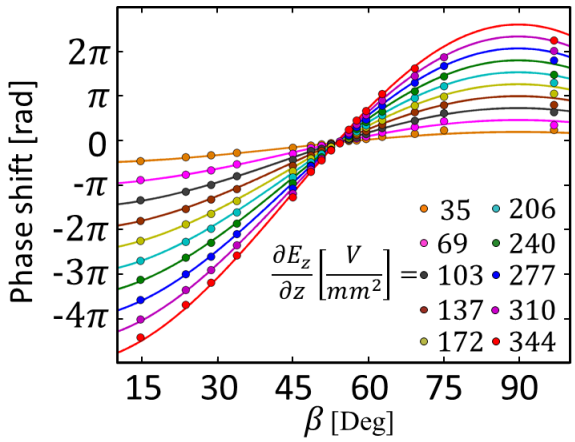

Figure 32: Final data set for quadrupole moment measurement. The plot shows 159 data points, for 16 different β values and 10 different $\frac{dE_a}{dz}$ values. From this fit the value of $\Theta\left(D, \frac{5}{2}\right)$ is extracted.

The final value of the quadrupole moment is $2.973^{+0.026}_{-0.033}\, ea_0^2$ where e is the electron charge and a_0 is the Bohr radius. Here we quote the statistical uncertainty of our measurement. In addition to statistical uncertainty, our measurement may be affected by systematic effects. These include second order Zeeman splitting and perhaps magnetic fields that oscillate synchronously with our dynamical decoupling sequence. The second order Zeeman is evaluated to be 0.5 Hz for our quantization field, and is below our measurement accuracy. We did not synchronize our experiment to any external trigger, and therefore we claim that synchronous magnetic field effects are negligible. The obtained value for the quadrupole moment agrees with theoretical calculations, and is $1.2\,\sigma$ from the only previous measurement. A summary of values from previous works appears in table 1.

Experiment	This work: $2.973^{+0.026}_{-0.033}$		Previous measurement: 2.6 ± 0.3[38]
Theory	3.048[39]	2.94 ± 0.07[40]	2.935 ± 0.017[41]

Table 1: Comparison between our result and previous work.

8 New methods for testing local Lorentz invariance violation with atomic systems

Published article can be found in [42]. This work was done in collaboration with M. S. Safronova and S. G Porsev from the University Of Delawere, V. A Dzuba and V. V Flambaum from the University of New South Wales and with H. Häffner from the University of California.

8.1 Abstract

We present a broadly applicable experimental proposal to search for the violation of local Lorentz invariance (LLI) with atomic systems. This scheme uses DD sequence similar to the one described in section 7.3.2 and can be implemented in current atomic clocks experiments, both with single ions and arrays of neutral atoms. Unlike the experiment measuring the quadrupole shift, the proposed scheme uses RF for both the DD sequence and the initial and final $\frac{\pi}{2}$ Ramsey pulses. This allows the scheme to be performed on systems with no optical transitions, and therefore it is also applicable to highly charged ions which exhibit particularly high sensitivity to Lorentz invariance violation. Here we show the results of an experiment measuring the expected signal of this proposal using a two-ion crystal of $^{88}Sr^{+}$ ions.

8.2 Lorentz invariance violation term in atomic bound electronic states

Local Lorentz Invariance (LLI) is a fundamental postulate of physics, underlying current physical laws. It states that the results of any local non-gravitational experiment are independent of the velocity and the orientation of the free falling apparatus [17]. Experiments testing LLI are usually analyzed in the context of an effective theory called the Standard Model Extension (SME) [43]. According to this effective theory, a transition frequency of a bound electron in an atom can be used for local Lorentz invariance tests. These are the so-called "clock comparison tests" [44, 45]. According to the SME, additional terms are added to the bound electron Hamiltonian [46], where the one that effects the electron energy to first order has the form:

$$\delta\tilde{\boldsymbol{H}} = \tilde{C}_{ij}\boldsymbol{p}_i\boldsymbol{p}_j.$$

Here $\boldsymbol{p}_i$ is the electron momentum operator in the $i = x, y, z$ direction, and $\tilde{C}_{ij}$ are frame dependent coefficients, i.e. their value changes with orientation with respect to some fixed frame of reference. According to section 6.2, Assuming that $\tilde{C}_{ij}$ are small, in order to find the energy shift of an electronic level with J

total angular momentum, we can translate this additional term to the addition of the operator

$$\delta \boldsymbol{H} = \hbar\lambda \left(\boldsymbol{J}^2 - 3\boldsymbol{J}_z^2\right), \tag{28}$$

where λ is an orientation-dependent angular frequency.

8.3 Proposal for LLI test with atomic systems

8.3.1 Earth rotation as a resource

Our system consists of an electron bound in an atom. The electron is in an atomic eigenstate having total angular momentum J. A constant magnetic field determines the orientation of this electronic wave-function in space. As time passes, the earth rotates around itself and the direction of the magnetic field rotates accordingly. Therefore, orientation dependent coefficients in the atomic Hamiltonian will exhibit a modulation at the sidereal frequency [46]. λ in Eq. 28 is one such coefficient, and we conclude that repeated interrogation of these coefficients can lead to measuring LLI violation effects, and if these effects are not detected, then the measurement uncertainty can bound the magnitude of such effects.

8.3.2 System Hamiltonian

The Hamiltonian of the spin J system is given by

$$H = \gamma B_z \boldsymbol{J}_z + \hbar\left(Q+\lambda\right)\left(\overrightarrow{\boldsymbol{J}}^2 - 3\boldsymbol{J}_z^2\right) + 2\hbar\Omega^J\left(t\right)\cos\left(\omega_{RF}t - \phi\right)\boldsymbol{J}_x,$$

similar to the one from section 7.3.1, except for the addition of the λ amplitude. Similar to the quadrupole shift measurement, $\omega_{RF} \approx \frac{\gamma B_z}{\hbar}$, and therefore the rotating frame Hamiltonian (taking the RWA) is given by

$$H_{int} = \hbar\delta\boldsymbol{J}_z + \hbar\left(Q+\lambda\right)\left(\overrightarrow{\boldsymbol{J}}^2 - 3\boldsymbol{J}_z^2\right) + \hbar\Omega^J\left(t\right)\left(\cos\left(\phi\right)\boldsymbol{J}_x + \sin\left(\phi\right)\boldsymbol{J}_y\right). \tag{29}$$

Same as in section 7.3.1, we assume that $\Omega^J\left(t\right)$ is allowed to have the values 0 and $\Omega_0 \gg \delta, Q, \lambda$, leading to the corresponding pulse and free operational modes. From here on, we will use the notation $\kappa = Q + \lambda$.

8.3.3 Pulse sequence

In order to measure a change in λ, we propose a DD sequence that uses the sequence building block described in section 7.3.2. However, unlike the experimental sequence that was used for measuring the quadrupole shift in section 7.3.3, here we initialize the spin state in an eigenstate of $\boldsymbol{J}_z$ with eigenvalue $m_J = m$:

$$\left|\psi_{init}\right\rangle = \left|J, m\right\rangle. \tag{30}$$

Next, application of the operator $\exp\left[i\frac{\pi}{2}\boldsymbol{J}_x\right]$ is carried out by an RF pulse. This operation drives the state $\left|J,m\right\rangle$ to the state $\exp\left[i\frac{\pi}{2}\boldsymbol{J}_x\right]\left|J,m\right\rangle$, which is

an eigenstate of the operator $\boldsymbol{J}_y$ with $\hbar m$ eigenvalue. This eigenstate is a superposition of all $\boldsymbol{J}_z$ eigenstates. As an example, for $J = \frac{5}{2}$ and $m = -\frac{3}{2}$, we get

$$\exp\left[i\frac{\pi}{2}\boldsymbol{J}_x\right]\left|J,-\frac{3}{2}\right\rangle =$$

$$= \frac{1}{4}\left[i\sqrt{\frac{5}{2}}\left|J,-\frac{5}{2}\right\rangle - \frac{3}{\sqrt{2}}\left|J,-\frac{3}{2}\right\rangle - i\left|J,-\frac{1}{2}\right\rangle - \left|J,\frac{1}{2}\right\rangle - \frac{3i}{\sqrt{2}}\left|J,\frac{3}{2}\right\rangle + \sqrt{\frac{5}{2}}\left|J,\frac{5}{2}\right\rangle\right].$$

This comprises the first $\frac{\pi}{2}$ Ramsey pulse of the interrogation.

After this first Ramsey pulse, a sequence of pulses $\exp(\pm i\pi\boldsymbol{J}_y)$ is operated. The change from $\boldsymbol{J}_x$ to $\boldsymbol{J}_y$ is achieved by fast switching of the RF drive phase in a phase-coherent fashion. The reason for this change is to follow CPMG pulse protocol [47], which makes the decoupling from the magnetic field noise more resilient against rotation angle error. The π pulses sequence is similar to the sequence in Fig. 24, with the $\boldsymbol{J}_x \to \boldsymbol{J}_y$ modification. As a result, this sequence can be summarized in the operator $\exp\left[i\left(4\kappa\tau\left(\overrightarrow{\boldsymbol{J}}^2 - 3\boldsymbol{J}_z^2\right)\right)\right]^n$ where $2n$ is the pulse number and τ is half the inter-pulse time. Taking $T = 4n\tau$ the total interrogation time, we get the DD sequence operator

$$U_{\mathrm{DD}} = \exp\left[i\left(\kappa T\left(\overrightarrow{\boldsymbol{J}}^2 - 3\boldsymbol{J}_z^2\right)\right)\right]. \tag{31}$$

The Ramsey sequence ends with a second $\frac{\pi}{2}$ pulse, with χ phase with respect to the first one. The operator applied here is $\exp\left[i\frac{\pi}{2}\left(\boldsymbol{J}_x\cos(\chi) + \boldsymbol{J}_y\sin(\chi)\right)\right]$. In an ideal scenario, χ should be π. However, it is possible to correct for constant residual magnetic field phase due to e.g. imbalance in echo arms with a different value of χ. Finally, the population in the initial state $|J,m\rangle$ is detected by a 674 nm π pulse to the S manifold followed by detection pulse, and provides the signal from our measurement. The entire sequence operator with $\chi = \pi$ has the compact form of

$$U_{\mathrm{Full}} = \exp\left[-i\frac{\pi}{2}\boldsymbol{J}_x\right]\exp\left[i\left(\kappa T\left(\overrightarrow{\boldsymbol{J}}^2 - 3\boldsymbol{J}_z^2\right)\right)\right]\exp\left[i\frac{\pi}{2}\boldsymbol{J}_x\right] =$$

$$= \exp\left[i\left(\kappa T\left(\overrightarrow{\boldsymbol{J}}^2 - 3\boldsymbol{J}_y^2\right)\right)\right], \tag{32}$$

where we used the fact that $\exp\left[-i\frac{\pi}{2}\boldsymbol{J}_x\right]\boldsymbol{J}_z\exp\left[i\frac{\pi}{2}\boldsymbol{J}_x\right] = -\boldsymbol{J}_y$ and the expected measurement signal is then given by this operator expectation value:

$$P_{J,m}[\kappa T, \chi = \pi] = \left|\langle J,m|\exp\left[i\left(\kappa T\left(\overrightarrow{\boldsymbol{J}}^2 - 3\boldsymbol{J}_y^2\right)\right)\right]|J,m\rangle\right|^2 =$$

$$= \left|\langle J,m|\exp\left[-3i\kappa T\boldsymbol{J}_y^2\right]|J,m\rangle\right|^2. \tag{33}$$

In this work, one candidate identified to have relatively large λ is Yb^+ in an $F_{\frac{7}{2}}$ state. Therefore, we computed the signal $P_{J,m}[\kappa T, \chi]$ for different $J{=}\frac{7}{2}$ and different m values. The results are shown in Fig. 33.

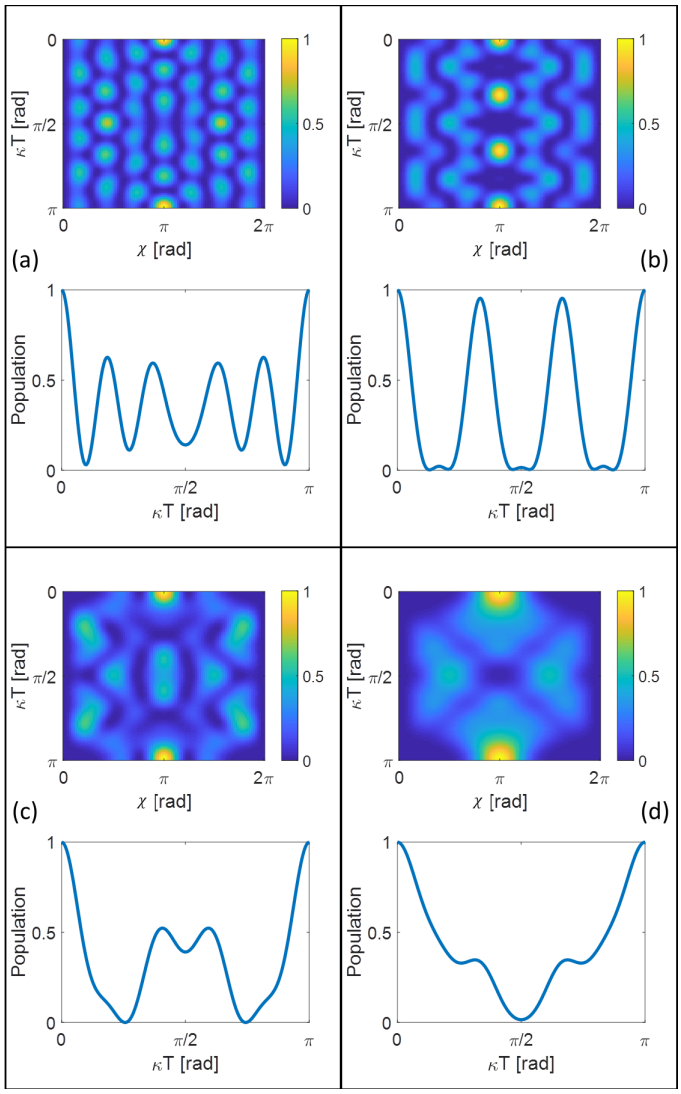

Figure 33: Theoretical calculation of $P_{\frac{7}{2},m}[\kappa T, \chi]$ **(a,b,c,d) Top:** Theoretical calculations of $P_{\frac{7}{2},m}[\kappa T, \chi]$ for $m = \pm\frac{1}{2}, \pm\frac{3}{2}, \pm\frac{5}{2}, \pm\frac{7}{2}$ respectively. **Bottom:** Corresponding Ramsey fringe for $\chi = \pi$ and $\kappa T \in [0, \pi]$.

The figure shows that the $\left|m = \frac{1}{2}\right\rangle$ exhibits the steepest slope in the Ramsey fringe, and therefore this state will have the optimal sensitivity to κ. In order to work around this optimal point, the quadrupole shift Q together with the total interrogation time T can be tuned using magnetic field angle or electric field gradient amplitude (see Eq. 20 in section 7.2.3).

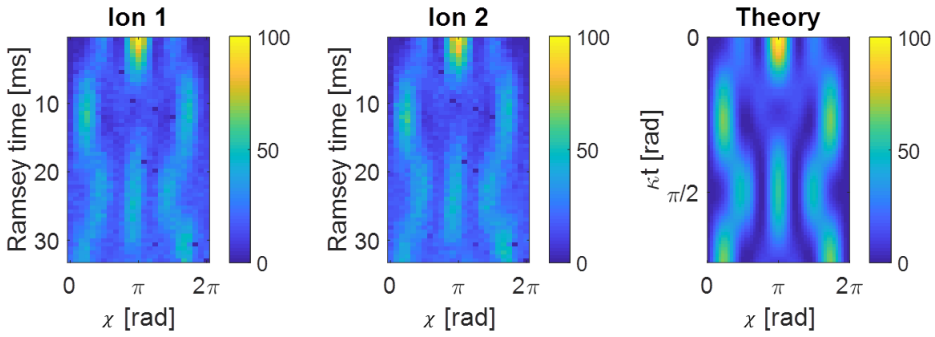

Figure 34: Experimental verification of our theoretical model compared to the calculated model.

Left, middle: Experimental results of the sequence in section 8.3.3 on a two-ion chain. Both the Ramsey time T and the final pulse phase χ are scanned. Here, the main contribution to κ is due to the quadrupole shift Q. **Right:** Theoretical expected results for $4D_{\frac{5}{2}}$ level of $^{88}Sr^{+}$with $m = -\frac{3}{2}$. The results show good visual agreement with the expected results. The contrast is lower, mainly due to residual magnetic field noise and spontaneous decay.

8.3.4 Experimental verification of the theoretical model and the experimental sequence

In order to verify our understanding of the sequence and the theoretical model, we performed a proof-of-principle experiment, in which we observed the signal $P_{\frac{5}{2},-\frac{3}{2}}[\kappa T, \chi]$ of the $4D_{\frac{5}{2}}$ Zeeman manifold of $^{88}Sr^{+}$. The results and the corresponding theoretical calculations are shown in Fig. 34. Here, we scanned both the experiment time and χ, the final Ramsey pulse phase. The effect measured here is dominantly the $^{88}Sr^{+}$ $4D_{\frac{5}{2}}$ level quadrupole shift, due to the poor sensitivity of our ion to LLI violation effects. From this experiment we conclude that our theory is valid, and that this experimental procedure could be performed with more than a single ion.

8.3.5 Calibration of pulse frequency and time

In order to perform the experimental sequence described in section 8.3.3, we need to know Ω_0 and the RF resonance frequency $\frac{\gamma B_z}{\hbar}$. Moreover, in order to maintain the applicability of our sequence to various different atomic systems, we would like to perform measurements of these quantities which are limited to the same tools used in the sequence itself. We show that this can be done by a calculated model for large spin Rabi oscillations and Rabi spectroscopy. The results of such measurements for $4D_{\frac{5}{2}}$ level of $^{88}Sr^{+}$ with $m = -\frac{3}{2}$ are shown in Fig. 35. In both the Rabi spectroscopy and the Rabi oscillations experiments, the ion was initialized in the $\left|J, -\frac{3}{2}\right\rangle$ state. In the Rabi spectroscopy, after initialization, a RF pulse with duration of $\tau \approx \frac{\pi}{\Omega_0}$ is applied, with angular

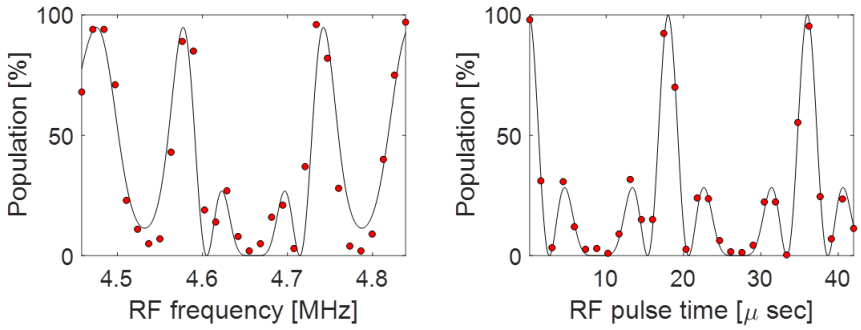

Figure 35: Measurement of Ω_0 and ω_{RF}.
Left: Rabi spectroscopy on spin $J = \frac{5}{2}$. Right: Rabi oscillations on spin $J = \frac{5}{2}$. In both cases the ion's state was initialized to $\left|m = -\frac{3}{2}\right\rangle$ state in the $4D_{\frac{5}{2}}$ manifold. Red full circles are measurements results and black solid line is theoretical fit. The RF frequency was measures to be $\omega_{RF} = 2\pi \times 4.65$ MHz, and the RF Rabi frequency was measured to be $\Omega_0 = 2\pi \times 55$ kHz.

frequency ω_{RF}. After the pulse, the population of the initial state $\left|J, -\frac{3}{2}\right\rangle$ is detected. The experiment is repeated for different values of ω_{RF}, and fitted to theory, from which the resonance frequency $\omega_{RF} = \frac{\gamma B_z}{\hbar}$ is extracted. In the Rabi oscillations experiment, after initialization, a resonant RF drive at frequency $\omega_{RF} = \frac{\gamma B_z}{\hbar}$ is applied for varying duration time τ. At the end of the pulse the initial state $\left|J, -\frac{3}{2}\right\rangle$ population is detected. Again, the correct Ω_0 is extracted from the fit to the theoretical model. The theoretical model is calculated as

$$P(m) = \left|\langle J, m| \exp\left[i\left(\Omega \boldsymbol{J}_x + \delta \boldsymbol{J}_z\right)\tau\right]|J, m\rangle\right|^2. \tag{34}$$

For the Rabi spectroscopy, we choose $\Omega = \Omega_0$ and we scan δ, and for the Rabi oscillation we choose $\delta = 0$ and we scan Ω.

8.3.6 LLI violation term sensitivity

We calculate the sensitivity of our method. We assume no systematic drifts, and under this assumption our measurement results can be described as a random variable $Y = \frac{1}{n}\sum_{i=1}^{n} x_i$, where x_i represents the number of ions detected in the $|J, m\rangle$ state after the i'th experimental realization, where n is the number of realizations. Each x_i is therefore a number between 0 and N an experiment performed with N ions. We denote the change in λ that can be observed between different measurements as $\Delta\lambda$, and it is given by

$$\Delta\lambda = \left(\frac{dE[Y]}{d\lambda}\right)^{-1} \sqrt{V[E[Y]]},$$

where $E[Y]$ is the expectation value of Y and $V[E[Y]]$ is the variance $E[Y]$. Here, we assume that $V\left[\sum_{i=1}^{n} x_i\right] \gg 1$, and therefore we can use $\sqrt{V[E[Y]]}$ as

projection noise uncertainty. In the experiment described above, the detected signal is a function of κT (see Eq. 33). We denote this function here as $F(\kappa T)$, and it is the $x_i's$ binomial parameter. Therefore, we can write that

$$\sqrt{V[E[Y]]} = \sqrt{\frac{F(\kappa T)(1-F(\kappa T))N}{n}},$$

and

$$E[Y] = NF(\kappa T).$$

We find that

$$\Delta\lambda = \Delta\kappa = \frac{\sqrt{F(\kappa T)(1-F(\kappa T))}}{\sqrt{Nn}\frac{d}{d\kappa}F(\kappa T)}.$$

Next, we denote $\kappa T = \xi$ and we write

$$\Delta\lambda = \frac{\sqrt{F(\xi)(1-F(\xi))}}{\sqrt{Nn}T\frac{d}{d\xi}F(\xi)}.$$

Assuming that the total experiment time is dominated by the Ramsey interrogation time (no "dead time") then we can denote $\tau = nT$ the total integration time, and we write

$$\Delta\lambda = \frac{\sqrt{F(\xi)(1-F(\xi))}}{\sqrt{N\tau T}\frac{d}{d\xi}F(\xi)}.$$

In our proposal for Yb^+ we use $F(\xi) = P_{\frac{7}{2},m}(\xi,\pi)$. The calculated values for the different m_J states are:

$$m_J = \frac{1}{2} \to \xi_{\frac{1}{2}} \approx 0.15 \text{ rad}, \ \Delta\lambda = 0.10\frac{\text{rad}}{\sqrt{N\tau T}},$$

$$m_J = \frac{3}{2} \to \xi_{\frac{3}{2}} \approx 0.17 \text{ rad}, \ \Delta\lambda = 0.11\frac{\text{rad}}{\sqrt{N\tau T}},$$

$$m_J = \frac{5}{2} \to \xi_{\frac{5}{2}} \approx 0.20 \text{ rad}, \ \Delta\lambda = 0.17\frac{\text{rad}}{\sqrt{N\tau T}},$$

$$m_J = \frac{7}{2} \to \xi_{\frac{7}{2}} \approx 0.22 \text{ rad}, \ \Delta\lambda = 0.28\frac{\text{rad}}{\sqrt{N\tau T}}.$$

Here ξ_{m_J} was chosen to maximize $\left|\frac{d}{d\xi}F(\xi)\right|$, in order to reduce sensitivity to additional experimental noise that might reduce the contrast of $F(\xi)$.

8.3.7 Comparison to previous proposals and bounds

In [48] a different method for measuring λ was proposed, relying on a DFS between two ions. In this proposal, a superposition of two ions is formed that is insensitive to linear Zeeman splitting drifts common to both ions, but is susceptible $\boldsymbol{J}_z^2$ type operators. We would like to compare the sensitivity of our proposed

sequence to this previous proposed method. Using the notation described above and since in [48] the ions are prepared in the two-ions superposition:

$$\frac{1}{\sqrt{2}}\left(\left|J,m_1=\frac{7}{2}\right\rangle\left|J,m_2=-\frac{7}{2}\right\rangle^{\otimes\frac{N}{2}}+\left|J,m_1=\frac{1}{2}\right\rangle\left|J,m_2=-\frac{1}{2}\right\rangle^{\otimes\frac{N}{2}}\right),$$

we get the Ramsey fringe form of

$$F\left(\xi\right)=\frac{1}{2}\left(1+\sin\left[N\left(\left(\frac{7}{2}\right)^2-\left(\frac{1}{2}\right)^2\right)\xi\right]\right).$$

Note that here, each experimental realization result has only two options, and therefore $E\left[Y\right]=F\left(\xi\right)$. Assuming full Ramsey contrast, we get

$$\Delta\lambda=0.083\frac{\text{rad}}{N\sqrt{\tau T}}.$$

Although this result scales better with the number of spins, it is much more difficult to scale experimentally beyond two ions.

The best bound in the electron sector to date is set by the experiment in [49]. Here, the bound is inferred from a comparison between two single $^{171}\text{Yb}^{+}$ clocks, where the quantization axes of the two clocks were perpendicular. This bound is in the 10^{-21} scale. Taking our example of Yb^{+} with no nuclear spin, we obtain:

$$\kappa_{\text{Yb}^{+}}=2\pi\times5.1\times10^{15}\times C_0^{(2)}\rightarrow$$

$$\rightarrow\Delta C_0^{(2)}=\frac{\Delta\kappa}{2\pi\times5.1\times10^{15}}=3.12\times10^{-18}\frac{1}{\sqrt{N\tau T}}.$$

This implies that 10 days of averaging (864000 seconds), with Ramsey interrogation time of $T=1$ seconds and modest atom number of $N=10$ already yields a bound of $\Delta C_0^{(2)}\leq1.1\times10^{-21}$, better than the best bound to date.

8.3.8 Compatible systems and method advantages

The experimental method described above for measuring LLI violation effects can be applied in different atomic systems:

First, The sequence applies independently on each one of the atoms, i.e. requires only local operations. Therefore, it does not require entanglement and correlation between different atoms. Due to this fact, it can be implemented even with a single ion in a trapped Yb^{+}experiment, a system that already exists and running. In addition, the fact that no correlations are needed and yet magnetic field drifts can be avoided, leads to the potential use of large atomic ensembles, such as in lattice clocks, for this LLI violation test.

Second, since the entire interrogation of the ion is done using RF, even ions that do not exhibit strong or any usable optical transitions can be candidates for this test. This can be done by means of logic spectroscopy [50], where the

internal state of the ion can be read by a second ion via their mutual motion. This does not require an optical transition, and can be done by a magnetic field gradient [51, 52]. The relaxed requirement for optical transitions opens this proposal to the world of highly charged ions (HCI), that can exhibit high sensitivity to LLI violation effects.

We also note that since the interrogation operations are done with RF that exhibits long wavelength, they have reduced sensitivity to heating of the trapped atoms. Therefore, even if both in initialization and detection optical transitions might be needed, optical pumping and repeated detection can increase the fidelity of these operation against heating.

9 Quadrupole shift cancellation using RF continuous dynamical decoupling

9.1 Abstract

In this work we present a method that uses RF magnetic field pulses in order to cancel the quadrupole shift in trapped ions clock transition. Due to the fact that quadrupole shifts in a single ion are affected by charges in its vicinity it is inherently an inhomogeneous broadening mechanism in trapped ion chains, limiting current optical ion clocks to low signal to noise ratio of a single probe ion. Canceling this shift at each interrogation of the clock transition frequency allows the use of $N > 1$ ions in these clocks, thus reduces the statistical uncertainty in the clock frequency by $\sqrt{N}$ according to the standard quantum limit. Our sequence relies on the tensorial nature of the quadrupole shift, and thus also cancels other tensorial shifts, such as the tensor ac stark shift. We demonstrate our sequence experimentally on three and more $^{88}Sr^{+}$ ions trapped in a linear Paul trap, using correlation spectroscopy. We show reduction of quadrupole shift difference between ions to < 20 mHz's level, where other shifts such as relativistic Doppler shift limit our spectral resolution. In addition, we show that using radio-frequency dynamic decoupling we can also cancel differences in the magnetic field between different ions.

9.2 Single ion vs multi-ion frequency reference

9.2.1 Signal to noise ratio in optical atomic clock operation

Trapped atomic-ions are excellent frequency references. Many of them exhibit narrow optical transitions, they can be localized and controlled to very good degree, they can be cooled to their ground state and more. Due to these favorable characteristics, some of the best clocks today are based on a single trapped atomic ion. The ion is usually reduced to an approximated two-level system, where the optical frequency reference is the frequency difference between these two levels and all the other levels are to be avoided (e.g. with repumping) or used for operations other than frequency interrogation (e.g. initialization and

detection). These systems are extensively studied, and their systematic and statistical shifts are known. The interrogation process of the ion is always done by

1. initialization of the ions to a known (usually ground) state (typically using dissipative process like optical pumping) that is one of the two levels in its clock transition.

2. Interrogation of the ion's clock transition and a local oscillator frequency difference by a spectroscopy scheme (e.g. Rabi or Ramsey).

3. Projection of the final ion's state on one of the two levels by detecting which state the ion ends up in.

The use of projective measurement in step 3 limits the SNR. Both in Ramsey and Rabi spectroscopy the optimal working point to measure is when the probability to detect each of the two levels at the end of the interrogation is equal. The SNR can be calculated as $\frac{\mu}{\sigma}$, where μ is the measurement expectation value and σ is it's standard deviation. Here, assuming projection noise, the measurement can be described as a Bernoulli random variable Y with parameter $p = 0.5$. Therefore, the SNR of a single frequency interrogation is $\text{SNR} = \frac{1\times 0.5}{\sqrt{1\times 0.5(1-0.5)}} = 1$. In order to extract information about the frequency difference between the transition frequency and the local oscillator, the measurement must be repeated and averaged over time to increase the SNR. However, that lets in dynamical noise sources, decreasing the clock stability. Another approach for increasing the SNR is to use multiple frequency references simultaneously at each interrogation. Then, if they are identical, the measurement is described by a random variable $Z = \frac{1}{N}\sum Y_i$ that is, Z is the mean of $N > 1$ identically independent Bernoulli random variables with parameter parameter $p = 0.5$. Here, N is the number of frequency references. The signal to noise is then $\text{SNR} = \frac{0.5}{\sqrt{\frac{1}{N}\times 0.5(1-0.5)}} = \sqrt{N}$. This approach is the drive behind neutral atomic references, such as in lattice clocks [53, 15, 54, 55], where $N = 10^3$ to 10^5 atoms. However, these systems encounter other systematic shifts, that limit the performance of the clock, and make it difficult to reach the ideal stability originating in the projection noise analysis above.

9.2.2 Multiple atomic-ion reference

As was mentioned in section 9.2.1, using more than a single frequency reference can improve the signal to noise. However, the references must be identical, meaning they oscillate at the same frequency. Otherwise, each reference should be addressed differently, and their frequency difference has to be monitored. This will complicate the clock operation since it cannot be addressed with a single optical beam, decrease the SNR compared to the ideal case stated above and might even create ambiguity in the signal averaging. The effect of different frequencies exhibited by different references in the same clock is referred to as inhomogeneous broadening. Due to the fact that all ions of the same kind are

inherently identical, difference between identical-ions transitions can only arise from their different environment. Most of the atomic-ion based clocks use a single ion probe in order to avoid this difficult problem of providing identical environment to ions at different positions. Inhomogeneous broadening mechanisms in trapped atomic ions include magnetic field spatial dependence, ion velocity spatial dependence (leading to difference in second order Doppler between different ions) black-body radiation spatial dependence and more. The dominant mechanism, however, which is (almost) inherent to trapped ions is the quadrupole shift.

9.2.3 Quadrupole shift in a multi-ion chain

The quadrupole shift physical parameters are described in Eq. 20. Even in the case where β, α, J are the same for all ions, it is difficult to produce a uniform gradient in electric field. As an example, in linear Paul trap, unless extensive effort is made to do differently, the trapping potential is to a good approximation harmonic in the trap axis direction. That means that each ion feels the same electric field gradient $\frac{dE_a}{da}$ originating from the trap, and therefore the trap electrodes do not contribute to the inhomogeneity in the quadrupole shift. However, in addition to the potential from the trap electrodes, each ion feels the charges of the other ions in the trap. Assuming k trapped ions in a linear chain, such that the i'th ion is located at the equilibrium position a_i along the trap axis $\hat{a}$. The ions have identical charge q and mass m, and therefore the DC electric potential at the i'th ion position is given by

$$V\left(a_i\right) = \sum_{j \neq i} \frac{q}{4\pi\varepsilon_0 \left|a_i - a_j\right|} + \frac{1}{2q} m\omega_a^2 a_i^2 + \left(\text{terms independent of } a_i\right).$$

where ω_a is the trap axial frequency, m is the ion mass and ε_0 is the vacuum permittivity. Differentiating this expression twice with respect to a_i gives:

$$\frac{dE_a}{da}\left(a_i\right) = 2\frac{q}{4\pi\varepsilon_0} \sum_{j \neq i} \frac{1}{\left|a_i - a_j\right|^3} + \frac{m\omega_a^2}{q}. \tag{35}$$

We show the inhomogeneity through an example of three ions. In a three-ion chain, choosing the center ion position as $a_{\text{center}} = 0$, the positions of the left, center and right ions are $a_{\text{left}} = -l$, $a_{\text{center}} = 0$, $a_{\text{right}} = l$ respectively. Computing the electric field gradient of each of the ions, we get

$$\begin{cases} \frac{dE_a}{da}\left(a_{\text{left}}\right) = \frac{dE_a}{da}\left(a_{\text{right}}\right) = \frac{2q}{4\pi\varepsilon_0 l^3} \times \frac{9}{8} + \frac{m\omega_a^2}{q} \\ \\ \frac{dE_a}{da}\left(a_{\text{center}}\right) = \frac{2q}{4\pi\varepsilon_0 l^3} \times 2 + \frac{m\omega_a^2}{q} \end{cases}. \tag{36}$$

In order to estimate the magnitude of the inhomogeneity in this example, we need to know l. The distances of three trapped ions forming a linear chain in a

harmonic trap are given in [56]. From here we can compute l:

$$l = 1.0772 \times \left(\frac{q^2}{4\pi\varepsilon_0 m\omega_a^2} \right)^{\frac{1}{3}}. \tag{37}$$

Plugging it into Eq. 36, we get

$$\begin{cases} \frac{dE_a}{da}\left(a_{\text{left}}\right) = \frac{dE_a}{da}\left(a_{\text{right}}\right) \approx 2.8 \times \frac{m\omega_a^2}{q} \\ \\ \frac{dE_a}{da}\left(a_{\text{center}}\right) \approx 4.2 \times \frac{m\omega_a^2}{q} \end{cases}, \tag{38}$$

meaning $\frac{dE_a}{da}\left(a_{\text{center}}\right) \approx \frac{3}{2} \times \frac{dE_a}{da}\left(a_{\text{right}}\right)$. From section 7.4.5 we find that for standard trapping parameters, $\frac{m\omega_a^2}{q}$ can vary between 10's and 100's $\frac{V}{mm^2}$ in $^{88}Sr^+$, meaning the inhomogeneity can amount to several Hz or more. For $^{88}Sr^+$, the optical frequency is about 4.4×10^{14} Hz, and therefore 1 Hz leads to a relative frequency shift between different ions of $\frac{\Delta f}{f_0} \sim 2 \times 10^{-15}$.

9.3 Scheme for cancellation of quadrupole shifts using RF pulses

9.3.1 Full Hamiltonian description

An ion-based optical clock employs optical transitions as frequency references. Therefore here, unlike sections 7 and 8, both ground state and excited state in the clock transition should be considered. As in many ion-based clocks, we assume the ground state has no quadrupole moment, and therefore exhibits no quadrupole shift. Our method is constructed for Ramsey-type spectroscopy, in which laser light only addresses the ion in the beginning and end of the sequence. Therefore, for clarity, we will construct Hamiltonian and operators for the Ramsey interrogation time between these two pulses, not accounting for transitions between the ground and excited states. We assume two spin subspaces, spin $J > \frac{1}{2}$ and spin $S = \frac{1}{2}$, such that they act on completely orthogonal spin sub-spaces $\{|J, m_J\rangle\}_{m_J}$ and $\{|S, m_S\rangle\}_{m_S}$ respectively. In Consistency with the above described experiments, we denote the angular momentum operator acting on $S\,(J)$ subspaces with the symbols $\boldsymbol{S}\,(\boldsymbol{J})$, and these operators leave a spin state $|S, m_S\rangle\,(|J, m_J\rangle)$ it its corresponding subspace. Each spin has its own associated magnetic moment denoted by $\overrightarrow{\boldsymbol{\mu}_S} = \gamma_S \overrightarrow{\boldsymbol{S}}$ and $\overrightarrow{\boldsymbol{\mu}_J} = \gamma_J \overrightarrow{\boldsymbol{J}}$. Following the same Hamiltonian construction in section 7.3.1, we obtain the total Hamiltonian

$$H_{\text{total}} = \hbar\omega_{\text{opt}} I_J + B_z\left(\gamma_J \boldsymbol{J}_z + \gamma_S \boldsymbol{S}_z\right) + \hbar Q\left(\overrightarrow{\boldsymbol{J}}^2 - 3\boldsymbol{J}_z^2\right)...$$

$$...+2\hbar\cos\left(\omega_{RF}^J t - \phi_J\right)\left(\Omega_J\left(t\right)\boldsymbol{J}_x + \Omega_S\left(t\right)\boldsymbol{S}_x\right)+2\hbar\cos\left(\omega_{RF}^S t - \phi_S\right)\left(C_J\left(t\right)\boldsymbol{J}_x + C_S\left(t\right)\boldsymbol{S}_x\right) \tag{39}$$

where $I_J = \sum_{m_J} |J, m_J\rangle \langle J, m_J|$, ω_{opt} is the optical transition frequency between the $\{|J, m_J\rangle\}_{m_J}$ and $\{|S, m_S\rangle\}_{m_S}$ manifolds at $B_z = 0$, $\Omega_i(t) = \gamma_i B_x^J(t)$, $C_i(t) = \gamma_i B_x^S(t)$ where B_x^J and B_x^S are the RF magnetic field amplitudes corresponding to fields at frequencies ω_{RF}^J and ω_{RF}^S respectively and i is J or S. Following the same assumptions in previous sections, $\Omega_i(t)$ and $C_i(t)$ can have two values: 0 and Ω_0^i or C_0^i respectively. Since $\hbar\omega_{\text{opt}} I_J$ commutes with all spin operators, in the following we disregard it. We choose ω_{RF}^J and ω_{RF}^S to be close to resonance with the magnetic separation of the spin J and spin S respectively, meaning $\omega_{RF}^J \approx \frac{B_z\gamma_J}{\hbar}$ and $\omega_{RF}^S \approx \frac{B_z\gamma_S}{\hbar}$. Since we do not account for transitions between the S manifold and the J manifold, we can separate the Hamiltonian into two parts:

$$H_J = B_z\gamma_J \boldsymbol{J}_z + \hbar Q\left(\overrightarrow{\boldsymbol{J}}^2 - 3\boldsymbol{J}_z^2\right) + 2\hbar\Omega_J(t)\cos\left(\omega_{RF}^J t - \phi_J\right)\boldsymbol{J}_x + 2\hbar C_J(t)\cos\left(\omega_{RF}^S t - \phi_S\right)\boldsymbol{J}_x,$$

$$H_S = B_z\gamma_S \boldsymbol{S}_z + 2\hbar\Omega_S(t)\cos\left(\omega_{RF}^J t - \phi_J\right)\boldsymbol{S}_x + 2\hbar C_S(t)\cos\left(\omega_{RF}^S t - \phi_S\right)\boldsymbol{S}_x.$$

Note: Due to the fact that the quadrupole shift exists only in the J manifold, in the following we will describe the quadrupole cancellation sequence only in this manifold, meaning using H_J alone. In addition, For this section, we set $C_J(t) = C_S(t) = 0$.

9.3.2 J subspace operations

We analyze the case of $\Omega_J(t) = \Omega_0^J$. We move to the interaction picture with respect to the Hamiltonian $\tilde{H} = \hbar\omega_{RF}^J \boldsymbol{J}_z$:

$$H_J^{int} = e^{-i\frac{\tilde{H}}{\hbar}t} H_J e^{i\frac{\tilde{H}}{\hbar}t} - \tilde{H} =$$

$$= B_z\gamma_J \boldsymbol{J}_z + \hbar Q\left(\overrightarrow{\boldsymbol{J}}^2 - 3\boldsymbol{J}_z^2\right) + 2\hbar\cos\left(\omega_{RF}^J t - \phi\right)\left(\Omega_0^J e^{-i\omega_{RF}^J t\boldsymbol{J}_z}\boldsymbol{J}_x e^{i\omega_{RF}^J t\boldsymbol{J}_z}\right) - \hbar\omega_{RF}^J \boldsymbol{J}_z$$

$$= \hbar\delta_J \boldsymbol{J}_z + \hbar Q\left(\overrightarrow{\boldsymbol{J}}^2 - 3\boldsymbol{J}_z^2\right) + 2\hbar\cos\left(\omega_{RF}^J t - \phi\right)\left[\Omega_0^J\left(\cos\left(\omega_{RF}^J t\right)\boldsymbol{J}_x + \sin\left(\omega_{RF}^J t\right)\boldsymbol{J}_y\right)\right].$$

where we defined $\delta_J = \frac{B_z\gamma_J}{\hbar} - \omega_{RF}^J$. Assuming $\omega_{RF}^J \gg \Omega_0^J \gg Q, \delta_J$, we can take the rotating wave approximation for H_J with respect to the fast rotating ω_{RF} and we obtain

$$H_J^{int} = \hbar\delta_J \boldsymbol{J}_z + \hbar Q\left(\overrightarrow{\boldsymbol{J}}^2 - 3\boldsymbol{J}_z^2\right) + \hbar\Omega_0^J\left(\cos(\phi)\boldsymbol{J}_x + \sin(\phi)\boldsymbol{J}_y\right). \tag{40}$$

Unlike in section 7.3.1, here we define three operation modes:

1. Free mode:
   In this mode, we do not operate the drive, meaning $\Omega_J(t) = 0$. The evolution operator in this case is

$$U_f^J(\tau) = \exp\left[i\left(\delta_J\tau\boldsymbol{J}_z + Q\tau\left(\overrightarrow{\boldsymbol{J}}^2 - 3\boldsymbol{J}_z^2\right)\right)\right]. \tag{41}$$

2. Pulse mode:
   In this mode, the RF drive is operated for a short time τ, such that the evolution due to the Hamiltonian terms $\delta_J \boldsymbol{J}_z + Q\left(\overrightarrow{\boldsymbol{J}}^2 - 3\boldsymbol{J}_z^2\right)$ in H_J is negligible. Therefore, in this mode the evolution takes the form

$$U_p^J(\phi,\tau) = \exp\left[i\left(\Omega_0^J \tau\left(\cos(\phi)\boldsymbol{J}_x + \sin(\phi)\boldsymbol{J}_y\right)\right)\right].$$

3. Continuous mode:
   In this mode, the drive operates for longer time τ, such that the terms $\delta_J \boldsymbol{J}_z + Q\left(\overrightarrow{\boldsymbol{J}}^2 - 3\boldsymbol{J}_z^2\right)$ cannot be neglected. In order to understand the evolution, we split the Hamiltonian H_J^{int} to two parts, $H_J^{int} = H_{diag} + H_{off}$, where

$$H_{diag}(\phi) = \hbar\Omega_0^J\left(\cos(\phi)\boldsymbol{J}_x + \sin(\phi)\boldsymbol{J}_y\right) + \hbar Q\left(\overrightarrow{\boldsymbol{J}}^2 - \frac{3}{2}\left(\boldsymbol{J}_z^2 + \left(\cos(\phi)\boldsymbol{J}_x + \sin(\phi)\boldsymbol{J}_y\right)^2\right)\right), \tag{42}$$

   is diagonal in the $\left\{\overrightarrow{\boldsymbol{J}}^2, \cos(\phi)\boldsymbol{J}_x + \sin(\phi)\boldsymbol{J}_y\right\}$ mutual basis, and

$$H_{off}(\phi) = \hbar\delta_J \boldsymbol{J}_z - \frac{3}{2}\hbar Q\left(\cos(\phi)\boldsymbol{J}_x + \sin(\phi)\boldsymbol{J}_y\right)^2,$$

   has only off diagonal elements in this basis. As a result, H_{off} does not contribute to the energy of an eigenstate from this basis to first order in Q or δ_J, and therefore can be neglected. The continuous mode evolution can be therefore approximated to be according to H_{diag}, and the evolution takes the form of

$$U_c^J(\phi,\tau) = \exp\left[i\frac{\tau}{\hbar}H_{diag}(\phi)\right].$$

9.3.3 Quadrupole shift cancellation pulse sequence

Assuming desired Ramsey time T, the proposed quadrupole shift cancellation sequence evolution $U_{\text{total}}(T)$ is as follows:

$$U_{\text{seq}}^J(T) = U_f^J\left(\frac{T}{3}\right)U_p^J\left(\pi, \frac{\pi}{2\Omega_0^J}\right)U_c^J\left(-\frac{\pi}{2}, \frac{T}{3}\right)U_c^J\left(\frac{\pi}{2}, \frac{T}{3}\right)U_p^J\left(0, \frac{\pi}{2\Omega_0^J}\right). \tag{43}$$

In order to calculate the resulting operation and verify the quadrupole shift cancellation, we write these evolution operators explicitly and use the fact that J operators are generators of rotations:

$$U_{\text{seq}}^J(T) =$$

$$= \exp\left[i\left(\delta_J\frac{T}{3}\boldsymbol{J}_z + Q\frac{T}{3}\left(\overrightarrow{\boldsymbol{J}}^2 - 3\boldsymbol{J}_z^2\right)\right)\right]...$$

$$...\exp\left[-i\frac{\pi}{2}\boldsymbol{J}_x\right]...$$

$$... \exp\left[i\left(Q\frac{T}{3}\left(\overrightarrow{\boldsymbol{J}}^2-\frac{3}{2}\left(\boldsymbol{J}_z^2+\boldsymbol{J}_x^2\right)\right)-\Omega_0^J\frac{T}{3}\boldsymbol{J}_y\right)\right]\exp\left[i\left(Q\frac{T}{3}\left(\overrightarrow{\boldsymbol{J}}^2-\frac{3}{2}\left(\boldsymbol{J}_z^2+\boldsymbol{J}_x^2\right)\right)+\Omega_0^J\frac{T}{3}\boldsymbol{J}_y\right)\right]...$$
$$... \exp\left[i\frac{\pi}{2}\boldsymbol{J}_x\right].$$

First, we note that the arguments of the two exponents in the fourth line commute with each other. Therefore, we can write

$$U_{\text{seq}}^J(T)=$$
$$=\exp\left[i\left(\delta_J\frac{T}{3}\boldsymbol{J}_z+Q\frac{T}{3}\left(\overrightarrow{\boldsymbol{J}}^2-3\boldsymbol{J}_z^2\right)\right)\right]...$$
$$... \exp\left[-i\frac{\pi}{2}\boldsymbol{J}_x\right]...$$
$$... \exp\left[i\left(QT\left(\frac{2}{3}\overrightarrow{\boldsymbol{J}}^2-\left(\boldsymbol{J}_z^2+\boldsymbol{J}_x^2\right)\right)\right)\right]...$$
$$... \exp\left[i\frac{\pi}{2}\boldsymbol{J}_x\right].$$

Next, we use the fact that $\exp\left[-i\frac{\pi}{2}\boldsymbol{J}_x\right]A\exp\left[i\frac{\pi}{2}\boldsymbol{J}_x\right]$ is a rotation of the operator A around the x axis with a rotation angle of $\frac{\pi}{2}$, and therefore $\boldsymbol{J}_z\rightarrow\boldsymbol{J}_y$ and $\boldsymbol{J}_x\rightarrow\boldsymbol{J}_x$. We therefore write

$$U_{\text{seq}}^J(T)=$$
$$=\exp\left[i\left(\delta_J\frac{T}{3}\boldsymbol{J}_z+Q\frac{T}{3}\left(\overrightarrow{\boldsymbol{J}}^2-3\boldsymbol{J}_z^2\right)\right)\right]...$$
$$... \exp\left[i\left(QT\left(\frac{2}{3}\overrightarrow{\boldsymbol{J}}^2-\left(\boldsymbol{J}_y^2+\boldsymbol{J}_x^2\right)\right)\right)\right].$$

Finally, the arguments of the two remaining exponents commute, and therefore we write:

$$U_{\text{seq}}^J(T)=$$
$$=\exp\left[i\left(\delta_J\frac{T}{3}\boldsymbol{J}_z+Q\frac{T}{3}\left(\overrightarrow{\boldsymbol{J}}^2-3\boldsymbol{J}_z^2\right)+QT\left(\frac{2}{3}\overrightarrow{\boldsymbol{J}}^2-\left(\boldsymbol{J}_y^2-\boldsymbol{J}_x^2\right)\right)\right)\right]=$$
$$=\exp\left[i\left(\delta_J\frac{T}{3}\boldsymbol{J}_z+QT\left(\overrightarrow{\boldsymbol{J}}^2-\left(\boldsymbol{J}_z^2+\boldsymbol{J}_y^2-\boldsymbol{J}_x^2\right)\right)\right)\right].$$

By definition, $\overrightarrow{\boldsymbol{J}}^2-\left(\boldsymbol{J}_z^2+\boldsymbol{J}_y^2-\boldsymbol{J}_x^2\right)=\boldsymbol{0}$, and therefore the resulting operator takes the form

$$U_{\text{seq}}^J(T)=\exp\left[i\left(\delta_J\frac{T}{3}\boldsymbol{J}_z\right)\right],$$

and the quadrupole shift is eliminated.

9.3.4 Quadrupole shift and $1^{\mathbf{st}}$ order Zeeman shift cancellation

In the previous section, we showed that applying the sequence in Eq. 43 cancels the quadrupole shift. However, the resulting evolution can still be affected homogeneously by magnetic field drifts and inhomogeneously by magnetic field difference between different ions. Since in an optical clock operation we are interested in the transition frequency between the ground and excited levels, the magnetic field shift phase we should regard is the relative phase between these levels. Therefore, we first need to analyze the phase due to magnetic shift between the optical transition levels. To this aim, we turn to the magnetic part of the free evolution in Eq. 39:

$$H_{\text{mag}} = B_z \left(\gamma_J \boldsymbol{J}_z + \gamma_S \boldsymbol{S}_z\right) + \hbar Q \left(\overrightarrow{\boldsymbol{J}}^2 - 3\boldsymbol{J}_z^2\right).$$

Applying the sequence in section 9.3.3 reduces the evolution to be according to the effective Hamiltonian

$$H_{\text{mag}}^{\text{eff}} = \hbar\omega_{\text{opt}} I_J + B_z \left(\gamma_J \Theta\left(t - \frac{2}{3}T\right)\boldsymbol{J}_z + \gamma_S \boldsymbol{S}_z\right),$$

where here Θ is the Heaviside step function. The magnetic phase shift amounts to:

$$\boldsymbol{\phi}_{\text{mag}} = \frac{1}{\hbar}\int_0^T B_z\gamma_J\Theta\left(t' - \frac{2}{3}T\right)dt'\boldsymbol{J}_z + \int_0^T B_z\gamma_S\boldsymbol{S}_z dt' = \frac{1}{\hbar}B_z\left[\frac{1}{3}\gamma_J T\boldsymbol{J}_z + \gamma_S T\boldsymbol{S}_z\right].$$

In order to eliminate this phase, one can use RF π pulses using the second drive term in 39, $2\hbar\cos\left(\omega_{RF}^S t - \phi_S\right)\left(C_J\left(t\right)\boldsymbol{J}_x + C_S\left(t\right)\boldsymbol{S}_x\right)$. Following the same steps in section 9.3.2 applied for H_S taken in the interaction picture with respect to $\tilde{H}' = \hbar\omega_{RF}^S \boldsymbol{S}_z$, and taking the RWA assuming $\omega_{RF}^S \gg C_0^S \gg Q$, $\frac{B_z\gamma_S}{\hbar} - \omega_{RF}^S = \delta_S$, we get that the interaction Hamiltonian in the S manifold becomes:

$$H_S^{int} = \hbar\delta_S\boldsymbol{S}_z + \hbar C_0^S\left(\cos\left(\phi_S\right)\boldsymbol{S}_x + \sin\left(\phi_S\right)\boldsymbol{S}_y\right).$$

Therefore, similar to section 9.3.2, applying this drive for duration time $\tau = \frac{\pi}{C_0^S}$ yields the pulsed evolution operator

$$U_p^S\left(\phi_S\right) = \exp\left(i\pi\left(\cos\left(\phi_S\right)\boldsymbol{S}_x + \sin\left(\phi_S\right)\boldsymbol{S}_y\right)\right). \tag{44}$$

Applying this π pulse at times $\frac{2}{3}T < t_1 < T$ and the pulse $U_p^S\left(-\phi_S\right)$ at time $t_2 = T$ performs the rotation $\boldsymbol{S}_z \to -\boldsymbol{S}_z$ twice, at times $t_1$and t_2. The evolution is therefore according to the operator:

$$\boldsymbol{\phi}_{\text{mag}} = \frac{1}{\hbar}\int_0^T B_z\gamma_J\Theta\left(t' - \frac{2}{3}T\right)dt'\boldsymbol{J}_z + \int_0^{t_1} B_z\gamma_S\boldsymbol{S}_z dt' - \int_{t_1}^T B_z\gamma_S\boldsymbol{S}_z dt' =$$

$$= \frac{1}{\hbar}B_z\left[\frac{1}{3}\gamma_J T\boldsymbol{J}_z + \gamma_S t_1\boldsymbol{S}_z - \gamma_S\left(T - t_1\right)\boldsymbol{S}_z\right] =$$

$$= \frac{1}{\hbar} B_z \left[\frac{1}{3} \gamma_J T \boldsymbol{J}_z + \gamma_S \left(2t_1 - T\right) \boldsymbol{S}_z \right].$$

Considering an initial superposition $|\psi_{init}\rangle = \frac{1}{\sqrt{2}} \left[|S, m_S\rangle + |J, m_J\rangle \right]$, the final superposition phase is:

$$\exp\left(i\boldsymbol{\phi}_{\text{mag}}\right) |\psi_{init}\rangle =$$

$$= \frac{1}{\sqrt{2}} \left[\exp\left(i \frac{\gamma_S B_z m_S}{\hbar} \left(2t_1 - T\right) \right) |S, m_S\rangle + \exp\left(i \frac{B_z \gamma_J m_J}{3\hbar} T \right) |J, m_J\rangle \right].$$

In order to eliminate this magnetic phase, we need to demand:

$$\frac{\gamma_S B_z m_S}{\hbar} \left(2t_1 - T\right) = \frac{B_z \gamma_J m_J}{3\hbar} T \rightarrow$$

$$\rightarrow t_1 = \frac{1}{2} \left(\frac{\gamma_J m_J}{3\gamma_S m_S} + 1 \right) T. \tag{45}$$

We note that when $\frac{\gamma_J m_J}{3\gamma_S m_S} > 1$, this time exceeds the experiment interrogation time. In this case, the additional π pulse should be applied in the J manifold instead of the S manifold.

9.3.5 Theoretical limits to continuous sequence

In both DD sequences described in sections 9.3.3 and 9.3.4, the approximated Hamiltonian in Eq. 42 was used for continuous pulse operation. In this section, we quantify the residual shifts from deviation from this approximation. In order to obtain the resulting shift from the continuous operation, we compare the entire actual continuous DD part of the evolution with its approximated form. The actual evolution is

$$U_{act} =$$

$$\ldots \exp\left[-i \frac{\pi}{2} \boldsymbol{J}_x \right] \ldots$$

$$\ldots \exp\left[i \frac{T}{3} \left(\delta_J \boldsymbol{J}_z + Q \left(\vec{\boldsymbol{J}}^2 - 3\boldsymbol{J}_z^2 \right) - \Omega_0^J \boldsymbol{J}_y \right) \right] \exp\left[i \frac{T}{3} \left(\delta_J \boldsymbol{J}_z + Q \left(\vec{\boldsymbol{J}}^2 - 3\boldsymbol{J}_z^2 \right) + \Omega_0^J \boldsymbol{J}_y \right) \right] \ldots$$

$$\ldots \exp\left[i \frac{\pi}{2} \boldsymbol{J}_x \right] =$$

$$= \exp\left[i \frac{T}{3} \left(-\delta_J \boldsymbol{J}_y + Q \left(\vec{\boldsymbol{J}}^2 - 3\boldsymbol{J}_y^2 \right) - \Omega_0^J \boldsymbol{J}_z \right) \right] \exp\left[i \frac{T}{3} \left(-\delta_J \boldsymbol{J}_y + Q \left(\vec{\boldsymbol{J}}^2 - 3\boldsymbol{J}_y^2 \right) + \Omega_0^J \boldsymbol{J}_z \right) \right], \tag{46}$$

and the approximated evolution is

$$U_{app} = \exp\left[i \frac{2}{3} Q T \left(\vec{\boldsymbol{J}}^2 - \frac{3}{2} \left(\boldsymbol{J}_x^2 + \boldsymbol{J}_y^2 \right) \right) \right]. \tag{47}$$

We compare the two by numerically evaluating the complex expectation values $\langle J, m_J | U_{act} | J, m_J \rangle$ and $\langle J, m_J | U_{app} | J, m_J \rangle$. First, we compare the square absolute value of these quantities, $\left| \langle J, m_J | U_{act} | J, m_J \rangle \right|^2$ and $\left| \langle J, m_J | U_{app} | J, m_J \rangle \right|^2$.

Due to the fact that $|J, m_J\rangle$ is an eigenstate of U_{app} but not of U_{act}, we would like to verify that $|\langle J, m_J| U_{act} |J, m_J\rangle|^2 \approx 1$, and only negligible population is transferred to other $|J, m'_J\rangle \neq |J, m_J\rangle$ states when operating with U_{act}.

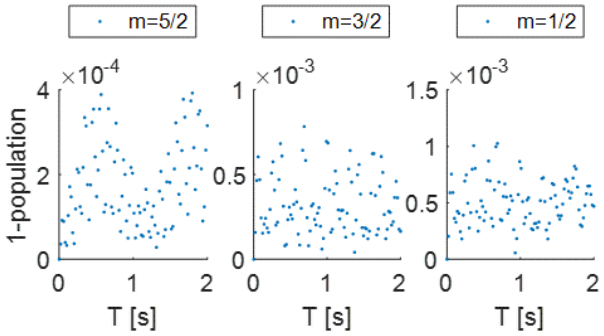

(a)

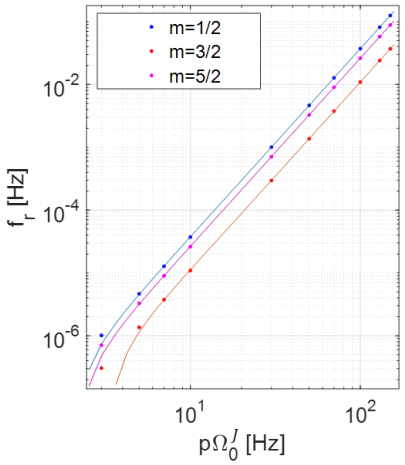

(b)

Figure 36: **Population lost and residual phase in continuous DD sequence.** **(a)** Population lost for different m initial states. The plots show numerically calculated $1 - |\langle m| U_{app}(T) |m\rangle|^2$ as a function of the time T, for initial states $|m\rangle = \left|\frac{5}{2}\right\rangle, \left|\frac{3}{2}\right\rangle, \left|\frac{1}{2}\right\rangle$. **(b)** Residual frequency f_r scaling with p, for different initial m states. The plots show slope extracted from of linear fit to $\phi_{act}(T) - \phi_{app}(T)$ for $|m\rangle = \left|\frac{5}{2}\right\rangle, \left|\frac{3}{2}\right\rangle, \left|\frac{1}{2}\right\rangle$ vs different values of $p\Omega_0$. The fits are to third order polynomial in p. We note that here we show the shift's absolute value. The shift for state $|m\rangle = \left|\frac{1}{2}\right\rangle$ has opposite sign with respect to the other states.

We now assume for simplicity that $\frac{\delta_J}{\Omega_0^J} = \frac{Q}{\Omega_0^J} = p \ll 1$. We calculate the complex amplitudes $\langle m| U_{act}(T) |m\rangle$ and $\langle m| U_{app}(T) |m\rangle$ for interrogation times from $T = 0$ s to $T = 2$ s. For a mutual eigenstate $|m\rangle$ of $\boldsymbol{J}^2$ and $\boldsymbol{J}_z$, we define $\langle m| U_{act}(T) |m\rangle = r_{act} \exp(i\phi_{act})$ and $\langle m| U_{app}(T) |m\rangle = \exp(i\phi_{app})$. In the calculation we set $\Omega_0^J = 2\pi \times 50$kHz. We set the conservative values $\delta_J = Q = 2\pi \times 100$ Hz, and calculate $1 - |\langle m| U_{app}(T) |m\rangle|^2$. The result are shown in Fig. 36a. Fig. 36a shows that this loss in contrast agrees with the scaling of $p^2 = \left(\frac{\delta_J}{\Omega_0^J}\right)^2 = \left(\frac{Q}{\Omega_0^J}\right)^2$, with a prefactor of order 10. These parameters show that this amplitude deviation is small and can be neglected. We therefore need only to account for the phase acquired by the initial state. We turn to evaluate the phase acquired by the initial state when $U_{act}(T)$ or $U_{app}(T)$ are applied. Our figure of merit is $|\phi_{act}(T) - \phi_{app}(T)|$. Again, here we take $\delta_J = Q := p\Omega_0^J$. Using these definitions, residual frequency shift f_r arising from the DD sequence corresponds to $\frac{\partial}{\partial T} |\phi_{act}(T) - \phi_{app}(T)|$. This derivative is estimated through a maximum likelihood fit to a linear function. Fig. 36b shows the scaling of f_r as a function of p.

These calculation results exhibit a cubic scaling in p. As an example, for $p\Omega_0 = 2\pi \times 10$ Hz, the residual shift from the continuous DD part in the sequence is less than 40μHz, which means less than $\approx 9.1 \times 10^{-20}$ relative frequency shift. The population scaling of p^2 and the phase scaling of p^3 are both proved mathematically in an appendix

We also calculated the expected shift for our DD sequence applied on three ions with two parameters choices, in which $Q \neq \delta_J$. The first was using our evaluated experiment parameters: $Q/2\pi = 28, 42, 28$ Hz and $\delta_J/2\pi = -33, 10, 53$ Hz, including our magnetic field gradient and a possible imperfect RF resonance calibration of 10 Hz. First, second and third numbers correspond to ion 1 (left), ion 2 (middle) and ion 3 (right). The second was a typical experimental parameters, where Q_J is the same as in our experiment and $\delta_J/2\pi = 5, 5, 5$ Hz. The resulting residual shift in mHz is given below.

$m = \frac{5}{2}$			
	Ion 1	Ion 2	Ion 3
Our experiment parameters	0.63	1.5	0.92
Typical clock parameters	0.45	1.5	0.45

$m = \frac{3}{2}$			
	Ion 1	Ion 2	Ion 3
Our experiment parameters	0.23	0.89	0.17
Typical clock parameters	0.26	0.89	0.26

$m = \frac{1}{2}$			
	Ion 1	Ion 2	Ion 3
Our experiment parameters	-0.85	-2.4	-1.1
Typical clock parameters	-0.71	-2.4	-0.71

9.3.6 Off resonance magnetic field driving systematic shift

When ω_{RF}^{J} is set to be on resonance with the Zeeman splitting $\frac{B_z\gamma_J}{\hbar}$ in the J manifold, it also off-resonantly driving the S manifold. This is manifested in the Hamiltonian as the driving amplitudes $C_J(t)$ and $\Omega_S(t)$. Since $C_J(t)$ is turned on for a short time during the interrogation, its corresponding shift is negligible. In contrast, $\Omega_S(t)$ is set to Ω_0^S during most of the interrogation due to the continuous nature of the DD sequence. As a result, the two states in the S ground manifold are shifted, in analogy to the AC Stark shift. This shift scales as $\frac{\Omega_S^2}{2\left(\omega_{RF}^{J}-\frac{B_z\gamma_J}{\hbar}\right)}$, and is an unwanted frequency shift affecting the clock's measured frequency and originating in the cancellation sequence described above. In order to mitigate this shift, one could first choose a lower driving field amplitude B_x^J, and therefore reduce this shift quadratically. Another strategy uses the fact that the ground state levels are shifted symmetrically around the zero magnetic field energy. Two approaches can be taken. First, one could incoherently average measurements of two transitions with different m levels, e.g.

$$\left|5S_{\frac{1}{2}},\frac{1}{2}\right\rangle \leftrightarrow \left|4D_{\frac{5}{2}},\frac{3}{2}\right\rangle \text{ and } \left|5S_{\frac{1}{2}},\text{-}\frac{1}{2}\right\rangle \leftrightarrow \left|4D_{\frac{5}{2}},\text{-}\frac{3}{2}\right\rangle.$$

This technique is widely used in current optical atomic clocks to eliminate 1^{st} Zeeman shifts, but has the disadvantage of allowing magnetic field changes between interrogations. Second, additional RF pulses applied on the ground state Zeeman manifold at specific times can eliminate phase accumulation originating in such a symmetric shift, including magnetic field shifts and the shift mentioned above. A third approach, is to add a second driving field during the continuous operation of the ω_{RF}^{J} drive, in order to counter-shift the S manifold and eliminate the effect of Ω_0^S. We note that all these methods can be incorporate together, and therefore reduce this off-resonant shift to be negligible (see supplementary material of [57]).

9.4 Quadrupole and magnetic field shifts cancellation experiment

9.4.1 Correlation spectroscopy

In order to show that our scheme works, we used correlation spectroscopy [58, 59]. Here, instead of measuring the optical frequency of an ion independently, only the difference between the resonance frequency of two ions is detected. Since the quadrupole shift is inhomogeneous, two ions in an ion chain consisting of more than two ions can have different quadrupole shifts, and therefore measuring the difference in their resonance frequency with and without applying our sequence can verify quadrupole shift cancellation. A major advantage of correlation spectroscopy is that it relaxes the requirement for long coherence time. The reason for that is the fact that the ions are measured with respect to each other. Any common mode noisy operation is rejected - does not influence the average measurement outcome. That includes common magnetic field

noise, laser phase noise, common Doppler shifts and so on. Below we analyze the correlation spectroscopy signal for two ions.
Assuming two ions, ion 1 and ion 2, with corresponding resonance frequencies ω_i between their two levels $|S, m_S\rangle_i, |J, m_J\rangle_i$, where i marks the ion number, 1 or 2. A simultaneous Ramsey experiment measuring both the ions frequencies, will look as follows:

1. Both ions are initialized in their ground state:

$$|\psi_0\rangle = |S, m_S\rangle_1 \otimes |S, m_S\rangle_2 .$$

2. Short $\frac{\pi}{2}$ laser pulse with frequency ω_L drives each ion to an equal superposition:

$$|\psi_1\rangle = \frac{1}{\sqrt{2}} \left(|S, m_S\rangle_1 + i\,|J, m_J\rangle_1\right) \otimes \frac{1}{\sqrt{2}} \left(|S, m_S\rangle_2 + i\,|J, m_J\rangle_2\right).$$

3. Free evolution of time τ results in a phase shift $\delta_i \tau = (\omega_i - \omega_L)\,\tau$ for the i'th ion:

$$|\psi_2\rangle = \frac{1}{\sqrt{2}} \left(e^{-i\frac{\delta_1\tau}{2}} |S, m_S\rangle_1 + ie^{i\frac{\delta_1\tau}{2}} |J, m_J\rangle_1\right) \otimes \frac{1}{\sqrt{2}} \left(e^{-i\frac{\delta_2\tau}{2}} |S, m_S\rangle_2 + ie^{i\frac{\delta_2\tau}{2}} |J, m_J\rangle_2\right).$$

4. A second $\frac{\pi}{2}$ pulse with the same frequency ω_L and with phase ϕ drives each ion:

$$\begin{aligned} |\psi_3\rangle = &\left(-ie^{i\frac{\phi}{2}} \sin\left(\frac{\delta_1\tau + \phi}{2}\right) |S, m_S\rangle_1 + ie^{-i\frac{\phi}{2}} \cos\left(\frac{\delta_1\tau + \phi}{2}\right) |J, m_J\rangle_1\right) \otimes ... \\ &... \left(-ie^{i\frac{\phi}{2}} \sin\left(\frac{\delta_2\tau + \phi}{2}\right) |S, m_S\rangle_2 + ie^{-i\frac{\phi}{2}} \cos\left(\frac{\delta_2\tau + \phi}{2}\right) |J, m_J\rangle_2\right). \end{aligned} \tag{48}$$

For a typical Ramsey experiment, the population of the excited state of each ion in $|\psi_3\rangle$ would be measured. However, in case where ϕ is a random variable, due to the fact that ϕ and $\delta_i\tau$ contribute equally to the final state, averaging many realizations would result in a loss of information about δ_1 and δ_2. In case where we are only interested in the frequency difference $\omega_2 - \omega_1$, a different approach can be used. We rewrite Eq. 48 in term of the two-ions states:

$$\begin{aligned} |\psi_3\rangle = &\left(-ie^{i\frac{\phi}{2}} \sin\left(\frac{\delta_1\tau + \phi}{2}\right)\right) \left(-ie^{i\frac{\phi}{2}} \sin\left(\frac{\delta_2\tau + \phi}{2}\right)\right) |S, m_S\rangle_1 \otimes |S, m_S\rangle_2 + ... \\ ... + &\left(-ie^{i\frac{\phi}{2}} \sin\left(\frac{\delta_1\tau + \phi}{2}\right)\right) \left(ie^{-i\frac{\phi}{2}} \cos\left(\frac{\delta_2\tau + \phi}{2}\right)\right) |S, m_S\rangle_1 \otimes |J, m_J\rangle_2 + ... \\ ... + &\left(ie^{-i\frac{\phi}{2}} \cos\left(\frac{\delta_1\tau + \phi}{2}\right)\right) \left(-ie^{i\frac{\phi}{2}} \sin\left(\frac{\delta_2\tau + \phi}{2}\right)\right) |J, m_J\rangle_1 \otimes |S, m_S\rangle_2 + ... \end{aligned}$$

$$... + \left(ie^{-i\frac{\phi}{2}} \cos\left(\frac{\delta_1 \tau + \phi}{2} \right) \right) \left(ie^{-i\frac{\phi}{2}} \cos\left(\frac{\delta_2 \tau + \phi}{2} \right) \right) |J, m_J\rangle_1 \otimes |J, m_J\rangle_2 .$$

Measuring the parity signal, i.e. subtract the probability to be in $|S, m_S\rangle_1 \otimes |J, m_J\rangle_2$or $|J, m_J\rangle_1 \otimes |S, m_S\rangle_2$ from the probability to be in $|S, m_S\rangle_1 \otimes |S, m_S\rangle_2$ or $|J, m_J\rangle_1 \otimes |J, m_J\rangle_2$, results in the signal:

$$\begin{aligned} S_{\text{corr}} &= P\left(|S, m_S\rangle_1 \otimes |S, m_S\rangle_2\right) + P\left(|J, m_J\rangle_1 \otimes |J, m_J\rangle_2\right) - ... \\ &... - P\left(|S, m_S\rangle_1 \otimes |J, m_J\rangle_2\right) + P\left(|J, m_J\rangle_1 \otimes |S, m_S\rangle_2\right) = \\ &= \frac{1}{2}\left[\cos\left(\left(\delta_1 - \delta_2\right)\tau\right) + \cos\left(\left(\delta_1 + \delta_2\right)\tau + 2\phi\right)\right]. \end{aligned}$$

Averaging over many realizations with random ϕ, we obtain the parity signal:

$$\langle S_{\text{corr}} \rangle_\phi = \frac{1}{2}\cos\left(\left(\delta_1 - \delta_2\right)\tau\right) = \frac{1}{2}\cos\left(\left(\omega_1 - \omega_2\right)\tau\right). \tag{49}$$

Note that this parity signal has a reduced contrast by a factor of two, but allows for long coherence times as it does not depend on the random ϕ, which could arise from drifts e.g. in the laser phase, magnetic field and more.

9.4.2 Quadrupole shift inhomogeneity measurement using correlation spectroscopy

We assume an ion chain having an odd number of ions. We denote the ions as ion 1, ion 2 ... ion N, from one edge of the chain to the other edge, such that ion $\frac{N+1}{2}$ sits at position $a = 0$, where a is a coordinate along the trap axial direction $\hat{a}$. A magnetic field in the form of $B(a) = (B_0 + B_1 a)\hat{z}$ is applied at the ions position, causing a different Zeeman splitting between different ions. In addition, according to Eq. 35, different ions exhibit different quadrupole shifts. These shifts are symmetric in position along $\hat{a}$ with respect to $a = 0$, and follow a decreasing function with $|a|$. We can therefore write the frequency shift δ_i of the i'th ion due to both Zeeman and quadrupole shifts as

$$\hbar\delta_i = (B_0 + B_1 a_i)\left(\gamma_J m_J + \gamma_S m_S\right) + \hbar Q_i \left(J\left(J+1\right) - 3m_J^2\right), \tag{50}$$

where a_i and Q_i are the i'th ion axial position and corresponding quadrupole shift respectively. From Eq. 50 we can compute the absolute value of the relative shift between the ions i and j, $\Delta\delta_{i,j}$:

$$\hbar\Delta\delta_{i,j} = \hbar\left|\delta_i - \delta_j\right| = \left| \underbrace{B_1\left(a_i - a_j\right)\left(\gamma_J m_J + \gamma_S m_S\right)}_{\hbar M_{i,j}} + \hbar \underbrace{\left(Q_i - Q_j\right)\left(J\left(J+1\right) - 3m_J^2\right)}_{\hbar Q u_{i,j}} \right|, \tag{51}$$

where $M_{i,j}$ and $Qu_{i,j}$ are the magnetic and quadrupole contributions to the relative shift. According to Eq. 49, parity signal between the ions i and j will have oscillations with frequency $\Delta\delta_{i,j}$. We now demand that for all $i \neq j$,

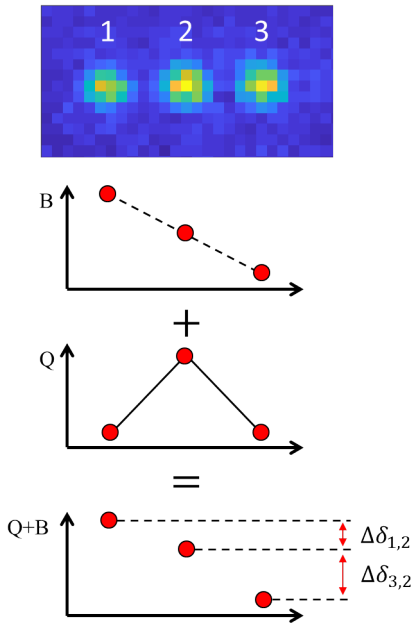

Figure 37: Relative quadrupole and magnetic shifts in a three-ion configuration.

Top: fluorescence of three ions captured on a EMCCD camera, along with ions' assigned numbers. Bottom: magnetic field (B) and quadrupole shift (Q) qualitative dependence on ion position\number. The sum of Zeeman and quadrupole shift leads to $\Delta\delta_{1,2} < \Delta\delta_{3,2}$.

we have $|M_{i,j}| > |Qu_{i,j}|$. This in turn allows us to write $\Delta\delta_{i,j} = |M_{i,j}| + \text{sign}\left(M_{i,j} \cdot Qu_{i,j}\right)|Qu_{i,j}|$. Therefore, it guarantees that by comparing parity measurements of pairs of ions located in symmetry with respect to $a = 0$, both the relative Zeeman shift and the relative quadrupole shift can be inferred independently. Due to the fact that $M_{i,j} = -M_{N+1-i,N+1-j}$ and $Qu_{i,j} = Qu_{N+1-i,N+1-j}$, the relative quadrupole shift between ions i and j will be given by

$$|Qu_{i,j}| = \frac{1}{2}\left|\left(\Delta\delta_{i,j} - \Delta\delta_{N+1-i,N+1-j}\right)\right|, \tag{52}$$

and the relative Zeeman shift is given by

$$|M_{i,j}| = \frac{1}{2}\left|\left(\Delta\delta_{i,j} + \Delta\delta_{N+1-i,N+1-j}\right)\right|. \tag{53}$$

An example for this ion pairs analysis in three ions is given in Fig. 37.

9.4.3 Quadrupole shift cancellation results

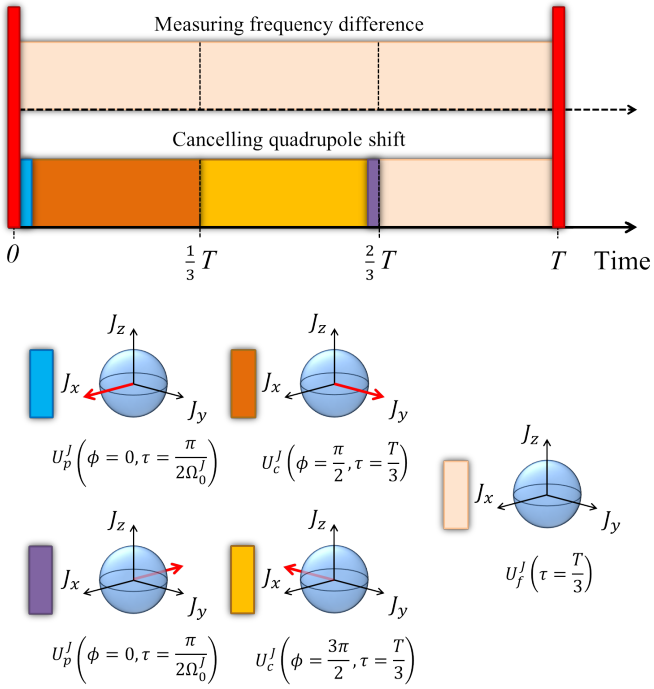

Figure 38: Quadrupole shift cancellation and measurement sequence. Schematic description of experimental sequence for measuring and canceling quadrupole shifts. Red rectangles mark optical $\frac{\pi}{2}$ pulses. Other colors mark RF rotation according to the bottom color code, which shows the operation as defined in section 9.3.2 along with a schematic rotation direction denoted by red arrow on an operator sphere.

In this first experimental demonstration of quadrupole shift cancellation, we used a three $^{88}Sr^{+}$ ion chain. The ions are denoted by numbers, from left to right on the EMCCD camera image (see Fig. 37). In order to test our quadrupole shift cancellation method, we compared two correlation spectroscopy experiments. The first was a standard optical Ramsey experiment, and the second was an optical Ramsey experiment incorporating our RF sequence in the Ramsey wait time. The experimental sequences are laid out in Fig. 38.

The figure of merit we compare between the two experiments is $|Qu_{1,2}|$ defined in Eq. 52. When no RF cancellation is applied, the expected result is $|Qu_{1,2}| > 0$, whereas the RF cancellation should ideally yield $|Qu_{1,2}| = 0$. Fig. 39 shows two parity oscillations, oscillating at $\Delta\delta_{1,2}$ and $\Delta\delta_{3,2}$.

The parity oscillations contain 81 Ramsey time points, each with 1000 repetitions obtained over total averaging time of roughly 4.5 hours. The measurement

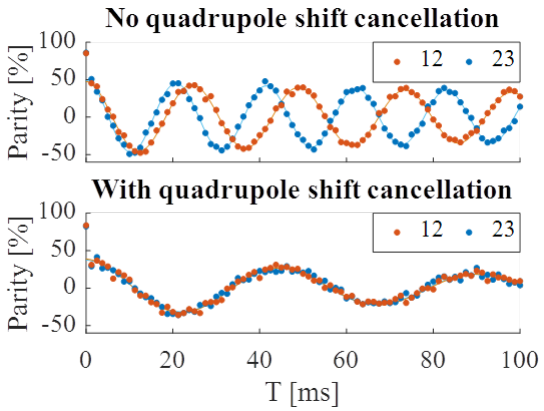

Figure 39: Parity fringes with and without quadrupole shift cancellation sequence.
Top and bottom correspond to the top and bottom sequences in Fig. 38, applied on the initial optical transition $\left|S,-\frac{1}{2}\right\rangle \leftrightarrow \left|D,-\frac{3}{2}\right\rangle$, respectively. When no quadrupole shift cancellation sequence is applied, two different parity frequencies are apparent, $\delta_{1,2}(Orenge) \neq \delta_{3,2}$ (Blue). These frequencies were estimated using a maximum likelihood fit to the data (solid line). The estimated values are $\delta_{1,2}/2\pi = 40.79 \pm 0.07$ Hz and $\delta_{3,2}/2\pi = 48.14 \pm 0.07$ Hz, corresponding to $|Qu_{1,2}| = 3.67 \pm 0.1$ Hz. In the case where the cancellation RF sequence is applied, the two frequencies are $\delta_{1,2}/2\pi = 22.1729 \pm 0.14$ Hz and $\delta_{3,2}/2\pi = 22.2715 \pm 0.15$ Hz. Here, we get $|Qu_{1,2}| = 0.1 \pm 0.2$ Hz, which agrees with zero within statistical uncertainty. The averaged frequency between the two pairs of ions is different in the top and bottom plot. That is due to the fact that in addition to canceling the quadrupole shift, the RF sequence cancels the magnetic contribution in the $\left|D,-\frac{3}{2}\right\rangle$ level for $\frac{2}{3}$ of the total interrogation time.

was done in an interlaced fashion between the quadrupole shift measurement and the cancellation of the quadrupole shift sequences. Here, $\Omega_0^J = 92.6$ kHz. From the figure it is apparent that the quadrupole shift is diminished when the cancellation protocol is used. In order to quantify this cancellation, we repeated the experiment with the cancellation protocol with longer averaging time and less points per fringe. In addition, we performed the protocol for two optical superpositions that differ by their m_J number: $\left|S,-\frac{1}{2}\right\rangle \leftrightarrow \left|D,-\frac{3}{2}\right\rangle$ and $\left|S,-\frac{1}{2}\right\rangle \leftrightarrow \left|D,\frac{1}{2}\right\rangle$. Results of this analysis are shown in Fig. 40.

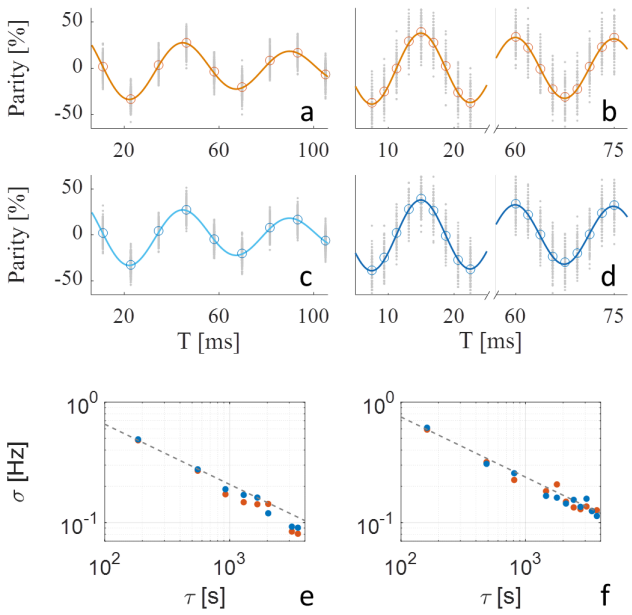

Figure 40: Correlations comparison after long averaging times. **(a,b)** Correlations of ion pair 1,2 using transition between levels $\left|S,-\frac{1}{2}\right\rangle \leftrightarrow \left|D,-\frac{3}{2}\right\rangle$ and $\left|S,-\frac{1}{2}\right\rangle \leftrightarrow \left|D,\frac{1}{2}\right\rangle$ respectively. **(c,d)** Correlations of ion pair 1,2 using transition between levels $\left|S,-\frac{1}{2}\right\rangle \leftrightarrow \left|D,-\frac{3}{2}\right\rangle$ and $\left|S,-\frac{1}{2}\right\rangle \leftrightarrow \left|D,\frac{1}{2}\right\rangle$ respectively. Grey points mark the measured data in a single realization fringe, empty circles are the averaged measurements over the entire experimental data set and solid lines are a maximum likelihood fit to the averaged data, as a guide to the eye. **(e,f)** Frequency Allan deviation for the transitions $\left|S,-\frac{1}{2}\right\rangle \leftrightarrow \left|D,-\frac{3}{2}\right\rangle$ and $\left|S,-\frac{1}{2}\right\rangle \leftrightarrow \left|D,\frac{1}{2}\right\rangle$ respectively. The total integration time was 20.5 and 14 hours with 1200 and 626 frequency points for the transitions $\left|S,-\frac{1}{2}\right\rangle \leftrightarrow \left|D,-\frac{3}{2}\right\rangle$ and $\left|S,-\frac{1}{2}\right\rangle \leftrightarrow \left|D,\frac{1}{2}\right\rangle$ respectively. In the $\left|S,-\frac{1}{2}\right\rangle \leftrightarrow \left|D,-\frac{3}{2}\right\rangle$case, the correlation frequencies are $\Delta\delta_{1,2} = 22.146 \pm 0.024$ Hz and $\Delta\delta_{3,2} = 22.168 \pm 0.024$ Hz, agreeing within $1\,\sigma$. In the $\left|S,-\frac{1}{2}\right\rangle \leftrightarrow \left|D,-\frac{1}{2}\right\rangle$case, the correlation frequencies are $\Delta\delta_{1,2} = 66.722 \pm 0.034$ Hz and $\Delta\delta_{3,2} = 66.768 \pm 0.034$ Hz, and the agreement is within $1.3\,\sigma$.

With longer averaging time, we could infer that under our protocol, the two ion-pair correlations 1,2 and 3,2 agree within 1 and 1.3 standard deviations, corresponding to 22 and 46 mHz, a relative difference of 5×10^{-17} and 1.05×10^{-16} over the optical frequency of 4.4×10^{14} Hz respectively. This difference between correlations could be explained by other position dependent effects, such as magnetic field term which is quadratic with position, position-dependent ion velocity, letting relativistic Doppler effects cause inhomogeneous frequency change or spatial dependent light shifts from laser light leaking to the trap.

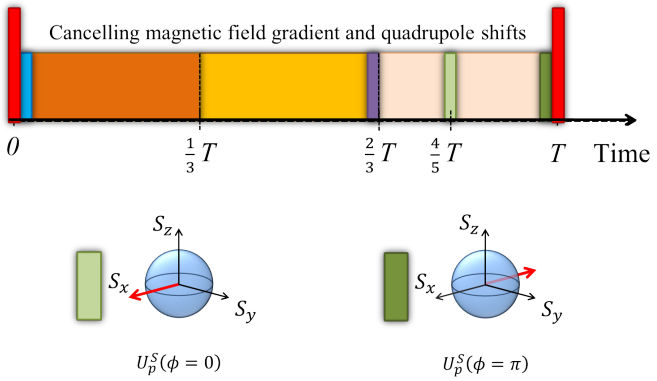

Figure 41: Quadrupole and magnetic field shifts cancellation.
The sequence is illustrated using a color code similar to the one in Fig. 38, with added ground state rotations. This sequence applies to cancellation of quadrupole shift and magnetic field with the chosen superposition $\left|S,-\frac{1}{2}\right\rangle \leftrightarrow \left|D,-\frac{3}{2}\right\rangle$, and the pulse time $\frac{4}{5}T$ is chosen according to Eq. 45 for the case of $^{88}Sr^{+}$.

9.4.4 Quadrupole shift and 1^{st} Zeeman shift cancellation results

In the second experiment, we added two RF π pulses resonant with the $\left|S,-\frac{1}{2}\right\rangle \leftrightarrow \left|S,\frac{1}{2}\right\rangle$ transition, in order to eliminate magnetic field shifts, according to the premise of section 9.3.4. Here, we again compared a simple optical Ramsey experiment with the cancellation sequence. The cancellation sequence is shown in Fig. 41.

To show the scalability of our method, we performed this experiment on a seven-ion chain. The results of the bare Ramsey sequence are shown in Fig. 42 along with an EMCCD image of the ion chain. These include all ion-pair correlations.

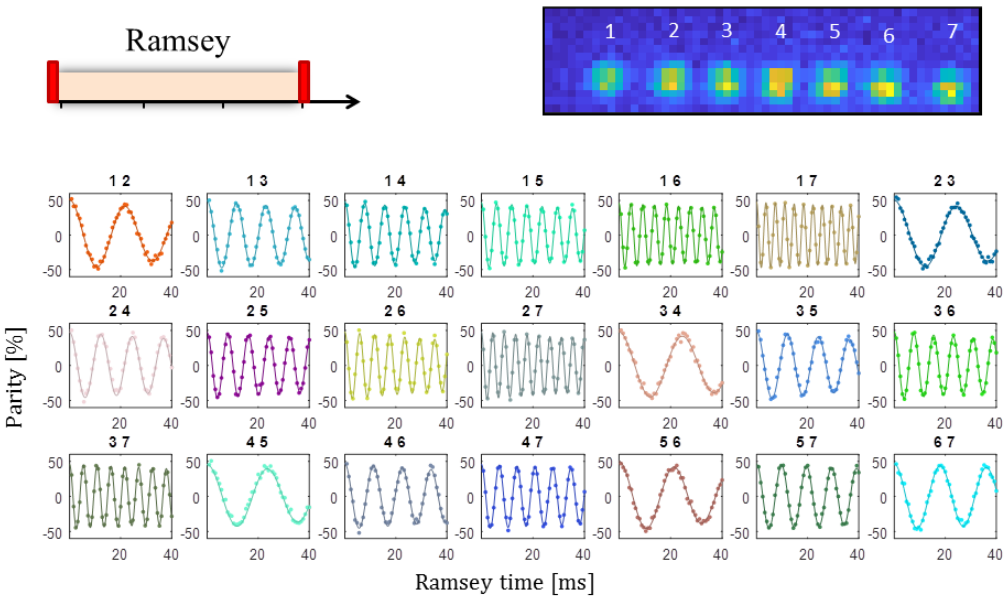

Figure 42: Seven-ion chain correlation spectroscopy Ramsey experiment. **Top left, right**: Experimental sequence of an optical Ramsey experiment schematics, and an EMCCD camera image of fluorescence from seven trapped ions with their corresponding numbers. **Bottom**: 21 pair-wise correlations in the ion chain. Each plot is titled with the two digits of its corresponding ions correlations. As is seen, each pair of ions has a different relative frequency, indicating high inhomogeneity in the ion chain.

From these results, we can infer that the ions' frequencies are inhomogeneous. For a more quantitative statement, we determine this inhomogeneity by computing the different shifts, magnetic and quadrupole and plot them as a function of position. These results are shown in Fig. 43

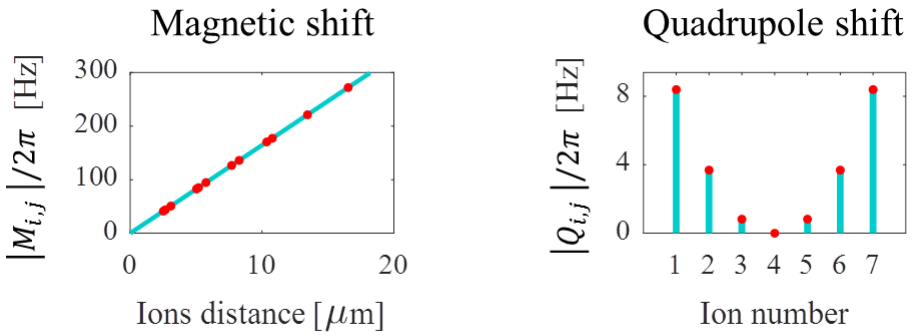

Figure 43: Seven-ion pairwise relative quadrupole are Zeeman shifts. Here, we compute the Zeeman shift gradient using Eq. 53 and taking the ions distances into account, and we get $\approx 16 \frac{\text{Hz}}{\mu m}$. In addition, we set the reference level of the quadrupole shift to be zero for ion 4, and we can calculate the relative quadrupole shift according to Eq. 52. We measure inhomogeneity of up to 8 Hzfrom quadrupole shift alone.

These results show that for our system parameters, indeed the ions frequency is different by relative change of up to 6×10^{-13} due to magnetic field difference and up to 2×10^{-14} due to quadrupole shift difference. Next, we implemented the sequence schematically shown in Fig. 41, and measured the corresponding 21 parity fringes. The results are presented in Fig. 44. From the comparison between the cancellation results and the bare Ramsey results it is evident that using our Zeeman and quadrupole cancellation sequence diminishes the inhomogeneity between the ions significantly.

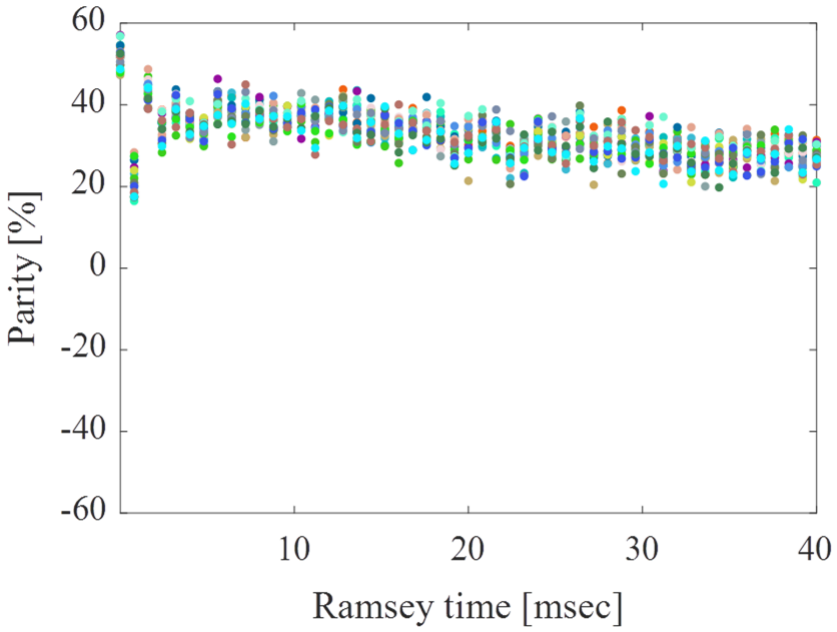

Figure 44: Quadrupole and Zeeman shifts cancellation results.
All 21 parity measurements of the seven-ion chain after a quadrupole and Zeeman shifts cancellation sequence plot together. Color code matches the one from Fig. 42. These results exhibit no oscillation at all, indicating that all ions have the same frequency. At Ramsey times below 5 ms, the relative laser phase between the two Ramsey optical $\frac{\pi}{2}$ pulses is not yet completely randomized, and therefore the averaged result in Eq. 49 does not fully describe the results at short times. Fitting this data to the theory gives frequency consistent with zero.

9.4.5 Contrast dependence on RF sequences

The sections above prove that our sequences can indeed mitigate inhomogeneous broadening due to quadrupole and Zeeman shift. However, in the above comparisons between bare Ramsey and cancellation sequences, we observed a decrease in parity fringe contrast. We believe that this decrease comes a partial overlap between the continuous DD sequence, in particular its Rabi frequency, and the magnetic noise spectrum. The dynamical decoupling sequence mitigates noise spectral components not resonant with it, but can act as a incoherent locking amplifier for overlapping spectral components. We suspect that during this experiment fast magnetic noise was present, and therefore was partially amplified by the DD Rabi oscillation at $\Omega_0^J = 2\pi \times 92.6$ kHz. In order to check this hypothesis, we performed a comparison between two realizations of an experiment

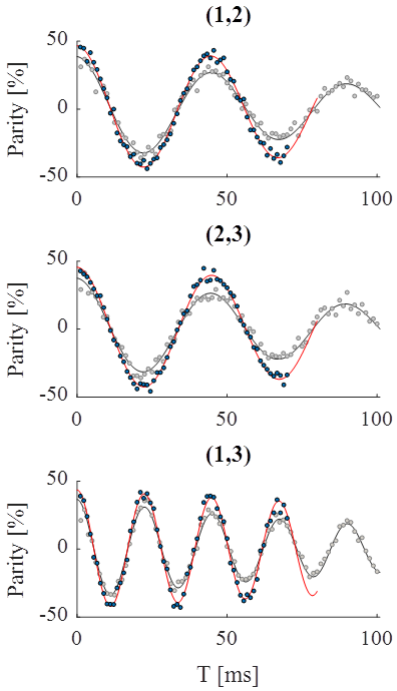

Figure 45: Comparison between DD with two RF magnetic field amplitudes. **Top to Bottom**: Parity fringes of ion pairs 1,2, 2,3 and 1,3 respectively. Grey and blue full circles are parity measurements of $\Omega_0^J = 2\pi \times 92.6$ kHz and $\Omega_0^J = 2\pi \times 47.9$ kHz respectively. Red and gray solid lines are theoretical corresponding fits to the data.

similar to the one shown in Fig. 39, with different Ω_0^J values of $2\pi \times 92.6$ and 47.9 kHz. This comparison is displayed in Fig. 45

Quantitatively, we can compare these two measurements by comparing contrast and decay time fit parameters. This comparison is summarized in Fig. 46

This comparison reinforces our hypothesis that the contrast reduction is related to RF power. Moreover, it means that this contrast reduction can be overcome by characterizing the magnetic field noise and choosing the right Rabi frequency Ω_0^J. We would like, to stress, however, that our lab conditions regarding magnetic field were not ideal for clock measurements, and in a typical high precision clock experiment magnetic field noise is reduced to further extent compared to the noise in our experiment. Without giving full noise analysis, in our lab we have typically magnetic field noise of $100's$ of μG at 50 Hz, whereas clock experiments are done in the few μG at 50 Hz.

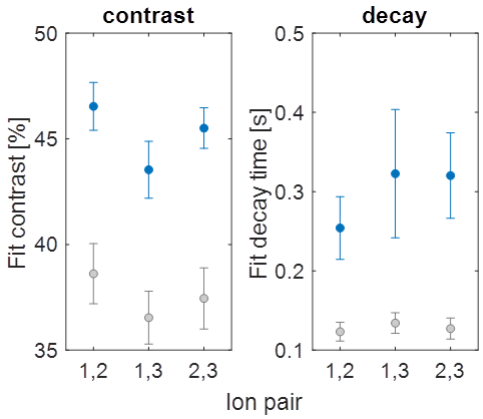

Figure 46: Contrast and decay time comparison between two RF amplitudes. These results show that reducing the RF power of the DD sequence improves contrast by a factor of roughly 20 % and prolong the decay time by roughly 200 %.

10 Discussion and outlook

In my thesis, I described a number of experiments, all under the umbrella topic of "quantum metrology". The main message I want to convey in my thesis is that QIP methods can provide important tools for quantum metrology, and perhaps in some cases provide an easy bypass for otherwise very challenging measurements. In particular, the notion of DD can be of importance to precision measurements, and even be used for the most accurate measurements, as in optical atomic clocks. The concept of DD supposedly adds complications to a frequency interrogation sequence. This may be different from the common view of making everything as simple as possible, but here we show that it can have an added value for either measuring or even eliminating systematic shifts in a coherent way. I also want to emphasis that DD, which is now an integral part of almost any QIP experiment, can be generalized from completely decoupling qubits from their environment to partially decoupling a quantum system from the environmental noise while leaving it a probe for the environment. I demonstrated it here by using a large spin instead of the standard two level system as a probe, and I showed that linear effects e.g. Zeeman shifts can be mitigated while quadratic shifts are measured.

As an outlook, I would like to mention that the LLI test experiment is planed to be performed by the group of Prof. Tanja mehlstäubler in PTB, Germany, where it would be carried out on a chain of tens of Yb^+ ions. It is projected to give a better bound on LLI violation than the best bound to date, also given by an experiment in the PTB. I would also like to mention that, although without a complete experimental proposal, we believe that LLI tests with our DD method could be performed on hot atoms in a vapor cell. This may improve

the sensitivity with respect to cold atom experiments due to the atom number, although much shorter interrogation times are possible.

I would also like to mention that the DD method used here in the context of force detection is actually a way to measure small oscillatory changes in an optical frequency. As such, it can be used for other purposes, such as dark matter searches [35].

To conclude, I believe that the tools of quantum metrology, including those taken from QIP like DD, provide a wide variety of building blocks, from which control sequences performed on a quantum system can be composed, which can increase precision and accuracy of measurements of physical quantities of interests.

A Residual quadrupole and magnetic shift scaling

We define: $\boldsymbol{V} = -\frac{\delta}{\Omega_0}\boldsymbol{J}_y - \frac{3Q_J}{2\Omega_0}\left(\boldsymbol{J}_y^2 - \boldsymbol{J}_x^2\right)$ and $\boldsymbol{H} = \frac{Q_J}{\Omega_0}\left(\boldsymbol{J}^2 - \frac{3}{2}\left(\boldsymbol{J}_y^2 + \boldsymbol{J}_x^2\right)\right)$, and we note that $\boldsymbol{V}$ has zeros for its diagonal elements, while $\boldsymbol{H}$ is diagonal with diagonal elements different from zero. Using these definitions we rewrite the operators U_{act} and U_{app}:

$$U_{act}\left(T\right) = \exp\left[i\frac{\Omega_0 T}{3}\left(\boldsymbol{V} + \boldsymbol{H} - \boldsymbol{J}_z\right)\right]\exp\left[i\frac{\Omega_0 T}{3}\left(\boldsymbol{V} + \boldsymbol{H} + \boldsymbol{J}_z\right)\right], \tag{54}$$

$$U_{app}\left(T\right) = \exp\left[i\frac{2\Omega_0 T}{3}\boldsymbol{H}\right]. \tag{55}$$

The latter has magnitude of unity due to the fact that $|m\rangle$ is an eigenstate of $\boldsymbol{H}$. We denote the $\boldsymbol{H}$ eigenvalue corresponding to $|m\rangle$ by h_m. With this notation, we write $\phi_{app} = \frac{\Omega_0 T}{3} \times 2h_m$

We now assume for simplicity that $\frac{\delta}{\Omega_0} = \frac{Q_J}{\Omega_0} = p \ll 1$, and note that the operators $\boldsymbol{V}, \boldsymbol{H}$ and the number h_m are proportional to p. We now turn to prove that the elements that contribute to the phase $\phi_{act} - \phi_{app}$ with the lowest power in p are proportional to $p^3\Omega_0 T$.

A.1 Theoretical proof for p^3 scaling

We examine the quantity $\langle m| U_{act}\left(T\right) U_{app}^{\dagger}\left(T\right)|m\rangle = r_{act}\exp\left(i\left(\phi_{act} - \phi_{app}\right)\right) = g\left(p, \Omega_0, \right) + if\left(p, \Omega_0, \right)$, where f and g are real functions describing real and imaginary parts.

A.1.1 Reduction to imaginary part

We claim that the lowest power of p in a Taylor expansion of the phase $\phi_{act} - \phi_{app}$ is equal to the lowest power of p in the Taylor expansion of the imaginary part f. Since $g\left(0, \Omega_0\right) = 1$ and $f\left(0, \Omega_0\right) = 0$ (see Eq. 46 and Eq. 47), we can write $g\left(p, \Omega_0\right) = 1 + (\text{powers of } p)$, and $f\left(p, \Omega_0\right) = 0 + (\text{powers of } p)$. This leads

to the conclusion that the lowest power of p in the expansion of the phase of $\langle m| U_{act}U_{app}^{\dagger}(T)|m\rangle$, which is $\arctan\left(\frac{f(p,\Omega_0)}{g(p,\Omega_0)}\right)$, has the same lowest power of p as $f(p,\Omega_0)$. Therefore, it is sufficient to prove that $f(p,\Omega_0)$ does not contain a linear or quadratic p term.

A.1.2 p3 scale

We now expand $\langle m| U_{act}U_{app}^{\dagger}(T)|m\rangle$ in a Taylor series:

$$\langle m| U_{act}U_{app}^{\dagger}|m\rangle = \sum_{n,k}\frac{1}{n!k!}\left(i\frac{\Omega_0 T}{3}\right)^{n+k}\underbrace{\langle m|\left(\boldsymbol{V}+\boldsymbol{H}-h_m\boldsymbol{I}+\boldsymbol{J}_z\right)^n\left(\boldsymbol{V}+\boldsymbol{H}-h_m\boldsymbol{I}-\boldsymbol{J}_z\right)^k|m\rangle}_{T_{nk}}, \tag{56}$$

where $\boldsymbol{I}$ is the unity operator and where we defined T_{nk} as a sum coefficient. T_{nk} can be written as summation over terms proportional to

$$\langle m|...\left[\left(\boldsymbol{H}-h_m\boldsymbol{I}\right)^{l_i}\boldsymbol{J}_z^{j_i}\left(-\boldsymbol{J}_z\right)^{j_i'}\boldsymbol{V}^{v_i}\right]\left[\left(\boldsymbol{H}-h_m\boldsymbol{I}\right)^{l_{i+1}}\boldsymbol{J}_z^{j_{i+1}}\left(-\boldsymbol{J}_z\right)^{j_{i+1}'}\boldsymbol{V}^{v_{i+1}}\right]...|m\rangle, \tag{57}$$

where for each $i=1,2,3,...,n+k$ one and only one of $\{l_i,j_i,j_i',v_i\}$ is 1 and the rest are zeros, $\sum_i(j_i)\leq n$, $\sum_i(j_i')\leq k$ and $\sum_i(l_i+j_i+j_i'+v_i)=n+k$.

We now prove two statements:

(*) All terms in which $\sum_i(v_i)=0$ cancel out.

proof:

Since $(\boldsymbol{J}_z)$ and $(\boldsymbol{H}-h_m\boldsymbol{I})$ commute, these terms can be written as: $\langle m|\boldsymbol{J}_z^{\sum_i j_i}\left(-\boldsymbol{J}_z\right)^{\sum_i j_i'}\left(\boldsymbol{H}-h_m\boldsymbol{I}\right)^{\sum_i l_i}|m$ In cases where $\sum_i l_i\neq 0$, the above expression equals $\langle m|\boldsymbol{J}_z^{\sum_i j_i}\left(-\boldsymbol{J}_z\right)^{\sum_i j_i'}|m\rangle\left(h_m-h_m\right)^{\sum_i l_i}=0$. In cases where $\sum_i l_i=0$, the sum over all terms with $n+k=d$ takes the form $\sum_n\frac{n!}{(n)!(d-n)!}\langle m|\left(\boldsymbol{J}_z\right)^n\left(-\boldsymbol{J}_z\right)^k|m\rangle=\langle m|\left(\boldsymbol{J}_z-\boldsymbol{J}_z\right)^d|m\rangle=0$.

(**) Terms in which $\sum_i(v_i)=1$ always vanish.

proof:

Due to the fact that $(\boldsymbol{V})$ has only zeros as its diagonal elements, it transforms a state $|m\rangle$ to a state orthogonal to it. On the other hand, both $(\boldsymbol{H}-h_m\boldsymbol{I})$ and $\boldsymbol{J}_z$ are diagonal in the $|m\rangle$ basis, and therefore transforms a state $|m\rangle$ to a state proportional to it. As a result, the state $\left(\boldsymbol{H}-h_m\boldsymbol{I}\right)^a\boldsymbol{J}_z^b\left(-\boldsymbol{J}_z\right)^c\boldsymbol{V}\left(\boldsymbol{H}-h_m\boldsymbol{I}\right)^{a'}\boldsymbol{J}_z^{b'}\left(-\boldsymbol{J}_z\right)^{c'}|m\rangle$, for integer a,b,c,a',b',c', must be orthogonal to $|m\rangle$.

Statements **(*)** and **(**)** prove that all terms proportional to p vanish.

Only T_{nk} terms in which $n+k$ is odd contribute to $f(p,\Omega_0)$. Therefore, we prove that terms proportional to p^2 cancel out for odd $n+k$. Terms proportional to p^2 are divided to three types:

1 - $\sum_i v_i=0$ and $\sum_i l_i=2$

2 - $\sum_i v_i=1$ and $\sum_i l_i=1$

3 - $\sum_i v_i=2$ and $\sum_i l_i=0$

Types 1 and 2 vanish due to the two statements **(*)** and **(**)** above. We now deal with type 3. As is written above, only terms with odd $n+k$ contribute to $f(p,\Omega_0)$. We assume a term in T_{nk} in which $n+k$ is odd and $\sum_i v_i=2$ and $\sum_i l_i=0$. We must have $\sum_i j_i+\sum_i j_i'=n+k-2$, and that means that either

$\sum_i j_i$ is odd and $\sum_i j_i'$ is even, or $\sum_i j_i$ is even and $\sum_i j_i'$ is odd. In either case, a similar term with switched $\sum_i j_i$ and $\sum_i j_i'$ must appear in T_{kn}, and due to opposite sign, these terms will cancel in summation.

A.1.3 Bound for the residual phase

We would now show that the phase $\phi_{act} - \phi_{app}$ has a dominant part proportional to $p^3\Omega_0 T$. We will show it in an example for $J = \frac{5}{2}$ spin and for the state $\left|m = \frac{5}{2}\right\rangle$. We now look at all the imaginary terms in Eq. 56, meaning terms for which $n + k$ is odd, and are proportional to p^3. These terms must be in one of two forms:

1. $\langle m| \left(\boldsymbol{J}_z\right)^{g_1} \boldsymbol{V} \left(\boldsymbol{J}_z\right)^{g_2} \boldsymbol{V} \left(\boldsymbol{J}_z\right)^{g_3} \boldsymbol{V} \left(\boldsymbol{J}_z\right)^{g_4} |m\rangle$,
2. $\langle m| \left(\boldsymbol{J}_z\right)^{g_1} \boldsymbol{V} \left(\boldsymbol{J}_z\right)^{g_2} \left(\boldsymbol{H} - h_m \boldsymbol{I}\right) \left(\boldsymbol{J}_z\right)^{g_3} \boldsymbol{V} \left(\boldsymbol{J}_z\right)^{g_4} |m\rangle$.

Note that $g_1 + g_2 + g_3 + g_4 = n + k - 3$. In addition, these terms must have even number of $(-\boldsymbol{J}_z)$ and even number of $(\boldsymbol{J}_z)$, because all terms that do not satisfy this condition cancel in summation with a corresponding term in T_{kn}. We now calculate each of these two terms for some choice of g_1, g_2, g_3, g_4 for $\left|m = \frac{5}{2}\right\rangle$:

We begin with type 1 term. The operator $\boldsymbol{V}$ couples a state $|m\rangle$ to the states $|m+1\rangle, |m+2\rangle, |m-1\rangle, |m-2\rangle$, with the coefficients $v_{m\to m+1}, v_{m\to m+2}, v_{m\to m-1}, v_{m\to m-2}$ respectively. We can therefore compute:

$$\left\langle \frac{5}{2} \right| \left(\boldsymbol{J}_z\right)^{g_1} \boldsymbol{V} \left(\boldsymbol{J}_z\right)^{g_2} \boldsymbol{V} \left(\boldsymbol{J}_z\right)^{g_3} \boldsymbol{V} \left(\boldsymbol{J}_z\right)^{g_4} \left| \frac{5}{2} \right\rangle =$$
$$\left(\frac{5}{2}\right)^{g_1+g_4} \left[\left(\frac{3}{2}\right)^{g_2} \left(\frac{1}{2}\right)^{g_3} V_{\frac{3}{2}\to\frac{5}{2}} V_{\frac{1}{2}\to\frac{3}{2}} V_{\frac{5}{2}\to\frac{1}{2}} + \left(\frac{1}{2}\right)^{g_2} \left(\frac{3}{2}\right)^{g_3} V_{\frac{1}{2}\to\frac{5}{2}} V_{\frac{3}{2}\to\frac{1}{2}} V_{\frac{5}{2}\to\frac{3}{2}} \right] \tag{58}$$

Next, we compute type 2 term:

$$\left\langle \frac{5}{2} \right| \left(\boldsymbol{J}_z\right)^{g_1} \boldsymbol{V} \left(\boldsymbol{J}_z\right)^{g_2} \left(\boldsymbol{H} - h_{\frac{5}{2}} \boldsymbol{I}\right) \left(\boldsymbol{J}_z\right)^{g_3} \boldsymbol{V} \left(\boldsymbol{J}_z\right)^{g_4} \left| \frac{5}{2} \right\rangle = \tag{59}$$
$$\left(\frac{5}{2}\right)^{g_1+g_4} \left[V_{\frac{3}{2}\to\frac{5}{2}} V_{\frac{5}{2}\to\frac{3}{2}} \left(h_{\frac{3}{2}} - h_{\frac{5}{2}}\right) \left(\frac{3}{2}\right)^{g_2+g_3} + V_{\frac{1}{2}\to\frac{5}{2}} V_{\frac{5}{2}\to\frac{1}{2}} \left(h_{\frac{1}{2}} - h_{\frac{5}{2}}\right) \left(\frac{1}{2}\right)^{g_2+g_3} \right] \tag{60}$$

When we plug the numbers $V_{\frac{5}{2}\to\frac{3}{2}} = p(-i\frac{\sqrt{5}}{2})$, $V_{\frac{5}{2}\to\frac{1}{2}} = p(3\sqrt{\frac{5}{2}})$, $V_{\frac{3}{2}\to\frac{1}{2}} = p(i\sqrt{2})$, $h_{\frac{3}{2}} - h_{\frac{5}{2}} = -6p$ and $h_{\frac{1}{2}} - h_{\frac{5}{2}} = -9p$ we obtain:

$$\left\langle \frac{5}{2} \right| \left(\boldsymbol{J}_z\right)^{g_1} \boldsymbol{V} \left(\boldsymbol{J}_z\right)^{g_2} \boldsymbol{V} \left(\boldsymbol{J}_z\right)^{g_3} \boldsymbol{V} \left(\boldsymbol{J}_z\right)^{g_4} \left| \frac{5}{2} \right\rangle =$$
$$p^3 \left(-\frac{15}{2}\right) \left(\frac{5}{2}\right)^{g_1+g_4} \left[\left(\frac{3}{2}\right)^{g_2} \left(\frac{1}{2}\right)^{g_3} + \left(\frac{1}{2}\right)^{g_2} \left(\frac{3}{2}\right)^{g_3} \right] \tag{61}$$

and

$$\langle m|\left(\boldsymbol{J}_z\right)^{g_1}\boldsymbol{V}\left(\boldsymbol{J}_z\right)^{g_2}\left(\boldsymbol{H}-h_m\boldsymbol{I}\right)\left(\boldsymbol{J}_z\right)^{g_3}\boldsymbol{V}\left(\boldsymbol{J}_z\right)^{g_4}|m\rangle = \\ p^3\left(\frac{5}{4}\right)\left(\frac{5}{2}\right)^{g_1+g_4}\left[(-6)\left(\frac{3}{2}\right)^{g_2+g_3}+(-9)\left(\frac{1}{2}\right)^{g_2+g_3}\right] \quad (62)$$

These calculations show that both terms have the same sign. In addition, we write that replacing each of the operators $\boldsymbol{V}$ and $\boldsymbol{H}-h_{\frac{5}{2}}\boldsymbol{I}$ with the operator $\left(h_{\frac{1}{2}}-h_{\frac{5}{2}}\right)\boldsymbol{I}$ yields a more negative number for any choice of g_1,g_2,g_3,g_4:

$$\left\langle\frac{5}{2}\right|\left(\boldsymbol{J}_z\right)^{g_1}\left(h_{\frac{1}{2}}-h_{\frac{5}{2}}\right)\boldsymbol{I}\left(\boldsymbol{J}_z\right)^{g_2}\left(h_{\frac{1}{2}}-h_{\frac{5}{2}}\right)\boldsymbol{I}\left(\boldsymbol{J}_z\right)^{g_3}\left(h_{\frac{1}{2}}-h_{\frac{5}{2}}\right)\boldsymbol{I}\left(\boldsymbol{J}_z\right)^{g_4}\left|\frac{5}{2}\right\rangle = p^3\left(-27\right)\left(\frac{5}{2}\right)^{g_1+g_2+g_3+g_4} \quad (63)$$

This means that the sum

$$p^3\left(-27\right)\sum_{d\geq 3 \text{ odd}}\sum_{n=0}^{d}\frac{1}{n!\left(d-n\right)!}\left(i\frac{\Omega_0 T}{3}\right)^d\left(\frac{5}{2}\right)^{d-3} \quad (64)$$

places a conservative bound on the residual phase. This sum is easily calculated and is equal to

$$ip^3\left(\frac{2}{5}\right)^3\left(-27\right)\left(\sin\left(2\frac{\Omega_0 T}{3}\times\frac{5}{2}\right)+\left(2\frac{\Omega_0 T}{3}\times\frac{5}{2}\right)\right) \quad (65)$$

which is the sum of a linear and a bounded oscillating terms, both scale as p^3.

To conclude, we proved that the residual frequency difference, f_r, between the operation of actual DD operator and the approximated one enters to leading order as a linear combination of terms scaling as $\frac{\delta^3}{\Omega_0^3}\Omega_0$, $\frac{\delta^2 Q_J}{\Omega_0^3}\Omega_0$, $\frac{\delta Q_J^2}{\Omega_0^3}\Omega_0$ and $\frac{Q_J^3}{\Omega_0^3}\Omega_0$, with an added bounded oscillating term. In addition, the statements **(*)** and **(**)** also prove that r_{act} deviates from 1 only as of p^2 to first order.

Note: For clarity, the proof assumed $\frac{\delta}{\Omega_0}=\frac{Q_J}{\Omega_0}=p$. A similar proof holds when using $p_1=\frac{\delta}{\Omega_0}$ and $p_2=\frac{Q_J}{\Omega_0}$, and the conclusion above is still derived.

References

[1] David J Wineland, C Monroe, Wayne M Itano, Dietrich Leibfried, Brian E King, and Dawn M Meekhof. Experimental issues in coherent quantum-state manipulation of trapped atomic ions. *Journal of Research of the National Institute of Standards and Technology*, 103(3):259, 1998.

[2] Juan I Cirac and Peter Zoller. Quantum computations with cold trapped ions. *Physical review letters*, 74(20):4091, 1995.

[3] Hartmut Häffner, Christian F Roos, and Rainer Blatt. Quantum computing with trapped ions. *Physics reports*, 469(4):155–203, 2008.

[4] Michel H Devoret, Andreas Wallraff, and John M Martinis. Superconducting qubits: A short review. *arXiv preprint cond-mat/0411174*, 2004.

[5] Jeremy L O'brien. Optical quantum computing. *Science*, 318(5856):1567–1570, 2007.

[6] Mark Saffman, Thad G Walker, and Klaus Mølmer. Quantum information with rydberg atoms. *Reviews of Modern Physics*, 82(3):2313, 2010.

[7] Daniel A Lidar and Todd A Brun. *Quantum error correction*. Cambridge university press, 2013.

[8] Tom Manovitz, Amit Rotem, Ravid Shaniv, Itsik Cohen, Yotam Shapira, Nitzan Akerman, Alex Retzker, and Roee Ozeri. Fast dynamical decoupling of the mølmer-sørensen entangling gate. *Physical review letters*, 119(22):220505, 2017.

[9] Yotam Shapira, Ravid Shaniv, Tom Manovitz, Nitzan Akerman, and Roee Ozeri. Robust entanglement gates for trapped-ion qubits. *arXiv preprint arXiv:1805.06806*, 2018.

[10] Michael J Biercuk, Hermann Uys, Joe W Britton, Aaron P VanDevender, and John J Bollinger. Ultrasensitive detection of force and displacement using trapped ions. *Nature nanotechnology*, 5(9):646, 2010.

[11] Ravid Shaniv and Roee Ozeri. Quantum lock-in force sensing using optical clock doppler velocimetry. *Nature Communications*, 8:ncomms14157, 2017.

[12] I Baumgart, J-M Cai, A Retzker, Martin B Plenio, and Ch Wunderlich. Ultrasensitive magnetometer using a single atom. *Physical review letters*, 116(24):240801, 2016.

[13] Ravid Shaniv, Nitzan Akerman, and Roee Ozeri. Atomic quadrupole moment measurement using dynamic decoupling. *Physical review letters*, 116(14):140801, 2016.

[14] HS Margolis. Trapped ion optical clocks. *The European Physical Journal Special Topics*, 172(1):97–107, 2009.

[15] Andrew D Ludlow, Martin M Boyd, Jun Ye, Ekkehard Peik, and Piet O Schmidt. Optical atomic clocks. *Reviews of Modern Physics*, 87(2):637, 2015.

[16] SM Brewer, J-S Chen, AM Hankin, ER Clements, CW Chou, DJ Wineland, DB Hume, and DR Leibrandt. An $^{27}Al^{+}$ quantum-logic clock with systematic uncertainty below 10^{-18}. *arXiv preprint arXiv:1902.07694*, 2019.

[17] MS Safronova, D Budker, D DeMille, Derek F Jackson Kimball, A Derevianko, and Charles W Clark. Search for new physics with atoms and molecules. *arXiv preprint arXiv:1710.01833*, 2017.

[18] Lorenza Viola and Seth Lloyd. Dynamical suppression of decoherence in two-state quantum systems. *Physical Review A*, 58(4):2733, 1998.

[19] Anders Sørensen and Klaus Mølmer. Quantum computation with ions in thermal motion. *Physical review letters*, 82(9):1971, 1999.

[20] Anders Sørensen and Klaus Mølmer. Entanglement and quantum computation with ions in thermal motion. *Physical Review A*, 62(2):022311, 2000.

[21] Erwin L Hahn. Spin echoes. *Physical review*, 80(4):580, 1950.

[22] Marcin Zwierz, Carlos A Pérez-Delgado, and Pieter Kok. Ultimate limits to quantum metrology and the meaning of the heisenberg limit. *Physical Review A*, 85(4):042112, 2012.

[23] D Leibfried, Murray D Barrett, T Schaetz, J Britton, J Chiaverini, Wayne M Itano, John D Jost, Christopher Langer, and David J Wineland. Toward heisenberg-limited spectroscopy with multiparticle entangled states. *Science*, 304(5676):1476–1478, 2004.

[24] JD Prestage, Go J Dick, and L Maleki. New ion trap for frequency standard applications. *Journal of Applied Physics*, 66(3):1013–1017, 1989.

[25] Nitzan Akerman, Y Glickman, Shlomi Kotler, Anna Keselman, and Roee Ozeri. Quantum control of 88sr+ in a miniature linear paul trap. *Applied Physics B*, 107(4):1167–1174, 2012.

[26] Nitzan Akerman. *Trapped ions and free photons*. PhD thesis, 2012.

[27] T Manovitz. Individual addressing and imaging of ion in a paul trap. Master's thesis, Feinberg Graduate School, The Weizmann Institute, 2016.

[28] Wayne M Itano, James C Bergquist, John J Bollinger, JM Gilligan, DJ Heinzen, FL Moore, MG Raizen, and David J Wineland. Quantum projection noise: Population fluctuations in two-level systems. *Physical Review A*, 47(5):3554, 1993.

[29] Jean-Pierre Likforman, Samuel Guibal, Luca Guidoni, et al. Precision measurement of the branching fractions of the 5p 2 p 1/2 state in 88 sr+ with a single ion in a micro fabricated surface trap. *arXiv preprint arXiv:1511.07686*, 2015.

[30] F Diedrich, JC Bergquist, Wayne M Itano, and DJ Wineland. Laser cooling to the zero-point energy of motion. *Physical Review Letters*, 62(4):403, 1989.

[31] Jürgen Eschner, Giovanna Morigi, Ferdinand Schmidt-Kaler, and Rainer Blatt. Laser cooling of trapped ions. *JOSA B*, 20(5):1003–1015, 2003.

[32] Claude Cohen-Tannoudji, Jacques Dupont-Roc, and Gilbert Grynberg. *Atom-photon interactions: basic processes and applications*. 1998.

[33] Shlomi Kotler, Nitzan Akerman, Yinnon Glickman, Anna Keselman, and Roee Ozeri. Single-ion quantum lock-in amplifier. In *Quantum Information and Measurement*, pages QM2A–3. Optical Society of America, 2012.

[34] Michael Bishof, Xibo Zhang, Michael J Martin, and Jun Ye. Optical spectrum analyzer with quantum-limited noise floor. *Physical review letters*, 111(9):093604, 2013.

[35] Shahaf Aharony, Nitzan Akerman, Roee Ozeri, Gilad Perez, Inbar Savoray, and Ravid Shaniv. Constraining rapidly oscillating scalar dark matter using dynamic decoupling. *arXiv preprint arXiv:1902.02788*, 2019.

[36] Ravid Shaniv, Tom Manovitz, Yotam Shapira, Nitzan Akerman, and Roee Ozeri. Toward heisenberg-limited rabi spectroscopy. *Physical Review Letters*, 120(24):243603, 2018.

[37] Wayne M Itano. External-field shifts of the 199hg+ optical frequency standard. *Journal of research of the National Institute of Standards and Technology*, 105(6):829, 2000.

[38] GP Barwood, HS Margolis, G Huang, P Gill, and HA Klein. Measurement of the electric quadrupole moment of the 4 d d 5/2 2 level in s r+ 88. *Physical review letters*, 93(13):133001, 2004.

[39] Wayne M Itano. Quadrupole moments and hyperfine constants of metastable states of ca+, sr+, ba+, yb+, hg+, and au. *Physical Review A*, 73(2):022510, 2006.

[40] Chiranjib Sur, KVP Latha, Bijaya K Sahoo, Rajat K Chaudhuri, BP Das, and Debashis Mukherjee. Electric quadrupole moments of the d states of alkaline-earth-metal ions. *Physical review letters*, 96(19):193001, 2006.

[41] Dansha Jiang, Bindiya Arora, and MS Safronova. Electric quadrupole moments of metastable states of ca+, sr+, and ba+. *Physical Review A*, 78(2):022514, 2008.

[42] R Shaniv, R Ozeri, MS Safronova, SG Porsev, VA Dzuba, VV Flambaum, and H Häffner. New methods for testing lorentz invariance with atomic systems. *Physical review letters*, 120(10):103202, 2018.

[43] Don Colladay and V Alan Kostelecký. Lorentz-violating extension of the standard model. *Physical Review D*, 58(11):116002, 1998.

[44] T. Pruttivarasin, M. Ramm, S. G. Porsev, I.I. Tupitsyn, M. S. Safronova, M. A. Hohensee, and H. Häffner. Michelson-morley analogue for electrons using trapped ions to test lorentz symmetry. *Nature*, 517:592, 2015.

[45] M. A. Hohensee, N. Leefer, D. Budker, C. Harabati, V. A. Dzuba, and V. V. Flambaum. Limits on violations of lorentz symmetry and the einstein equivalence principle using radio-frequency spectroscopy of atomic dysprosium. *Phys. Rev. Lett.*, 111(5):050401, 2013.

[46] V Alan Kostelecký and Charles D Lane. Constraints on lorentz violation from clock-comparison experiments. *Physical Review D*, 60(11):116010, 1999.

[47] Saul Meiboom and David Gill. Modified spin-echo method for measuring nuclear relaxation times. *Review of scientific instruments*, 29(8):688–691, 1958.

[48] VA Dzuba, VV Flambaum, MS Safronova, SG Porsev, T Pruttivarasin, MA Hohensee, and H Häffner. Strongly enhanced effects of lorentz symmetry violation in entangled yb+ ions. *Nature Physics*, 12(5):465, 2016.

[49] Christian Sanner, Nils Huntemann, Richard Lange, Christian Tamm, Ekkehard Peik, Marianna S Safronova, and Sergey G Porsev. Optical clock comparison test of lorentz symmetry. *arXiv preprint arXiv:1809.10742*, 2018.

[50] P Oetal Schmidt, T Rosenband, C Langer, Wayne M Itano, James C Bergquist, and David J Wineland. Spectroscopy using quantum logic. *Science*, 309(5735):749–752, 2005.

[51] Florian Mintert and Christof Wunderlich. Ion-trap quantum logic using long-wavelength radiation. *Physical Review Letters*, 87(25):257904, 2001.

[52] C Ospelkaus, U Warring, Y Colombe, KR Brown, JM Amini, D Leibfried, and DJ Wineland. Microwave quantum logic gates for trapped ions. *Nature*, 476(7359):181, 2011.

[53] TL Nicholson, MJ Martin, JR Williams, BJ Bloom, M Bishof, MD Swallows, SL Campbell, and J Ye. Comparison of two independent sr optical clocks with 1× 10- 17 stability at 10 3 s. *Physical review letters*, 109(23):230801, 2012.

[54] Nathan D Lemke, Andrew D Ludlow, ZW Barber, Tara M Fortier, Scott A Diddams, Yanyi Jiang, Steven R Jefferts, Thomas P Heavner, Thomas E Parker, and Christopher W Oates. Spin-1/2 optical lattice clock. *Physical Review Letters*, 103(6):063001, 2009.

[55] Stephan Falke, Nathan Lemke, Christian Grebing, Burghard Lipphardt, Stefan Weyers, Vladislav Gerginov, Nils Huntemann, Christian Hagemann, Ali Al-Masoudi, Sebastian Häfner, et al. A strontium lattice clock with 3×

10- 17 inaccuracy and its frequency. *New Journal of Physics*, 16(7):073023, 2014.

[56] Daniel FV James. Quantum dynamics of cold trapped ions with application to quantum computation. *Applied Physics B: Lasers and Optics*, 66(2):181–190, 1998.

[57] Ravid Shaniv, Nitzan Akerman, Tom Manovitz, Yotam Shapira, and Roee Ozeri. Quadrupole shift cancellation using dynamic decoupling. *arXiv preprint arXiv:1808.10727*, 2018.

[58] M Chwalla, K Kim, T Monz, P Schindler, M Riebe, CF Roos, and R Blatt. Precision spectroscopy with two correlated atoms. *Applied Physics B*, 89(4):483–488, 2007.

[59] Chin-Wen Chou, DB Hume, Michael J Thorpe, David J Wineland, and T Rosenband. Quantum coherence between two atoms beyond q= 10 15. *Physical review letters*, 106(16):160801, 2011.